UNIVERSITÀ DI PISA

Dipartimento di Fisica *E. Fermi*

Corso di Laurea Magistrale in Fisica

Characterization of irradiated monolithic CMOS active pixel sensors for the upgrade of the Belle II Vertex Detector

Relatori:

Prof. Francesco Forti

Prof.ssa Giuliana Rizzo

Candidato:

Guglielmo Francesco Benfratello

Anno Accademico 2024/2025

Introduction

Belle II is a particle physics experiment located at the KEK laboratory in Tsukuba (Japan). The detector is a general-purpose spectrometer which studies electron-positron collisions produced by the SuperKEKB accelerator, a second generation flavor-factory which operates at the luminosity frontier, holding the world record instantaneous luminosity of $L_{peak} = 5.1 \times 10^{34}\ \mathrm{cm}^{-2}\,\mathrm{s}^{-1}$.

SuperKEKB is the upgrade of the previous facility KEKB (operational from 1998 to 2010) and consists in a 3 km-circumference asymmetric accelerator which collides electrons and positrons beams at a center-of mass energy near the $\Upsilon(4S)$ resonance ($\sqrt{s} = 10.58$ GeV). Data taking started in March 2019.

In the next decade, the goal of Belle II and SuperKEKB is to reach a peak luminosity of $6 \times 10^{35}\ \mathrm{cm}^{-2}\,\mathrm{s}^{-1}$ and to collect 50 ab^{-1} (approximately 50 times the existing dataset) of data. This will allow to study CP violation in B and D mesons system with unprecedented accuracy and to search for physics beyond the Standard Model through precision measurements.

In order to reach these ambitious goals a detector upgrade is needed, to cope with increased radiation damage and background, which could otherwise hinder the operation of the Belle II detector at this increased luminosity, and to accommodate possible modifications to the interaction region geometry that might be required to reach high luminosity.

The main subdetector which needs to be upgraded is the vertex detector (VXD), the nearest to the point of interaction, composed by the inner pixel detector (PXD) and the outer silicon strip vertex detector (SVD). The proposal chosen for the upgrade of this detector is the VerTeX Detector (VTX), which is a new vertex detector with six layers of pixelated sensors based on the CMOS Depleted Monolithic Active Pixel Sensor (DMAPS) technology to replace the VXD.

The beam conditions needed for running at high luminosity generate a large rate of background particles in Belle II. The expected hit rate is 120 $\mathrm{MHz\,cm}^{-2}$ in the innermost layer at maximum, translating into radiation levels of 10 Mrad/year ionising dose and fluences reaching 5×10^{13} 1-MeV-$\mathrm{n_{eq}}/\mathrm{cm}^2$/year.

This new detector is being designed to have higher granularity in both space and time, which gives greater robustness against beam-induced backgrounds and also improves tracking efficiency and resolution, especially at low momentum. This leads to better impact parameter and vertex resolution, allowing improved time-dependent analyses of B and D mesons' decays and a more powerful rejection of background events.

In addition, the material budget must be kept as small as possible, below the $3.5\%\,X_0$ of the current VXD. The requirements on granularity and material budget can be met with DMAPS technology and prompted the development of a new silicon sensor, OBELIX, fabricated using a modified version of the 180 nm CMOS TowerJazz Semiconductor process, whose design is being completed. OBELIX will have a depleted sensitive thickness of 30 µm, with the possibility of a sensor with a physical thickness of 40 or 50 µm. The pixel size is $33.04 \times 33.04\ \mu\mathrm{m}^2$ to ensure sufficient granularity.

This thesis presents the characterization of the precursor of OBELIX, the TJ-Monopix2 sensor, originally developed for the ATLAS ITk.

Results from previous test campaigns had already confirmed that the performance specifications could be achieved with non-irradiated TJ-Monopix2 sensors. In this campaign the performance of the sensor after irradiation was studied in detail, since previous test beam campaigns on irradiated samples had shown promising results but also an efficiency degradation at higher threshold and temperature. Laboratory and beam tests to study the efficiency as a function of threshold and temperature have been conducted on four devices irradiated with fluences from 1×10^{14} 1-MeV-$\mathrm{n_{eq}}/\mathrm{cm}^2$ to 5×10^{14} 1-MeV-$\mathrm{n_{eq}}/\mathrm{cm}^2$, which describe the full range of the radiation damage expected during the 10-year operation of VTX.

The study in laboratory of the behaviour of the chip focused on finding configurations that allowed a stable operation at different temperatures, which have then been used during a Test Beam at DESY in April 2025 and also to optimize the design of the OBELIX chip. The tests conducted in the laboratory and test beam campaign

have been done in a chip temperature range that goes from $\sim$ 10 to $\sim$ 50 °C, which is more than the expected temperature range at operation in the new VTX detector, but gives a meaningful insight into the behaviour of the chip.

In more detail, these tests focused on studying the threshold distributions for the two tested types of front-end circuits implemented in the matrix, mainly using internal injection methods. Dedicated procedures were developed and applied to minimize the threshold dispersion and noise for each of them. The chip registers were optimized to operate the sensor at the lowest possible threshold, to achieve high efficiency also after irradiation.

Another part of this study was conducted on the clock counter (BCID) cross-talk effect, which changes the threshold of the pixel depending on the time of the hit with respect to the counter reset. In our measurements we found that this effect is temperature dependent and is the main limiting factor to the sensor's performance, due to its significant contribution to noise. The magnitude of this effect has shown to be linearly dependent on the number of columns on which the clock signal is enabled, meaning that, if not mitigated or cured, in OBELIX it could be 1.6 times larger, hindering the operation of the sensor at high efficiency.

The beam test with 4.2 GeV electrons focused on measuring the efficiency at different irradiation fluences, temperatures and configurations, providing crucial indications for the design of the OBELIX chip, its future operation, and for the temperature specifications of the VTX ladders cooling system.

The threshold dependence on the temperature of the chip, which becomes worse due to the radiation damage to the bulk, has been meticulously studied.

The results of these measurements show that the DCC front-end performs significantly better than the other tested one after irradiation and for this reason it was chosen as the only front-end of the upcoming OBELIX chip.

Discrepancies in the efficiency of the sensors irradiated with electrons and protons at the same equivalent fluence hinted at a smaller-than-expected effective bulk damage of the electron irradiation, which was also confirmed by measurements of the leakage current of the sensors.

In conclusion, in our measurements two major features of irradiated TJ-Monopix2 sensors were investigated: the clock counter cross-talk and the efficiency dependence on threshold and temperature.

The clock signal cross-talk study prompted the implementation of a cure in the upcoming OBELIX submission, while the efficiency studies in the Test Beam at DESY have given a better insight on the possible limitations for the operation of the new vertex detector of Belle II. Furthermore, these measurements have been crucial in the decision of the front-end of the OBELIX chip.

This work has concluded the characterization of TJ-Monopix2, paving the way for the submission of OBELIX. The future work will be the testing and characterization of OBELIX to complete the design of VTX and to prepare for the detector operation.

The measurements leading to these results have been performed at the Test Beam Facility at DESY Hamburg (Germany), a member of the Helmholtz Association (HGF). The laboratory characterization was carried out in the INFN-Pisa "Laboratori Alte Tecnologie".

Chapter 1 briefly describes the open questions of the Standard Model that can be answered by B-Factories and then presents the SuperKEKB accelerator, with a focus on the background sources, and the Belle II detector, with a focus on the current vertex detector.

Chapter 2 outlines the motivations behind the upgrade and presents the overall upgrade program of the experiment, focusing on the VTX project and detailing its requirements and its expected physics' performance, concluding with the specifications for the new pixel sensor.

Chapter 3 gives an overview of the use of semiconductor detectors for the detection of radiation, describing their working principles and the different types of sensors that use this technology, like strip, hybrid pixel and monolithic pixel sensors. It then focuses on the effects of temperature and radiation damage on their performance.

Chapter 4 is centered around the Monolithic Active Pixel Sensors, with a description of their working principle and the main modifications to the TowerJazz 180 nm CMOS process that have been crucial for the development of TJ-Monopix2 and OBELIX. These two sensors are then described with their main features, the registers used for operation and the column-drain readout architecture.

Chapter 5 presents the complete set of results from the laboratory measurement, both for the preparation for the Test Beam and for the characterization of the BCID cross-talk effect. The chapter begins by detailing the tests done on these sensors, the effects of irradiation and the laboratory setup used, to then describe the results of the laboratory measurements.

Chapter 6 presents the main results obtained from the test beam measurements at DESY, with a focus on the evolution of the detection efficiency under different operating conditions. The chapter begins with a description of the test beam setup, followed by an explanation of the data analysis procedure. The results are then presented, with particular emphasis on the efficiency variations at different temperatures and thresholds.

Index

Chapter 1

Belle II and SuperKEKB

This chapter describes the Belle II experiment and its scientific motivation. Starting from some of the open questions in the Standard Model, it then describes the peculiarities of the B-Factories, focusing on SuperKEKB and Belle II, with a description of their apparatus.

1.1 Physics program

The Standard Model (SM) is a very successful theory that describes three of the four fundamental forces with which elementary particles interact: the electromagnetic, strong and weak interactions, with the exception of the gravitational force. In this model, all the elementary constituents of ordinary matter (fermions, with half-integer spin, and bosons, with integer spin) are classified in four groups, as shown in Figure 1.1: the quarks and leptons (the fermions), which are the matter fields; the vector bosons, which mediate the interactions, and the Higgs boson, the only scalar boson, which is needed to give a mass to the matter fields.

Figure 1.1: The particle classification in the Standard Model.

While the SM has achieved numerous successes in describing almost all the known particle phenomenology, many questions remain still unanswered. The main questions can be summarized as follows [1]:

- The SM does not explain whether the three generations of fermions that have been discovered are the only ones.
- The reasons behind the mass hierarchy in fermions, i.e. the large differences in the masses of quarks and leptons, are unknown.
- The mechanism with which neutrinos acquire their (very small) masses is unknown.

- The matter-antimatter asymmetry in the universe is not explained: Charge-Parity (CP) violation is necessary to explain the asymmetry, but the SM mechanism only accounts for a value several orders of magnitude smaller than what is needed to explain the matter domination over antimatter, which allowed the evolution of the universe as we know it today.
- The flavour-changing currents are phenomenologically described with two mixing matrices: the Cabibbo-Kobayashi-Maskawa (CKM) matrix for the quarks and the Pontecorvo-Maki-Nakagawa-Sakata (PMNS) matrix for the neutrinos. The SM fails to provide any explanation for the values of their elements (nearly diagonal for the quarks, highly non diagonal for the neutrinos), which, in the case of the CKM matrix, could be hiding a new symmetry.
- Astrophysical observations indicate the existence of dark matter, but its origin and nature have not been explained yet.

The search for the answers to these questions is being carried on in several experiments of particle physics, working with two complementary approaches: at the energy frontier and at the intensity frontier. Experiments at the energy frontier search for New Physics (NP) at the highest possible energy, employing huge colliders such as the Large Hadron Collider (LHC) at CERN, that operates at a center-of-mass energy of $\sqrt{s} = 14$ GeV. Experiments at the intensity frontier, instead, search for NP through precision measurements of suppressed processes or deviations from the SM predictions. One of the main experiments that follows this approach is Belle II at the SuperKEKB B-Factory at KEK.

Thanks to very high statistics, Belle II has a very broad physics program in many areas of precision flavour physics. Specifically, it studies CP violation in the B and D mesons systems, carries out searches of NP signals in rare decays of B and D mesons, and τ leptons, explores many different possible signatures of dark matter particles.

1.2 Asymmetric B-Factories and SuperKEKB

Asymmetric B-Factories are particle accelerators designed to produce a large number of B mesons using beams of different energies. To this day, only three of them have been realized (PEP-II for the Babar experiment, KEKB for the Belle experiment and SuperKEKB for the Belle II experiment) of which only SuperKEKB is still in operation. To reach this goal, electrons and positrons are collided at the $\Upsilon(4S)$ resonance, at a center-of-mass energy of $\sqrt{s} = 10.58$ GeV, which decays $> 96\%$ of times into a $B\bar{B}$ pair.

The small mean life ($\tau_B \simeq 1.5 \times 10^{-12}$ s) of the B mesons results in $c\tau \simeq 450$ µm. The resonance is slightly above ($m_{\Upsilon(4S)} - 2m_B \simeq 20$ MeV) the threshold for the production of a pair of B mesons; therefore, in the symmetric beams configuration of the accelerator, the decay length of these mesons $\ell_B = \beta\gamma c\tau$ would be too small to be detected.

The study of CP violations (in particular the time-dependent processes), however, requires a precise measurement of the decay time difference of the two B mesons, whose uncertainty is dominated by the decay vertex resolution (≈ 20 µm). For this reason a different approach is needed, in which the beam energies are asymmetric, with a center-of-mass boost in the laboratory frame that allows the reconstruction of the B mesons decay vertices, their lifetimes, and the time-dependent decay rate asymmetries. In particular, SuperKEKB collides an electrons beam of 7 GeV (High Energy Ring, HER) with a positrons beam of 4 GeV (Low Energy Ring, LER) with a Lorentz boost factor of the $\Upsilon(4S)$ of $(\beta\gamma)_{\Upsilon(4S)} \approx 0.28$. This results in a decay length of these mesons of:

$$\ell \simeq (\beta\gamma)_{\Upsilon(4S)} c\tau \approx 126\,\mu\text{m} \tag{1.1}$$

This number, which is measurable but still very small, indicates that an extremely good vertexing resolution is crucial for the reconstruction of secondary vertices (the decay points of B, D, τ) and more in general for the precise event reconstruction.

An illustration of an example of an event at Belle II is depicted in Figure 1.2: the two B mesons are produced in an entangled state and, therefore, when one assigns the flavor of one of them from its decay products (e.g. B^0, which is defined as the *tag* meson B^0_{tag}), then it is also possible to assign the flavor of the other, which is the opposite ($\bar{B}^0$, defined as $\bar{B}^0_{phys}$).

From the reconstruction of the decay vertices, their positions in the longitudinal direction z_1 and z_2 are evaluated, from which their difference Δz and their proper time decay difference Δt can be computed:

$$\Delta z = z_1 - z_2 = (\beta\gamma)_{\Upsilon(4S)} c\Delta t \tag{1.2}$$

A small time uncertainty is therefore strictly dependent on a good vertexing resolution and reconstruction capability. This time-resolved measurement is only possible in the asymmetric configuration.

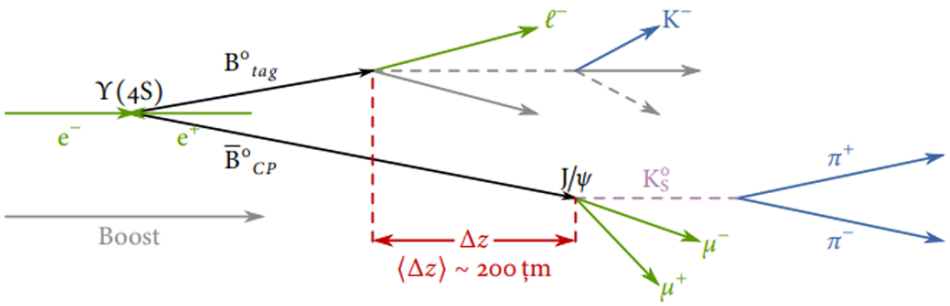

Figure 1.2: A schematic depiction of an event in Belle II.

1.2.1 The SuperKEKB Accelerator

SuperKEKB (shown in Figure 1.3) is an asymmetric electron-positron collider, with a 3 km circumference, that operates at the $\Upsilon(4S)$ resonance at the center-of-mass energy of 10.58 GeV. It is an upgraded and improved version of the KEKB accelerator, which was operated from 1998 to 2010, reached a peak instantaneous luminosity of 2.11×10^{34} cm^{-2} s^{-1} and collected almost 1 ab^{-1}, aiming at reaching the target instantaneous luminosity of 6×10^{35} cm^{-2} s^{-1}, with an integrated luminosity of 10 ab^{-1}.

To reach the target luminosity, an improvement of the accelerating and colliding scheme has been employed, called the nano-beam scheme.

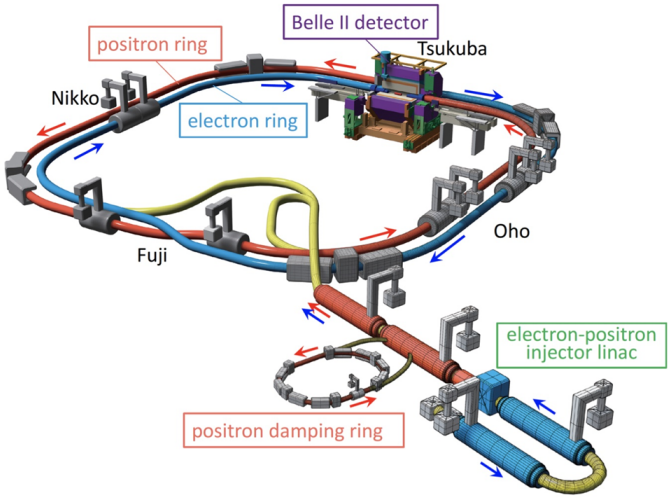

Figure 1.3: The SuperKEKB accelerator.

Luminosity. Instantaneous luminosity is one of the key parameters of any collider, in particular if it hosts experiments at the intensity frontier. It is defined as the number N of interactions per second per unit of cross section, from which it is also possible to extract the number of events with a given cross section σ that have been produced in a given time T:

$$L = \frac{1}{\sigma}\frac{dN}{dt} \Rightarrow N = \int_0^T L\sigma dt \tag{1.3}$$

At a collider, luminosity can also be expressed as:

$$L = \frac{N_b n_+ n_- f}{A_{\text{eff}}} \text{ with } A_{\text{eff}} = \frac{\sigma_x^* \sigma_y^*}{R_L} \tag{1.4}$$

where N_b is the number of bunches circulating in each ring, n_+ and n_- are the number of positrons and electrons per bunch, f is the revolution frequency, and A_{eff} is the effective transverse overlap area of the bunches at the

Interaction Point; A_{eff} is given by the product of σ_x^* and σ_y^* (the transverse bunches sizes at the IP), and is reduced by an effective factor R_L, which limits the luminosity increase at high beam currents.

To increase luminosity two approaches can be followed: increasing the beam currents and decreasing the overlap area. Both are pursued at SuperKEKB.

The increase in the currents can be pursued with both an increase in the number of particles per bunch ($n_\pm$) or the number of bunches (N_b), which poses significant challenges that need to be tackled by dedicated upgrades of the accelerator. One of these is the maximum allowed distance between bunches, which is limited by the accelerator but can be improved with dedicated designs.

In particular, KEKB and SuperKEKB chose the approach with a small crossing angle between the beams, which allows for smaller bunch spacing, while avoiding parasitic crossing. The crossing angle at KEKB was 22 mrad and SuperKEKB has further increased it to 83 mrad, also improving luminosity by employing the Nano-Beam scheme, initially proposed for the SuperB project [2].

This scheme, which significantly reduces the effective crossing area, is shown in Figure 1.4 and it requires to employ a large crossing angle, a great bunch length σ_z and a very small horizontal bunch size σ_x. In this way, A_{eff}, which depends on the horizontal overlap d, can be reduced, increasing the luminosity, solving the "hourglass" effect (i.e. the enlargement of the tails of the bunches due to the oscillation of the vertical betatron function β_y) and reducing the parasitic collisions (i.e. the collisions along the enlarged tails).

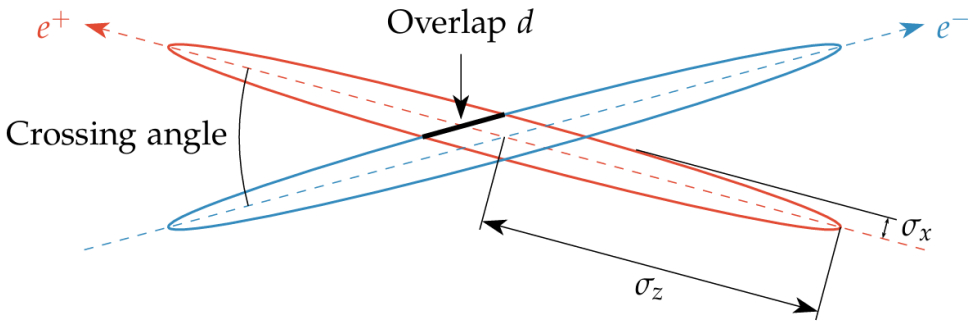

Figure 1.4: The Nano-Beam scheme employed at SuperKEKB.

A comparison between the parameters of KEKB and SuperKEKB is shown in Table 1.1, showing the great improvements of the new accelerator.

	KEKB	SuperKEKB
Energy (LER/HER) [GeV]	3.5/8.0	4.0/7.0
N_b	1585	2249
β_y [mm]	5.9/5.9	0.6/0.6
I [A]	1.64/1.19	1.39/1.12
Luminosity [10×10^{34} cm^{-2} s^{-1}]	2.11	5.1
Time between collisions [ns]	5.9	4.2
Crossing angle [mrad]	$\pm$11	$\pm$41.5
σ_z [mm]	6.5/6.5	8.3/7.6
σ_x [µm]	117/124	17.9/16.6

Table 1.1: Fundamental parameters of KEKB and SuperKEKB (from [3, 4]) at the present date (September 2025).

1.2.2 Background sources

One of the most important characteristics of the high-luminosity e^+e^- colliders is the production of unwanted background in the detector, originating both by the individual beams and in the collision. The characterization (and reduction) of this background is crucial both for the detector design and the optimization of the running conditions.

The backgrounds produced within each beam are called "single-beam" backgrounds. Some examples are the synchrotron radiation, the intrabeam Touschek scattering or the "beam-gas" scattering. In particular, Touschek

scattering is the straying of beam particles due to the Coulomb scattering with other particles in the same bunch, while the "beam-gas" scattering is the scattering of beam particles with residual gas in the vacuum.

A significant number of particles from these background sources can reach the beam pipe near the IP and produce signals in the Belle II detector. While they are difficult to simulate accurately, some precautions have been taken to reduce their intensity, for example by placing movable collimators to scrape the beam halo, or to mitigate their effects, for instance by filtering the charged tracks in an event by imposing a maximum distance from the IP.

In general, single beam backgrounds depend on the beam characteristics, such as the curent on the number of bunches, but not directly on luminosity.

Backgrounds produced by the collision of the bunches have a linear dependence on luminosity, and are therefore called "luminosity-dependent" backgrounds. Some examples are the radiative Bhabha scattering ($e^+e^- \to e^+e^-\gamma$) and the two-photon process $e^+e^- \to e^+e^-e^+e^-$. The former can create large energy deposits in the machine elements near the IP, with showers that extend to the detector region. It is mitigated with properly placed heavy metal shields near the IP. The latter creates a large number of low energy curling e^+e^- pair, which are prevented from reaching the detector by the strong solenoidal field.

Another important background comes from the top-up injection. In this procedure a bunch enters the main ring at an angle and is deflected on the orbit direction by a dedicated magnet. Before reaching the injection point, the pre-existing bunch is moved closer to the new bunch by a pair of kickers (magnets activated for a short time with a strong field). The new bunch is then injected in phase with the pre-existing bunch and both are puth on the nominal orbit by another pair of kickers. This new bunch, however, will be slightly out of this orbit due to the (small) distance between the two bunches during the injection, which causes it to oscillate for a few ms until the synchrotron radiation losses dampens it.

The large amount of synchrotron radiation produced by these oscillating particles, together with the particles which remain strayed out of the nominal orbit, behaves as a single-beam background, but with a more severe effect that requires particular attention during the operation [5].

1.2.3 Current status of data taking

Belle II has started its physics operations in 2019 and plans to continue until 2042, with the goal to collect 50 ab^{-1} of data [6]. During its operation, three phases (Runs) are scheduled, with periods of pause between them (Long Shutdowns, LS) to upgrade the detector and the accelerator.

During Run 1, which lasted from 2019 to 2022, 365 fb^{-1} have been collected at the $\Upsilon(4S)$ resonance and 63 fb^{-1} at higher and lower energies. In 2024, after Long Shutdown 1, during which the installation of the vertex detector was completed, Run 2 has started , with the goal of collecting up to 10 ab^{-1} until 2032, when a significant upgrade (more details in Chapter 2) is scheduled. During the last run, the collider has reached the world record instantaneous luminosity of $5.1 \times 10^{34}\ \text{cm}^{-2}\,\text{s}^{-1}$. Until September 2025 the detector has collected a total 575 fb^{-1}.

Finally, Run 3 will start in 2034 after the upgrade of both the detector and the accelerator and will last until 2042, with the goal of reaching the total data set of 50 ab^{-1}.

To reach this ambitious goals, the instantaneous luminosity should constantly increase up to $6 \times 10^{35}\ \text{cm}^{-2}\,\text{s}^{-1}$, following the plan shown in Figure 1.5.

1.3 Belle II detector

The Belle II detector [7] is a general-purpose spectrometer arranged in a concentric sequence of sub-detectors placed around the berillium beam pipe, at the IP of the two beams. The boosted center of mass frame results in an asymmetric acceptance of the detector. The physics requirements of the B-Factories prompt the need for the use of specific detectors:

- *Tracking* sub-detectors, which reconstruct the tracks of charged particles, divided into a *vertex detector*, which reconstructs the decay vertices of the particles produced at the IP, and a *drift chamber*.
- *Particle IDentification* (PID) sub-detectors, based on the Cherenkov effect.
- An *electromagnetic calorimeter*, which mainly reconstructs the photons and the electrons.
- A superconducting *solenoid*, with a 1.5 T magnetic field for the measurement of the track momenta.
- *Muon identification and K_L^0 detection subdetectors*, which also serve as the return yoke of the solenoid magnet.

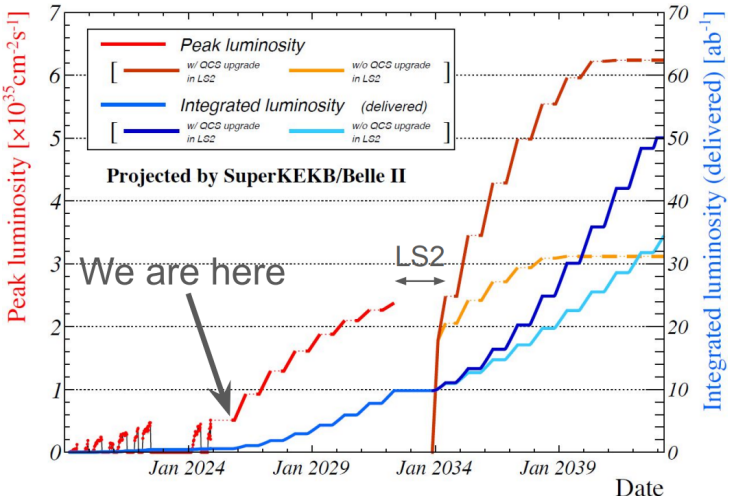

Figure 1.5: The luminosity projection for the operation of Belle II.

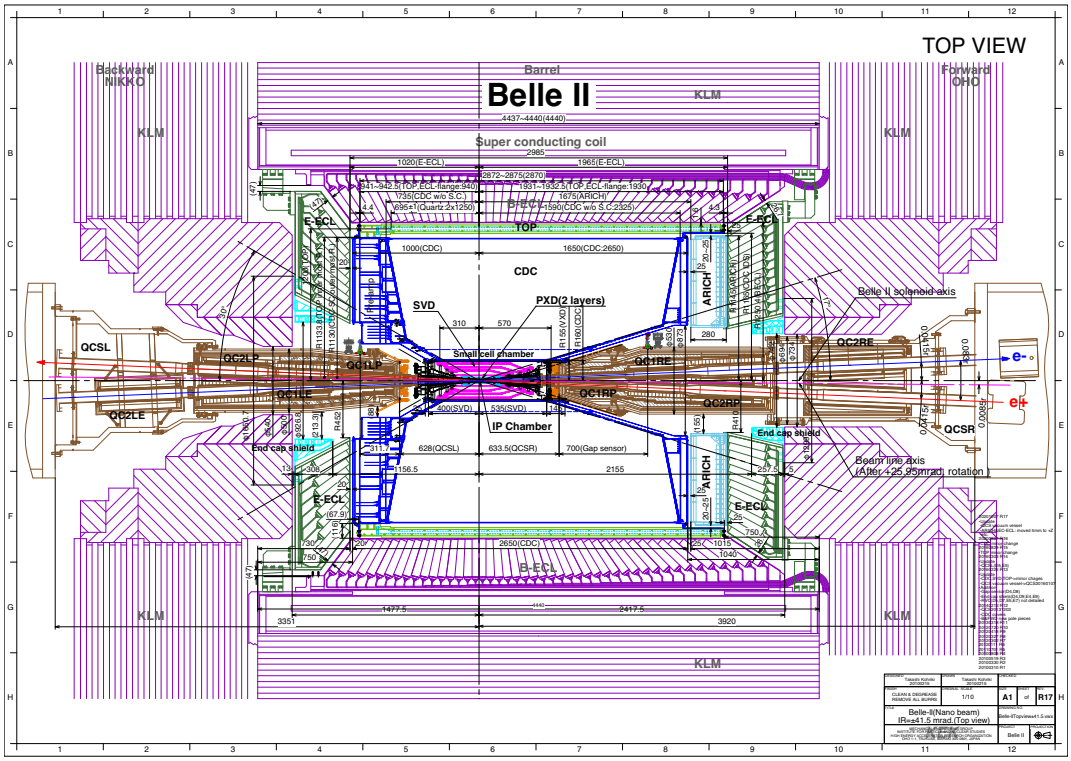

Figure 1.6: The top view of the Belle II detector.

A top view of the Belle II detector is shown in Figure 1.6.

In the following the subdetectors are briefly described.

VXD. The VerteX Detector (VXD) is composed of two siliicon-based sub-detectors, the pixel detector (PXD) and the silicon vertex detector (SVD), placed as close as possible to the IP to achieve the necessary vertexing resolution ($\sim$ 20 µm). This six-layer sensor (2 for the PXD and 4 for the SVD) has to comply with strict material budget requirements, to avoid worsening the tracking performance.

As shown in Figure 1.7, the detector has an asymmetric structure along the longitudinal axis, due to the asymmetric beam energies. In the forward direction the sensors are slanted to reduce the particle crossing angle, thus minimizing the multiple scattering effects while maintaining a good signal-to-noise ratio.

More details on the sub-detectors are provided in Section 1.4.

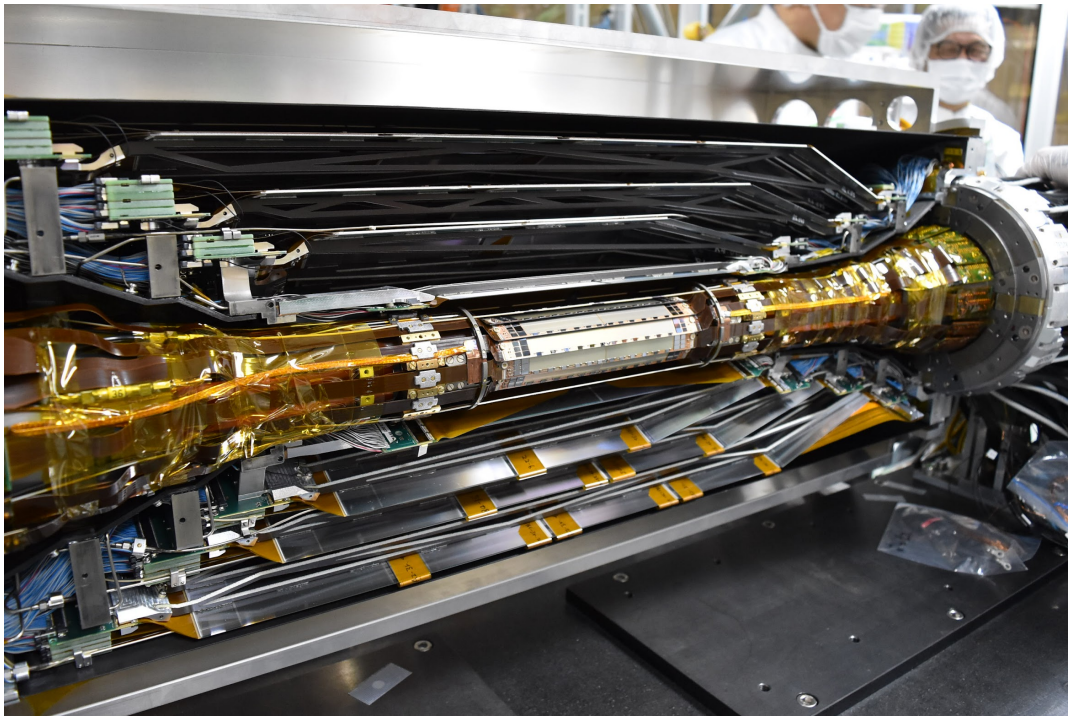

Figure 1.7: The VXD detector during LS1, with the entire PXD and half SVD installed.

CDC. The Central Drift Chamber (CDC) is the central tracking device, which covers the radial range from 17 cm to 113 cm and has a polar angle acceptance that ranges from 17° to 150°. The CDC uses a gas mixture of 50 % helium and 50 % ethane, with 14 thousand tungsten-gold wires arranged either in axial (aligned with the solenoidal magnetic field) or stereo (skewed with respect to the axial wires, for longitudinal position) orientation. The wires are distributed in 56 layers, grouped into nine "superlayers", as shown in Figure 1.8, that alternate between the axial and the stereo configuration.

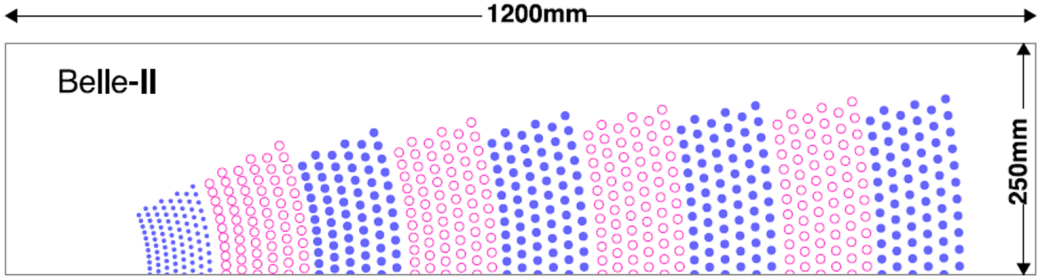

Figure 1.8: The superlayers of the CDC detector.

Combining the information from both the axial and the stereo layers it is possible to reconstruct full three-dimensional helix charged tracks and measure their momenta. It also provides information for PID by measuring the ionization energy loss, which is particularly useful for low-momentum particles.

TOP. The Time of Propagation (TOP) counter is one of the two detectors based on the Cherenkov effect that provide poweful PID capabilities to the experiment. It consists of 16 quartz bars of cross section 45×2 cm^2 and a length of 2.6 m, with the sensor at the end of the bar, in the barrel region outside the CDC. In order to achieve a single-photon time resolution of about 100 ps (required for a good PID), 16-channel microchannel plate photomultiplier tubes (MCP-PMT) are employed, specifically developed for this purpose, which can operate even in high magnetic field. A schematic representation is shown in Figure 1.9.

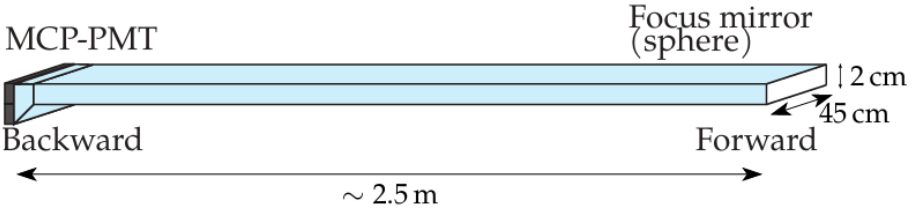

Figure 1.9: Schematic representation of the TOP detector.

ARICH. The Aerogel Ring Imaging CHerenkov (ARICH) is the second detector based on the Cherenkov effect. It is placed in the forward endcap region and it completes the PID detectors. It is made of a proximity-focusing aerogel Cherenkov radiator, followed by an empty expansion volume and an array of photon detectors.

To increase the number of detected Cherenkov photons two 2 cm-thick layers of aerogel with slightly different refractive indices ($n_1 = 1.045$, $n_2 = 1.055$) are used, which increase the photon yield without degrading the Cherenkov angle resolution. The schematic of the detector is shown in Figure 1.10.

The photodetectors are pixelated hybrid avalanche photo-diodes (HAPD) with a pitch of 4.9 mm.

The main task of the TOP and ARICH detectors is to provide the K/π separation from about ≈ 1 GeV c^{-1} until 3.5 and 4 GeV c^{-1} of momentum, respectively.

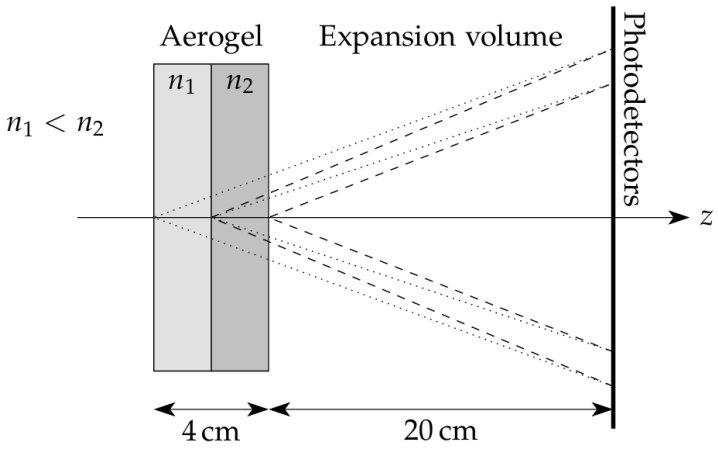

Figure 1.10: Schematic principle of the ARICH detector.

ECL. The Electromagnetic Calorimeter (ECL) is a highly segmented array of thallium-doped caesium iodide (Cs I (Tl)) crystals, with an average cross section of 6×6 cm^2 and a length of 30 cm, corresponding to $\sim 16\ X_0$. The crystals are assembled in a 3 m long barrel section with a radius of 1.25 m, and two endcap discs located at 2 m (forward) and 1 m (backward).

In addition to photons, this detector is used to detect electrons, improving the e/π separation, and to provide a first active interaction medium for neutral hadrons (n, K^0_L).

KLM. Outside the solenoid there is the return yoke of the magnetic flux, made of 4.7 cm-thick iron plates. To make the K^0_L and μ detector (KLM), these plates are alternated with active detector elements. The iron provides a total of 3.9 hadronic interaction lengths in which neutrons and K^0_L mesons can shower, to be added to the 0.8 interaction lengths of the ECL.

The active detector elements are resistive plate chambers (RPCs) for the outer barrel section and plastic scintillator readout by silicon photomultipliers (SiPMs) through wavelenght-shifting fibers in the endcap region and the first two layers of the barrel, where a higher background is expected.

Trigger. The trigger system of Belle II is important to identify quickly the interesting events during the acquisition, since the detector systems are limited in data storage and bandwith. The system is divided in two levels: an FPGA based Level 1 trigger (L1) and a software based second level, the High Level Trigger (HLT).

The L1 trigger is based mainly on fast track reconstruction in the CDC and on ECL energy, with a latency of 5 µs and a maximum average rate limited to 30 kHz.

The HLT is used to fully reconstruct the events that pass the L1 trigger, with the goal of reducing the event rate to 10 kHz for offline storage. It has access to the event data of all the sub-detectors (except the PXD) and it is designated to identify the region of interest for the readout of the PXD from the reconstructed tracks.

1.4 The Belle II Vertex Detector

The most relevant detector for this thesis is the VXD, which is described with a bit more detail in this section. A summary of the main features of the VXD layers is shown in Table 1.2.

	PXD		SVD			
	L1	L2	L3	L4	L5	L6
Radius [mm]	14	22	39	80	104	135
# Ladders	8	12	7	10	12	16
# Sensors per Ladder	2	2	2	$2+1^*$	$3+1^*$	$4+1^*$
ϕ pitch [µm]	50	50	50	75, (75 to 50)*		
z pitch [µm]	60	80	160	240		
Sensor thickness [µm]	75		320	320, 300*		
Material budget [% X_0]	0.19		0.70			

Table 1.2: Summary of the properties of the VXD subdetectors. The * refers to the trapezoidal, slanted modules of SVD. Data from [7].

PXD. The Pixel Detector (PXD) is the closest detector to the beam pipe, with the first layer placed at a radius of 14 mm, which is advantageous for vertex resolution. The reduced distance from the IP, however, implies a high occupancy, which requires a high granularity detector made with pixel sensors.

PXD (shown in Figure 1.11) is made of two coaxial layers of sensors placed at radii of 14 mm and 22 mm, with a total of ~ 8 million pixels, distributed in a polar acceptance range of [17°, 150°].

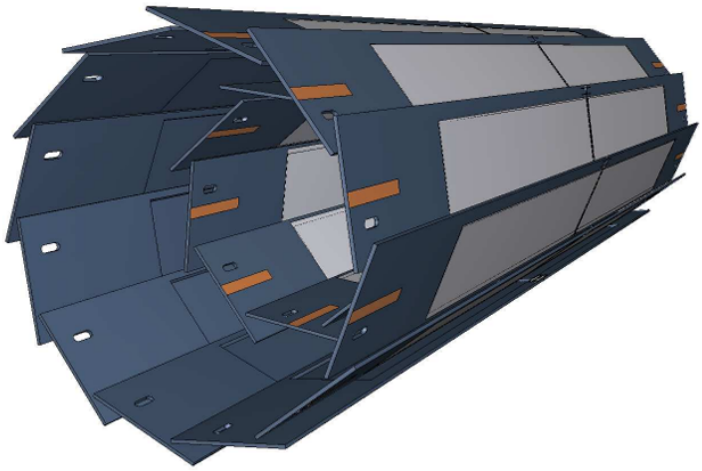

Figure 1.11: Schematic 3-D rendering of the PXD detector.

This detector is composed of 40 modules, glued in pairs and forming eight inner and twelve outer ladders. Each module in the first (second) layer has an area of $1.5 \times 6.8\,(8.5)$ cm^2 and is made of DEPFET (Depleted Field Effect Transistor) sensors (see 3.4.1), placed in a 250×768 matrix. The pixels have a pitch between 50 and 80 µm, depending on the direction and the layer.

To reduce the average material budget to $\simeq 0.2\%\, X/X_0$ per layer, the silicon bulk is thinned to 75 µm, with a 400 µm thick silicon frame, and most of the electronics is integrated with the sensor, with only a part of the readout

electronics placed outside the acceptance region and cooled with a two-phase CO_2 at -20 °C in Run 1 and -25 °C in Run 2. The DEPFET matrix is instead cooled with a flow of nitrogen N_2.

The pixels need to be powered only during the readout, reducing the power consumption, and have a small capacitance, with a very low noise even at room temperature. However, their long integration time (20 µs in rolling shutter mode), excludes PXD from the track reconstruction of the trigger and requires that the tracks reconstructed by SVD are propagated back to PXD to define a region of interest in which the DEPFET pixels can be readout.

SVD. The Silicon Vertex Detector (SVD) is composed of four layers of double sided silicon strip detectors (DSSDs, see Section 3.2), placed at 3.9, 8.0, 10.4 and 13.5 cm radii. Together with the CDC composes the tracking system of the Belle II detector. Its vertex reconstruction capability is also used to define the region of interest in PXD and the detector is also able to reconstruct the vertices of the particles that decay outside PXD, such as K^0_S.

The detector consists of four coaxial layers made by ladders mounted on a lantern-shape barrel, covering a polar acceptance range of [17°, 150°], shown in Figure 1.12. Each ladder is made of a support structure hosting 2 to 5 sensors with their readout chips and cooling support. The sensors are arranged around the beam direction with a windmill-like structure that causes a partial overlap of the sensor active regions (between 2% and 8% depending on the layer). The asymmetric layout accounts for the forward boost from the asymmetric-energy collisions, with the three outer layers inclined with respect to the cylinder axis in the forward region, with angles of 11.9°/17.2°/21.1°, respectively.

The detector was operated at -20 °C during Run 1, with the current value decreased to -25 °C. The cooling is done using two-phase CO_2 transported in stainless steel pipes.

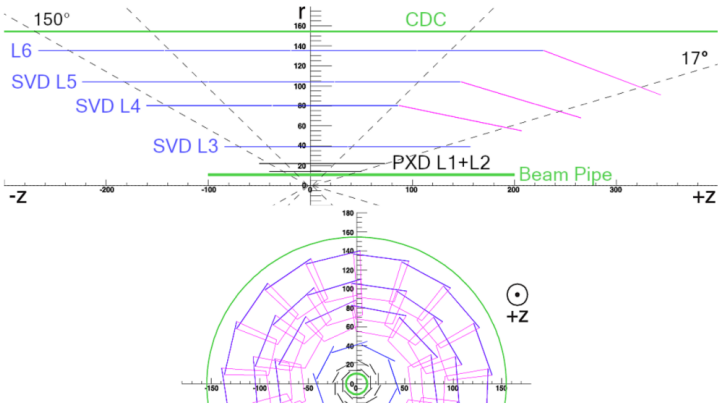

Figure 1.12: Schematic side view of the SVD detector.

To reach a total material budget of ~ 0.6 % X_0 per layer, the strip sensors are 300 µm thick and mounted on a carbon fiber support structure. The innermost SVD layer has a readout pitch of 50 µm in ϕ and 160 µm in z, while the outermost layers have a pitch of 75 µm in ϕ and 240 µm in z; in the tilted forward sensors, which are trapezoidal in shape, the pitch is z-dependent in ϕ, ranging from 50 µm to 75 µm. This allows to reach a spatial resolution of 7 to 12 µm (p-side) and 15 to 25 µm (n-side), while the fast readout allows to reach a cluster time resolution of $\mathcal{O}(2\,\text{ns})$. The excellent time resolution also results in a relatively high maximum occupancy (6%).

Its great cluster time resolution makes it the reference detector for determining the event's T_0.

The use of DSSDs reduces the amount of readout channels but the high particle rate requires a readout chip with a fast shaping time. For this reason the APV25 chip [8] was chosen, thanks to its low-noise preamplifiers and shapers for 128 channels and its shaping time of 50 ns, which minimises the hit occupancy from beam-induced background. The strips on the top side of the chips are connected to the readout chips using a planar pitch adapter, while the strips on the bottom side are routed to the chips via a flexible pitch adapter wrapped around the edge of the sensor. Placing all the chips on one side of the sensors makes it possible to cool the APV25 chips in each layer using a single cooling pipe, minimising the material budget.

For luminosity and beam monitoring, a total of 20 diamond sensors are placed around the beam pipe and inside the VXD volume.

Cooling The cooling CO_2 plant supplies a two phase CO_2 to the VXD system (SVD and PXD) up to a rate of 30 $\text{g}\,\text{s}^{-1}$. The reasons for the choice of the CO_2 for the cooling fluid are listed in the following:

- The liquid CO_2 has a large latent heat, which allows cooling with a lower flow compared to water.
- The viscosity of the liquid CO_2 is small, allowing the use of small-diameter tubes for coolant circulation. For the SVD, the inner tube diameter is only 1.5 mm.
- A wall thickness of 0.05 mm provides sufficient pressure margin, which also concurs in keeping the material budget low.

During Run 1 the plant was operated at a temperature of -20 °C. After the completion of the installation of the PXD in LS1, the temperature has been lowered to -25 °C to compensate for the increased power consumption.

Performance. Currently the VXD is running with the sole SVD turned on, due to significant damage inflicted by two Sudden Beam Loss (SBL) events to the PXD that prompted the team to preventively turn it off to avoid further damage. SBL events are very fast losses of most of the beam with subsequent damage to the detector due to the sudden increased hit rate. In particular, after 2024, 2% of the PXD pixels do not function anymore. A fast power off procedure is being developed for the PXD to improve its safety against SBLs, which are still not completely understood.

The SVD detector, instead, is operating stably with all the layers with a hit efficiency $> 98.5\%$ and low occupancy ($< 1\%$), and manages to also smoothly deal with the higher background due to injection. While the background occupancy is increasing (from $\sim 0.6\%$ to $\sim 0.8\%$ in the innermost layer during the operation in 2024), it is still well below the limits for efficient operation.

Furthermore, during the operation in 2024, the worse injection background conditions, mainly due to relaxed thresholds on the radiation monitoring diamond detectors, led to an increase of configuration errors of the APV25 chips due to Single Event Upsets (SEUs). However, countermeasures will be taken in the upcoming runs, mainly to reduce the impact of the reconfiguration of the chips on the run time.

Chapter 2

Belle II Upgrade

This chapter describes the upgrade project of the Belle II experiment and the plan to install major components during Long Shutdown 2, currently scheduled for 2032. Starting from the motivations, in particular the expected background, it then presents the requirements and the main elements for the upgrade of the Interaction Region, the VXD and the CDC. Finally, a description of the new vertex detector (VTX) is provided.

2.1 Motivation

The ambitious physics goals set by the experiment require a significant improvement of the accelerator and the detector to reach the target luminosity of 6×10^{35} cm^{-2} s^{-1}. In the current configuration, the SuperKEKB accelerator is expected to reach a maximum instantaneous luminosity of $\sim 2 \times 10^{35}$ cm^{-2} s^{-1} in 2032. A modification of the Interaction Region (IR) is required to improve the accelerator performance, mainly by using a new superconducting final focus quadrupole magnet system (QCS), with a reduced distance between the Interaction Point and the last magnetic element.

A redesign of the IR, however, will also require a redesign of the vertex detector, since the VXD is attached to it to improve the vertexing resolution. Furthermore, even if the current IR was kept, simulations have shown that the increased background would cause occupancy levels in the vertex detector over its operating limits.

These reasons have motivated the need for a new vertex detector with increased safety margins against beam background and better resolution, with the opportunity to improve physics performances.

During the LS2 it will also be possible to upgrade other detectors, for example the CDC, with improvements of the tracking performance and radiation hardness [4].

Background. The background sources described in Section 1.2.2 are one of the main limiting factors to the operation of the accelerator. Both single-beam and luminosity background will significantly increase at the target luminosity, requiring a careful evaluation of the impact on the subdetectors' performance.

Studies to monitor the status of the background are conducted regularly by operating the HER and LER individually and together with different beam currents. The results from one of these studies are presented in Figure 2.1 for the various detectors and machine components near the IR. In general, it is not straightforward to distinguish the various background components and the uncertainties are large.

From these studies an extrapolation of the expected background in 2032 has been performed, with three different scenarios evaluated for the operation after LS2 depending on the not-so-easily-simulated evolution. In particular, three different scaling factors have been implemented, starting from the background extrapolated with the current optics before LS2:

- Scenario-1: optimistic, in which the single-beam background components from before LS2 are scaled with a $\times 2$ scaling factor to target beam parameters.
- Scenario-2: intermediate, with a $\times 5$ scaling factor on the single beam background components.
- Scenario-3: conservative, with a $\times 10$ scaling factor, in which all the single-beam backgrounds are scaled by an order of magnitude.

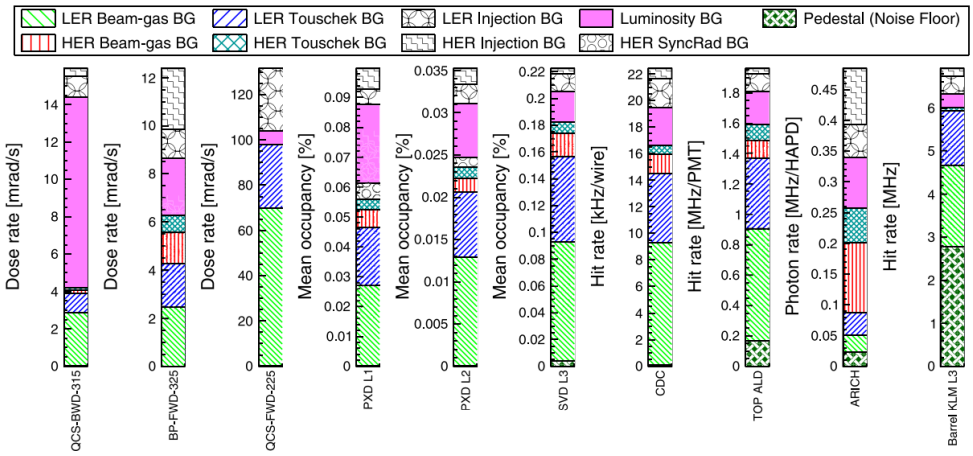

Figure 2.1: Beam background composition from a study in June 2021.

In all scenarios the luminosity backgrounds are simply scaled with the luminosity increase. The estimated background rates at the target luminosity are shown in Figure 2.2 for the detectors, with the safety margin (defined as the maximum allowed rate divided by the expected background rate) for the Scenario-2 highlighted in the boxes.

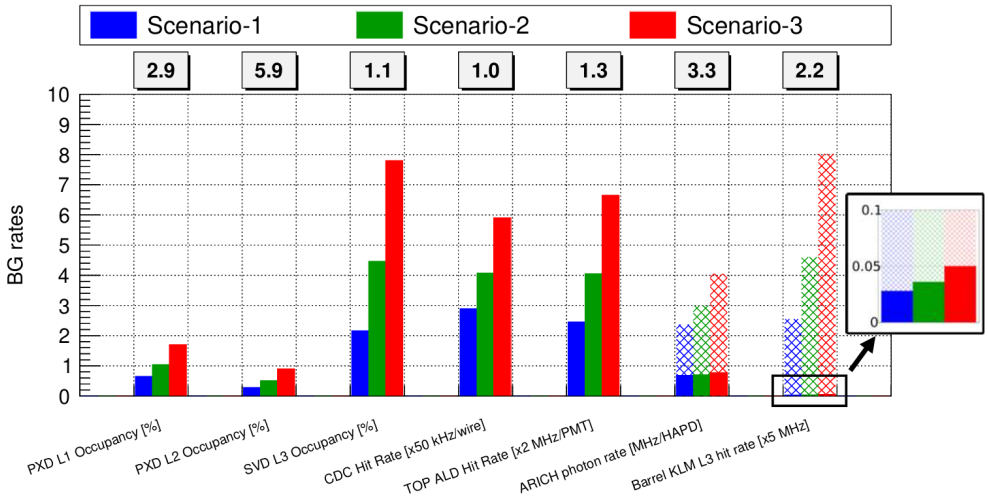

Figure 2.2: Estimated beam background for the three scenarios at the target luminosity for all the detectors. The number in the box is the safety margin for the detectors at the Scenario-2.

As shown, three detectors will operate very close to the maximum rate: the SVD, CDC and TOP detectors. For the TOP the operation outside the safety margins only means a reduced lifetime of the MCP-PMTs, which are replaceable albeit expensive. For the SVD and the CDC the situation is more critical. For the CDC, which is vital for charged particle tracking, high background causes not only reduced "operational" efficiency and worse resolution, but also permanent damage to the wire and may lead to discharges that require turning off a portion of the chamber. Its future upgrade or, at least, refurbishing is under discussion.

The SVD, on the other hand, will have a worrisome 8% occupancy in its first layer in Scenario 3, which would hinder its tracking capabilities. Its upgrade is therefore seen as a crucial step toward achieving the desired physics and performance goals. The upgrade of the vertex detector is also motivated by the possible change in the IR geometry, that would make the current detector unusable.

2.2 Overview of the Belle II VXD upgrade

The vertex detector upgrade is strongly linked with the redesign of the Interaction Region, as discussed in the following.

2.2.1 Interaction Region

The interaction region (IR) of the SuperKEKB accelerator is designed to achieve extremely small beta functions at the Interaction Point, both in horizontal and vertical directions, thanks to the superconducting magnets QC1s and QC2s that provide the focusing magnetic field.

The current design (shown in Figure 2.3) employs superconducting compensations solenoids (anti-solenoids) to compensate for the solenoid field of the Belle II detector, such that:

$$\int_{\mathrm{IP}} B_z(s)ds = 0 \tag{2.1}$$

where B_z is the magnetic field along the solenoidal axis and s is the distance from the IP.

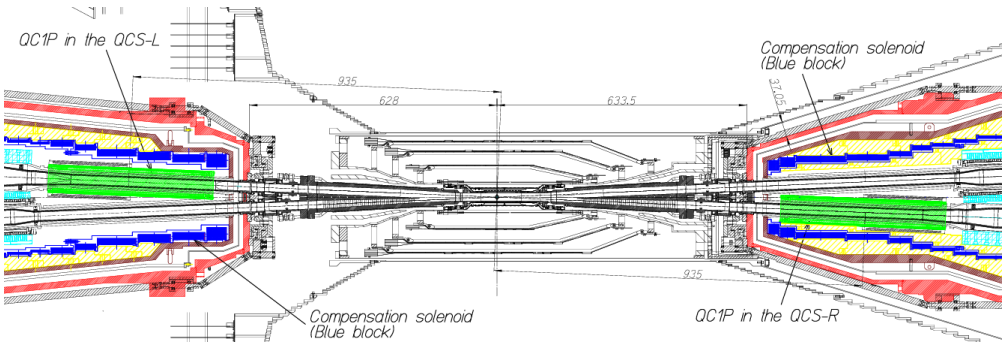

Figure 2.3: Current design of the SuperKEKB IR. The vacuum vessels of the cryostat (red), the liquid helium vessels (brown), the tungsten radiation shields (yellow), the anti-solenoid coils (blue), the magnetic yokes/shields (cyan) and the QC1P magnets (green) are shown.

However, the presence of a 83 mrad angle between the two beams ($\pm$41.5 mrad with respect to the solenoidal axis), introduces a transverse component of the magnetic field across the orbit $B_x(s)$. The presence of this component causes a chromatic (i.e. energy dependent) coupling between the horizontal and vertical motions of the particles in the beams and increases their dispersion.

A correction of these effects is currently applied by dedicated quadrupole and dipole magnets on each side of the IP, with a further correction to the coupling in the LER applied by a rotatable sextupole magnet. However, the incomplete vertical dispersion compensation results in a vertical emittance (i.e. how much the beam particles are spread out) that is strongly dependent on $B_x(s)$. To minimize it, it is necessary to reduce the $B_z(s)$ differential along the beam trajectory [4].

In order to do so, the IR will be upgraded, making the beam trajectory as parallel to the QC1 magnet axis as possible to reduce the chromatic horizontal-vertical coupling, while also modifying the $B_z(s)$ profile. These goals will be achieved bringing the QC1P magnet closer to the IP by 10 cm and adapting the magnets to the requirements on the field.

The latest version of the future IR is shown in Figure 2.4. A closer QC1P magnet requires also a closer cryostat and additional detector shielding, which will interfere with the support structure of the current vertex detector. A closer QC1P magnet also means that a more compact design must be employed, to avoid reducing the solid angle acceptance of the detector. A dedicated R&D program is ongoing to test the feasibility of using the more resilient material Nb_3Sn for the superconducting cables, instead of the current NbTi. I will not discuss this any further, as it is beyond the scope of this work

2.2.2 VXD

The upgrade of the VXD aims at coping with the increased machine background at higher luminosity, while improving the physics performances at the same time. The path chosen in this direction was to use pixelated CMOS fast sensors, in particular the Monolithic Active Pixel Sensors (MAPS), reducing the occupancy level and increasing the tracking efficiency and the resolution.

The new detector will also have to comply with specific radiation resistance requirements to work in the high-radiation environment after LS2. In particular, these requirements are, for 10 years of operation:

- Hit rate capability: 120 MHz cm^{-2}.

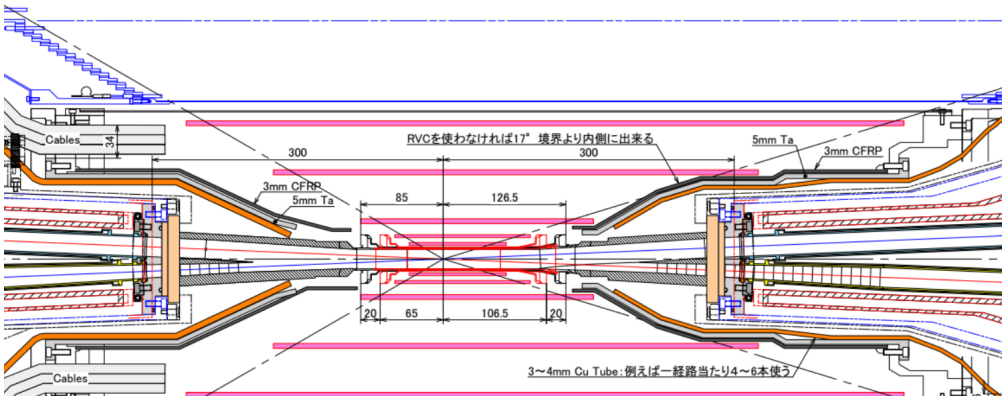

Figure 2.4: Current design of the upgraded SuperKEKB IR.

- Total Ionizing Dose: 10 Mrad, 100 kGy.
- NIEL fluence: 5×10^{14} 1-MeV-n_{eq}/cm^2.

To put these values in perspective, they are similar to the requirements of the outer layers of the Inner Tracker of the ATLAS experiment and of the Outer Tracker of the CMS experiment at LHC. In these detectors, after the upcoming upgrade to prepare for the high luminosity runs, the total NIEL dose (for ~ 10 years of operation) will be of $\sim 3 \times 10^{16}$ 1-MeV-n_{eq}/cm^2 for the inner layers and $\sim 0.9 - 1.2 \times 10^{15}$ 1-MeV-n_{eq}/cm^2 for the outer layers. Similarly, the Total Ionizing Dose will be ~ 1.2 Grad in the inner layers and ~ 50 Mrad in the outer layers [9–12]. Note that the fluence can significantly change depending on the layer of the detector (as in Belle II), so the listed values are the maximum ones for each subdetector.

The VerTeX detector (VTX), the upgrade of the VXD, consists of 6 concentric layers of MAPS with a barrel geometry, operated at room temperature to decrease as much as possible the material budget due to the cooling setup. Its main targets are a significant reduction (two orders of magnitude with respect to PXD) of the integration time, lower detector occupancy, better tracking efficiency and improved momentum and impact parameter resolution at low transverse momentum.

The choice of the CMOS MAPS as the sensor for the new detector, together with the requirements, prompted the development of a new pixel sensor, called OBELIX (Optimized BELle II pIXel sensor). This sensor uses a modified TowerJazz 180 nm CMOS process and it is based on the TJ-Monopix2 sensor, whose characterization is the main topic of this thesis and is presented in Chapters 5 and 6.

The dimensions of OBELIX are 29.60×15.33 mm^2, with 33.04×33.04 µm^2 pixels. A single device type will be used in all VTX layers, with different geometrical arrangements as discussed below.

2.3 The VTX Project

The need for a new vertex detector has prompted the design of the VTX detector, comprised of 6 straight barrel shaped layers of pixelated sensor to cover the angle of acceptance $18.3° < \theta < 150°$, dictated by the upgraded QCS. The layers can be divided in two groups: an inner part (iVTX), with 2 layers, and an outer part (oVTX), with 4 layers and a separate mechanical structure.

The initial design was developed with 5 layers, out of space considerations. To accomodate the sixth layer in the oVTX, staggered layers are employed. The design with 6 layers shows improvements in all the properties with respect to the original 5-layers one, with the sole exception of a slight increase in the vertex resolution, due to the increased material budget.

2.3.1 Mechanical structure

In Figure 2.5 the VTX detector is shown in its 6-layers configuration, while in Table 2.1 a summary of its properties is provided. For the oVTX, the two radii of the staggered layers are provided, respectively corresponding to the odd and even ladders.

In the initial design air cooling was chosen for the iVTX layers but it has shown to be unfeasible due to a too high operating temperature with respect to the specifications provided by the tests on TJ-Monopix2. For this reason,

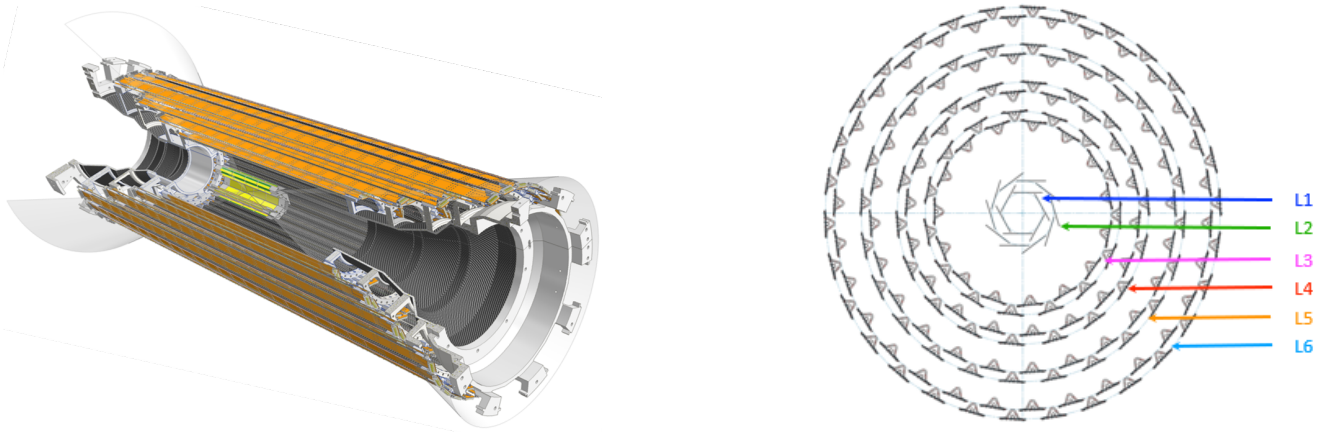

(a) 3-D rendering of the VTX detector.

(b) Schematic cross section of the VTX detector.

Figure 2.5: The VTX detector.

	L1	L2	L3	L4	L5	L6	Unit
Radii	14.1	22.1	62.5/69.0	82.5/89.0	108.0/114.5	133.5/140	mm
# Ladders	6	10	30	36	48	60	
# Sensors per Ladder	4	4	12	16	20	24	
Hit rate (Sc-1)	14.1	5.6	0.42	0.28	0.16	0.11	$\mathrm{MHz\,cm^{-2}}$
Hit rate (Sc-2)	21.2	9.4	0.68	0.45	0.25	0.17	$\mathrm{MHz\,cm^{-2}}$
Hit rate (Sc-3)	34.0	16.2	1.12	0.76	0.40	0.26	$\mathrm{MHz\,cm^{-2}}$
Material budget	0.3	0.3	0.8	0.8	0.8	0.8	% X_0

Table 2.1: Summary of the properties of the VTX geometry with 6 layers and staggered layers in the oVTX. The two radii quoted are referred to the two radii of each staggered layer [13].

new approaches are under discussion for the iVTX: an active cooling, with the use of a liquid coolant distributed with dedicated pipes (which increase the budget material), or a passive one, with the use of pyrolythic graphite to disperse the heat more easily, thanks to its great thermal conductivity (up to 1800 $\mathrm{W\,m^{-1}\,K^{-1}}$).

While the latter would reduce the complexity of the cooling setup, the radiation hardness of the material is under testing to ensure that it can mantain its properties in a range compatible with the VTX requirements.

The iVTX ladders are optimized for the lowest material budget possible, with an average 0.3 % X_0 material budget. These ladders are entirely made in silicon, hosting four OBELIX chips each. These sensors are diced out together from the production wafer and remain independent, while a redistribution layer (RDL), added to the ladder after the production, connects the sensors electrically.

This RDL consists of multiple metal and dielectric layers and allows the placement of passive components, such as decoupling capacitors. The ladder is then thinned down inhomogeneously, with a 40 µm thickness under the sensor and 400 µm around them and on the ends of the ladders to ensure mechanical stability. A sketch of this concept is shown in Figure 2.6.

The oVTX ladders, instead, uses a more standard approach, similar to the one used for the ITS2 of the ALICE experiment at CERN [15], because they can not be self-sustaining due to their larger dimensions with respect to iVTX.

The mechanical support is given by a 3-D carbon fiber structure and cold plate, which is coupled to the pipes for the circulation of the coolant on one side and glued to the sensors on the other. Flex PCBs glued on top of the sensors ensure the electrical connections, with adaptions made case by case for the four layers, depending, for example, on the space needed by the machine components.

In Figure 2.7, a schematic of the ladders for the last two layers of the original oVTX design is depicted, which is very similar to the one used in the current staggered version.

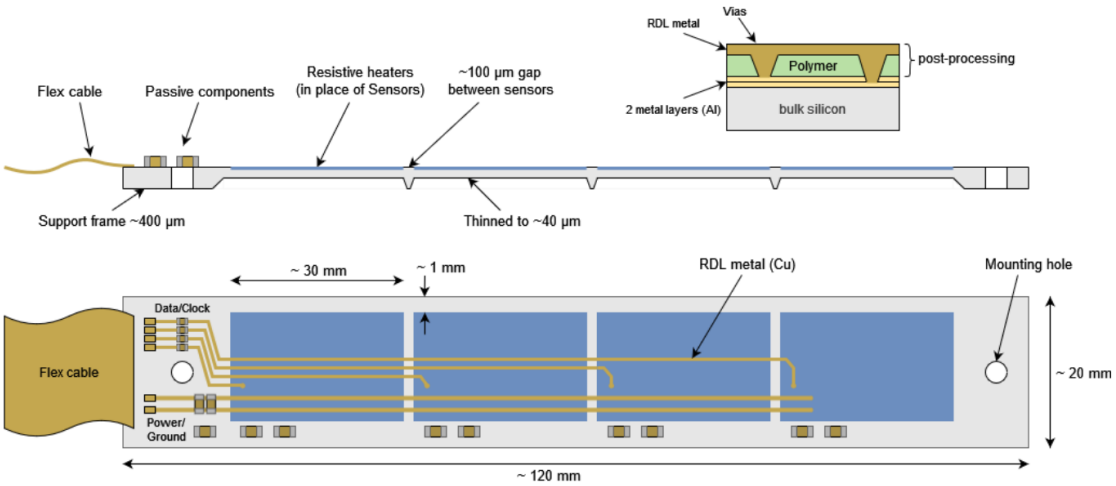

Figure 2.6: Sketch of the all-silicon ladder concept of the iVTX. Four sensors (blue) are on the silicon support (grey), with power and data transimission lines (yellow) transmitted by a flex cable [14].

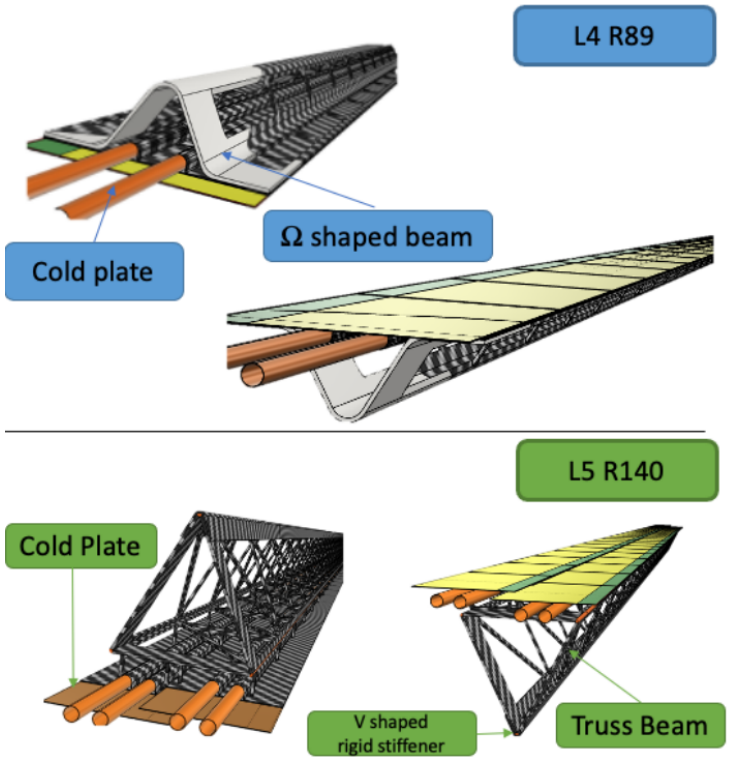

Figure 2.7: Sketch of the ladders for the layer 4 and 5 of the original 5-layers VTX, very similar to the ones used in the current version of oVTX. The active area (yellow) and the chip's periphery (green) are shown, together with the cooling pipes (orange) [14].

2.3.2 Physics performance

The VTX upgrade aims at significantly improving the physics performance of the vertex detector and of the Belle II experiment as a whole. The premature increase of the CDC occupancy has shed a worrying picture on the tracking efficiency evolution after LS2 if the chamber remains the reference detector.

As shown in Figure 2.8, the tracking efficiency relying only on the CDC decreases dramatically with higher background scenarios. This decrease is partially mitigated by including the current SVD in the tracking, but the drop in the scenarios with higher background is still present. The VTX (in Figure 2.8 the data are from the original

5-layers geometry, but the 6-layers one has similar behaviour), however, can almost completely compensate the drop due to the increased CDC occupancy. The efficiency is kept almost constant for the three scenarios, with a much smaller drop in the conservative one with respect to the CDC-only and CDC + SVD configurations.

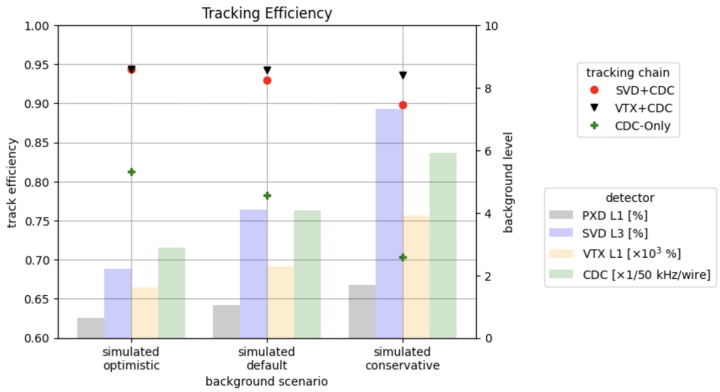

Figure 2.8: Comparison between the tracking efficiency in the three possible scenarios when using only the CDC, the CDC and the current SVD and the CDC with the 5-layers VTX [4].

Many tests have been conducted on the 5 and 6-layers geometries, to compare their reconstruction efficiency of the K^0_S and π^-_{soft}, together with the resulting vertexing resolution.

Regarding the reconstruction efficiency of the π^-_{soft}, simulations have shown a significant improvement for both geometries with respect to the current VXD, with better results for the 6-layers than the 5-layers configurations, as shown in Figure 2.9. Note that the material budget considered for the simulation of the 6 layers is the best-case scenario but more realistic values are consistent and only show a slight reduction, mantaining the advantage with respect to the 5 layers.

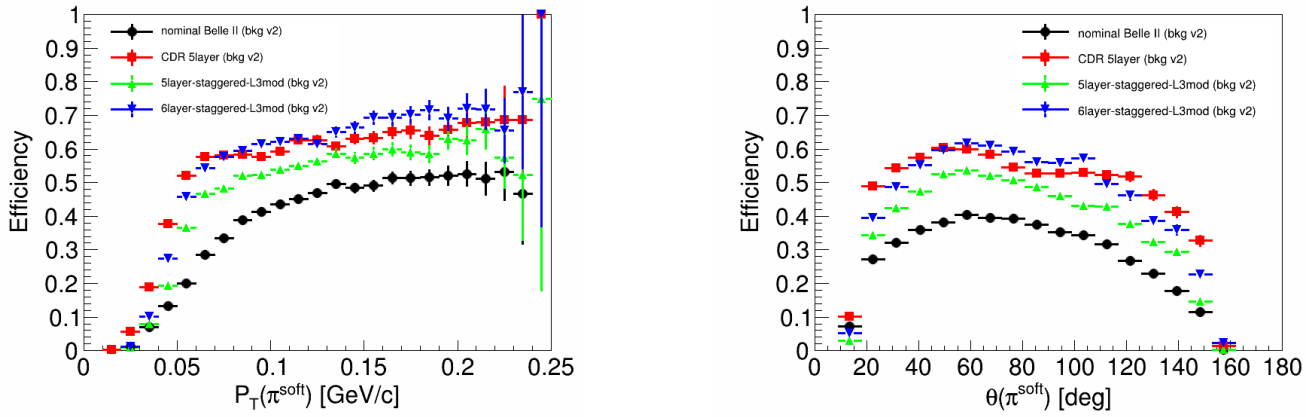

(a) Dependence on transverse momentum.

(b) Dependence on the angle.

Figure 2.9: π^-_{soft} reconstruction efficiency for the current VXD, the original VTX design (now abandoned) and the geometries with 5 and 6 layers.

The comparison between the two configurations has also been performed for the reconstruction of the K^0_S, from simulated $B^0 \to J/\psi K^0_S$ processes. The results are shown in Figure 2.10.

The 6-layers geometry shows a more consistent reconstruction efficiency in the decay length than the 5-layers one, which presents a drop at the position of the L3. Beyond about 10 cm, the reconstruction is dominated by the CDC and shows little dependence on the vertex detector design.

Notably, the reconstruction efficiency for the K^0_S is reduced of about 5% in the 5-layers geometry with respect to the VXD, mainly because the current detector has one layer more. This was one of the main reasons that prompted the study for a 6-layers geometry.

Furthermore, Figure 2.10 also shows the comparison between the different material budget configurations for iVTX and oVTX, which are however rather consistent.

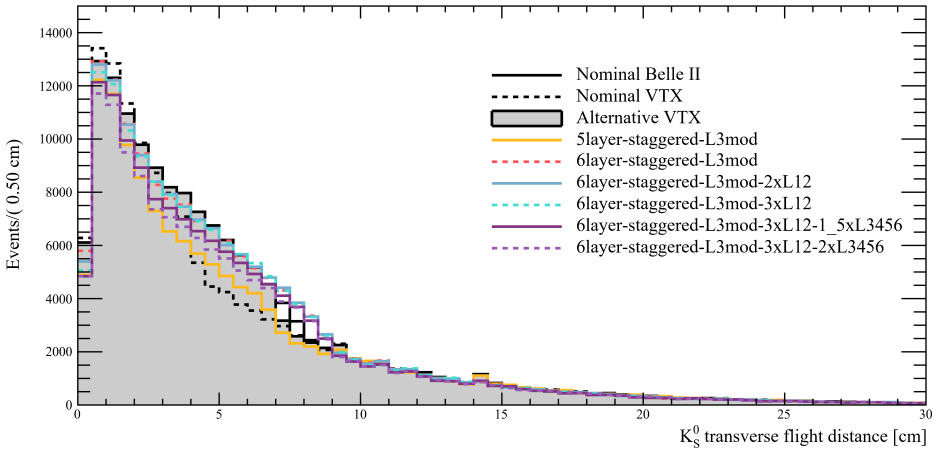

Figure 2.10: Number of K^0_S reconstructed versus flight distance for the various VTX configurations. The different 6-layers configurations correspond to different contributes to material budget from iVTX and oVTX.

The only parameter in which the 6-layers VTX is worse than the 5-layers one is the vertexing resolution, due to the additional layer and material. The results (Table 2.3) come from the same $B^0 \to J/\psi K^0_S$ events used before and are, however, still better than the current VXD resolution and do not seem to be much affected by the increasing background in the different scenarios.

The 6-layers configurations listed in Table 2.2 refer to different material budgets, depending on the cooling and the mechanical support of the layers.

	iVTX [% X_0]	iVTX [% X_0]
Optimistic	0.1	0.4
Engineering design	0.3	0.6
Pessimistic	0.3	0.8

Table 2.2: Material budget for possible VTX configurations for the iVTX and oVTX.

The pessimistic scenario has been chosen as the reference one.

B_{sig} z vertex resolution [µm]	Bkg(v1)	Bkg(v2)	Bkg(v3)
Belle II	20.9	22.3	24.5
Nominal VTX	13.9	14.0	13.9
Alternative VTX	13.7	13.7	13.6
5-layers staggered	16.7	16.1	16.4
6-layers optimistic	16.1	16.1	16.1
6-layers engineering design	19.0	19.0	19.0
6-layers pessimistic	19.1	19.1	19.1

Table 2.3: Resolution for the VXD and different geometries of the VTX. Nominal and alternative VTX refer to the 5-layers design with different position of L3. The description of the 6-layers geometries is in the text. Results partially from [4].

Furthermore, the oVTX layers can be added in the trigger process already from the L1, reducing the impact of the shortcomings of the CDC in terms of background rejection.

2.3.3 Sensor specifications

The requirements for the sensor used for the VTX upgrade matched well with the use of TJ-Monopix2 as a prototype for OBELIX. Some of these requirements and their implementation in OBELIX are briefly listed in the following.

The first one is the resolution, which needs to be below the current 20 µm: for this reason a spatial resolution of ≈ 12 µm is needed, which is achieved with the mere binary information of the hit of a pixel. Thanks to the 33.04

µm pixel pitch the resolution is $33.04/\sqrt{12} \approx 9.5$ µm even without using cluster charge information.

Another requirement is the reduced material budget, satisfied by OBELIX thanks to its 30 µm epitaxial silicon, which allows to thin the sensor down to 40 µm [13].

One of the main reasons for this upgrade is the increased estimated occupancy due to an increased hit rate. The OBELIX sensor is designed to sustain a hit rate of more than 120 MHz cm^{-2}, which is more than 3 times the amount estimated for the innermost layer (34 MHz cm^{-2}), also thanks to its triggered operation, which reduces the registered background. Due to sudden background increases due to injection background, the matrix should also be able to withstand rapid burst at a hit rate of 600 MHz cm^{-2}.

To take part in the triggering and allow more complex algorithms already at the L1 stage, the sensor's latency should be at least 10 µs (double the current Belle II value), which has also been implemented in OBELIX, together with an integration time below 100 ns (two timestamps of 47.1 ns will be merged for the readout). The timing performance is also critical to substitute the SVD in the event T_0 determination, which is possible thanks to the timing resolution below 3 ns.

Finally, the sensor needs to sustain the expected radiation dose, cited in Section 2.2, which has been proven by dedicated tests on TJ-Monopix2, presented in this thesis.

2.3.4 Timeline

The timeline is strongly dependent on the development of the OBELIX sensor (Section 4.3). The current schedule sets to the start of 2030 the production phase and to the half of the 2032 the start of the installation and commisioning.

As in all complex chip design projects, there is a significant risk that multiple submissions are required to arrive at a fully functional design. In this respect, the TJ-Monopix2 characterization work carried out in this thesis is relevant to inform the OBELIX design and increase the chances of a timely completion of the project.

Chapter 3

Semiconductor particle detectors

This chapter focuses on semiconductor detectors, starting from the description of the p-n junction in semiconductors to then move to the movement of the charges and the formation of signals on the electrodes. Some relevant silicon detector technologies are then described, followed by discussion of temperature and radiation effects on these sensors. Note that most of the material in this chapter derives from [16].

3.1 p-n diode as a detector

Solids can be divided in three categories depending on their electrical conductivity: conductors, semiconductors and insulators. In the solid state lattice the atoms are so densely arranged in a periodic manner that some of their energy levels have gaps of the order of meV. These levels can be considered as a single energy band, in which the electrons can flow freely, separated from the other bands by a band gap.

The two highest bands are the valence band and the conduction band, with the latter with the highest energy. The characteristic amplitude of their band gap is what categorizes the solids: for insulators it is typically $\sim 9\,\text{eV}$, in semiconductors it is smaller (e.g. 1.12 eV for silicon), while for conductors the conduction and valence bands (at least) partially overlap, as can also be seen in Figure 3.1.

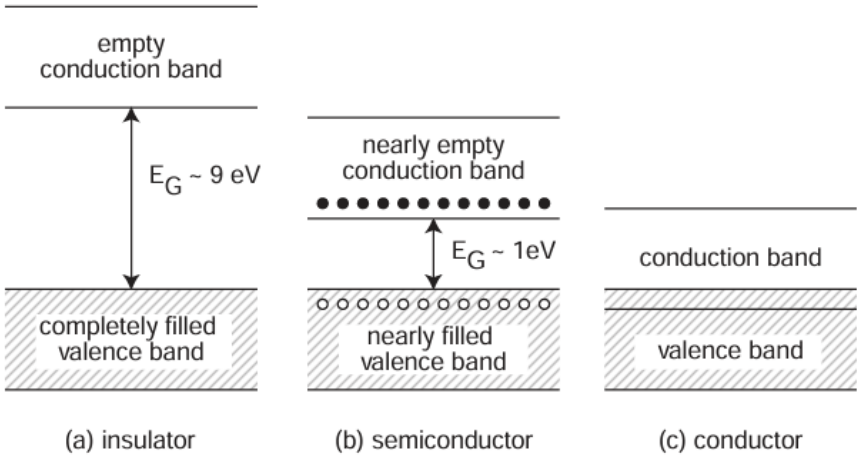

Figure 3.1: Schematic energy band structure of insulators (a), semiconductors (b) and conductors (c).

Semiconductors. Semiconductors are often tetravalent chemical elements, such as silicon or germanium.

When charged particles traverse materials, they lose energy by ionizing the atoms of the medium, forming couples of charge carriers of opposite charge. In semiconductors the charge carriers are electrons and holes and the relatively small energy band allows to convert the deposited energy in a charge high enough to be detected.

In particular, the most used semiconductor for particle detectors is silicon, due to its use in consumer electronics industry and its low band gap (1.14 eV), which requires only 3.65 eV for the production of a electron-hole pair,

while making the detector operable at room temperature. By applying an electric field, the produced carriers drift towards their relative electrode: holes (positive) towards the cathode and electrons (negative) towards the anode, which sense the signal induced by this movement.

Semiconductors can be doped with certain chemical elements that change their charge carriers distribution. Typical elements are P or As, called donors (n-doping), which are pentavalent elements that added in the tetravalent semiconductors increase the number of conduction electrons, or B, Al, called acceptors (p-doping), which are trivalent elements that increase the number of holes. Notably, the doped semiconductor remains neutral. A representation is given in Figure 3.2.

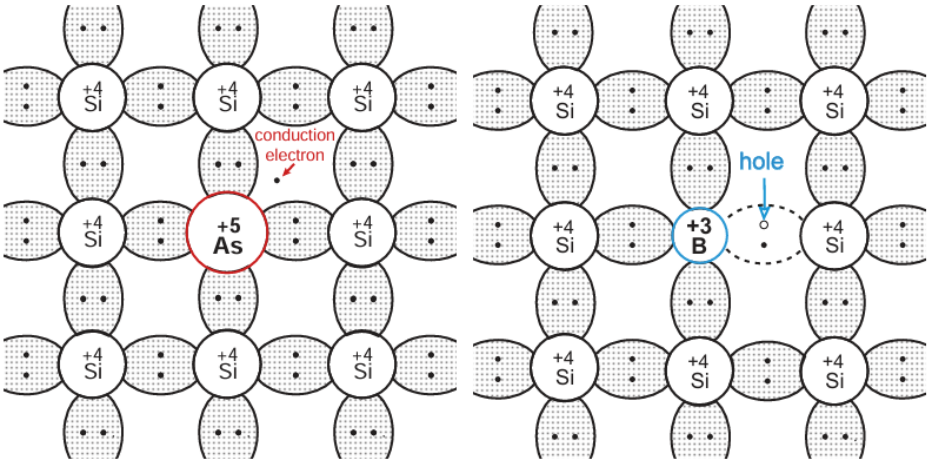

Figure 3.2: Schematic representation of n-doped and p-doped silicon.

p-n junction. When two semiconductors with opposite doping are in contact, a p-n junction is formed. The excess of holes in the p-semiconductor and of electrons in the n-semiconductor generates a density difference across the junction, which causes the diffusion of the charge carriers from one region to the other. In this way the charges recombine at the junction, creating a region without free carriers called depletion zone. Differently from the semiconductor outside, the depletion zone has a space-charge that depends on the type of doping: it is positive in the n-layer and negative in the p-layer. Their opposite sign generates an electric field that counters the initial diffusion current. A schematic of the p-n junction is given in Figure 3.3.

The width of the depletion zone can be varied by applying an external voltage V_{ext} to the two sides of the junction. A positive voltage applied to the p-side (forward bias) reduces the depletion region, while a negative voltage applied (reverse bias) increases it. The same happens with voltage with the opposite sign applied to the n-side.

3.1.1 Semiconductor detectors

The typical structure of semiconductor detectors is a reverse biased p-n diode, in which the depletion region is the active volume and the diode terminals are the charge collection electrodes.

Charge motion. When a charged particle ionizes the bulk of the detector, the charge carriers pairs are separated by the electric field applied and start to drift towards the respective electrode, with a drift velocity that depends on the carrier mobility μ:

$$v_D = \mu(E)E \tag{3.1}$$

which has a typical value of $\sim 50\ \mu\text{m}\,\text{ns}^{-1}$ in silicon detectors.

When carriers are not produced in the depleted region, they usually move by diffusion. This process arises from a concentration gradient and thermal motion, in which the particles tend to move in the opposite direction with respect to the concentration gradient. Higher temperatures and mobilities linearly increase the diffusion constant D, the quantity that parametrizes this effect.

If multiple charges are created together as a charge cloud, the size of the cloud increases over time due to diffusion, with a width σ:

$$\sigma = \sqrt{2Dt} \tag{3.2}$$

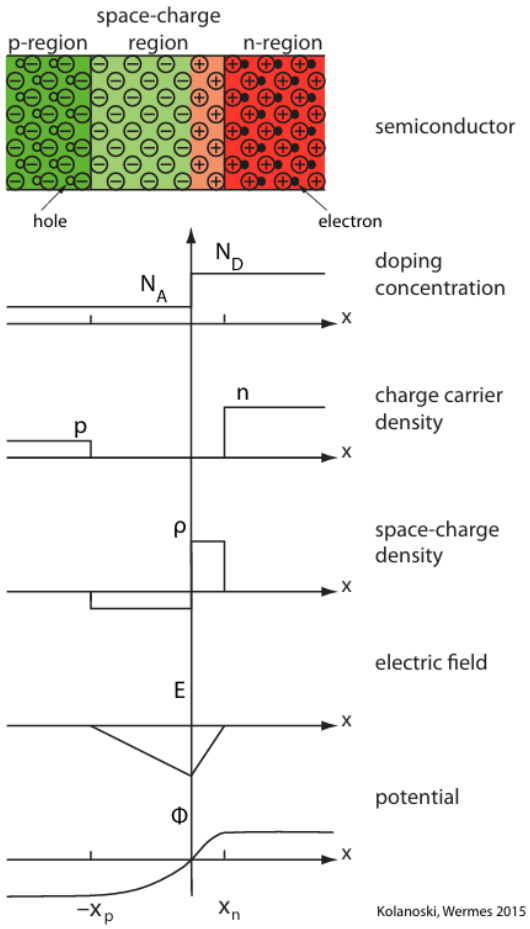

Figure 3.3: Schematic representation of the p-n junction, with doping and charge densities and electric field and potential depicted.

Notably, if σ is greater than the readout electrodes of the sensor, the diffused charge is readout by multiple electrodes, creating charge clusters signals.

Creation of the signal on the electrode. The movement of the charges, either via diffusion or drift, induces a signal on the electrodes, according to the Shockley-Ramo theorem. According to it, the induced current i on an electrode is given by:

$$i = q\vec{E}_{\mathrm{w}} \cdot \vec{v}_D \tag{3.3}$$

where $\vec{E}_{\mathrm{w}}$ is the weighting field, which corresponds to the electric field if the charge q were not present and a unitary voltage was provided to the electrode.

Integrating Equation 3.3 over the path of the charge carrier, it is possible to obtain the induced signal charge on the electrode. Its value mostly depends on the width of the detector and the energy of the traversing particle and follows a Landau distribution. In silicon, the average value of produced couples by a MIP is $\approx 107\ \mu\mathrm{m}^{-1}$, while its most probable value (MPV) is $\approx 77\ \mu\mathrm{m}^{-1}$. This implies thatfor a typical sensor thickness of 300 µm the average signal is $\approx 32000\, e^-$, while the MPV is $\approx 23000\, e^-$. A larger charge usually allows for an easier detection, with less constraints on the noise of the detector, while thinner sensors (such as Monolithic Active Pixel Sensors, Section 4.1) have smaller signals ($\sim 0.1\times$ these) and need to reduce the noise as much as possible.

3.2 Strip Detectors

One of the earliest silicon sensor technology to be developed was the silicon strip sensor, in which an array of long and thin electrodes is employed to get one-dimensional position information. Usually the doped silicon strips are implanted in a substrate with opposite doping, to increase the depletion region below them.

The readout is carried out by metal strips on top of the doped region, with the electronics placed at one (or both) end of the strip. If the metal is directly in contact with the doped strip the readout is directly coupled (DC) and the preamplifier of the readout must compensate the leakage current; if, however, between the metal and the strip there is a dieletric (i.e. SiO_2), this acts like a capacitor and blocks the DC leakage current. A representation is given in Figure 3.4, highlighting the circuit logic of the two couplings.

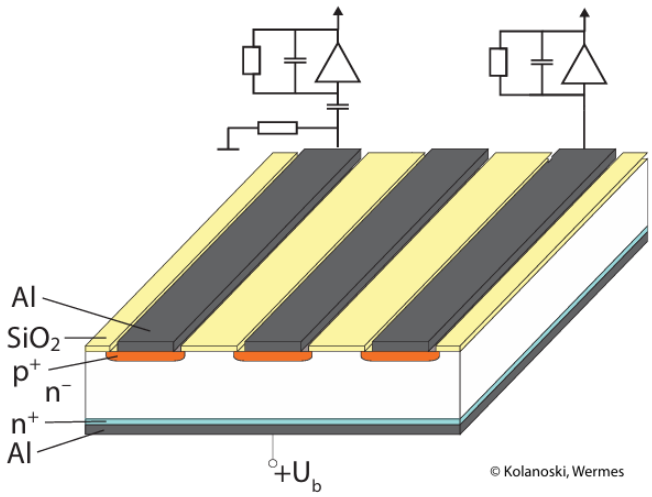

Figure 3.4: Representation of a strip sensor with the capacitively (AC, left) and direct (DC, right) coupling.

To have spatial information on two dimensions, a second detector can be placed on top of the first one with an angle between their orientations or a double sided silicon strip detector (DSSD, shown in Figure 3.5), can be employed. In the latter, strips with opposite doping are implanted on the two sides of the bulk, in two different directions. This allows to get positional information from charge collected in the same bulk material, thus reducing the material budget.

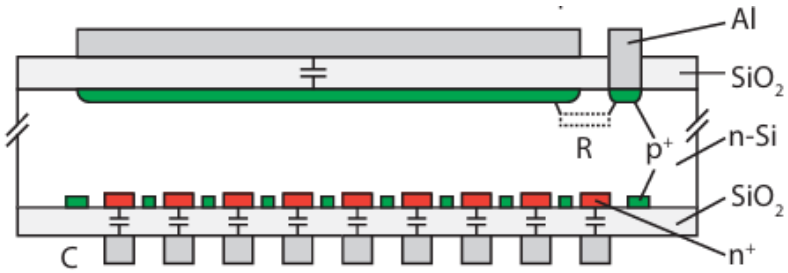

Figure 3.5: Cross section of a double sided strip sensor, showing both p (green) and n (red) implants.

Many experiments use strip sensors for their detectors, either in the single-sided (ATLAS, CMS) and the double-sided (Belle II) configurations.

3.3 Hybrid pixel detectors

Requirements from high occupancy environments prompted the development of detectors segmented in both directions that could sustain higher occupancy, the pixel detectors. The pixel pitch can vary from few tens to hundreds of microns, depending on the application.

Depending on the technology employed, the pixel detector can be either hybrid or monolithic. In this section the hybrid one is presented, while the monolithic is presented in the next one.

The hybrid pixel detector is made of two separate parts with different functions: the pixel sensor, which is the sensing element, divided in pixel cells, and the readout chips, which have the same pixel structure and are bump bonded to the respective pixel. A cross section is shown in Figure 3.6, showing its different elements.

Since the two layers are developed separately, they can be optimized for their individual requirements. While the sensor is produced from low-doped high-resistivity silicon wafers that can be depleted with a relatively low voltage,

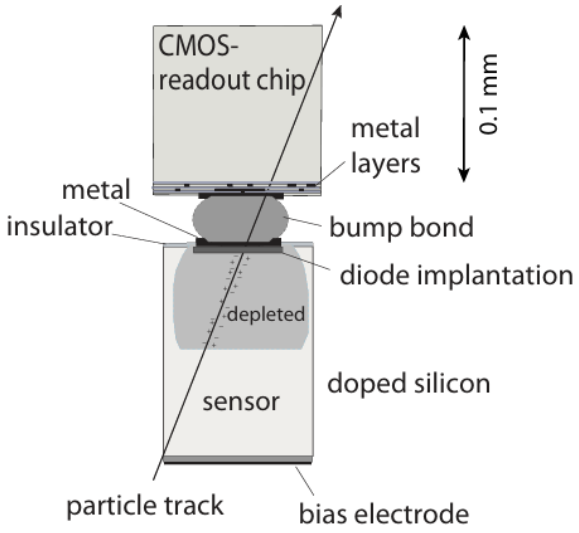

Figure 3.6: Cross section of a hybrid pixel sensor.

the readout chip containing electronic circuitry is typically implemented in conventional CMOS technology on low resistivity doped silicon substrate. However, the bump bonding process is a costly procedure with a significant rate of failures; furthermore, the use of two silicon layers, together with the bonding, increases the material budget which cannot be easily reduced.

Thanks to the individual optimization, this kind of pixel sensors can be extremely radiation hard (NIEL fluences up to 1×10^{16} 1-MeV-n_{eq}/cm^2, TID up to 1 Grad) and is the technology of choice for high radiation environments, such as the inner layers of ATLAS and CMS [17, 18].

3.4 Monolithic pixel detectors

To reduce the material budget of the hybrid detectors and to improve reliability, monolithic sensors have been developed, for instance by employing commercial CMOS processes with an epitaxial layer that can be used as active charge collection element. One of the first detectors of this kind was the MIMOSA26 sensor [19], in which a low resistivity substrate was employed and only a small depletion region could be achieved. For this reason the detectors partially relied on diffusion for charge collection, which increased the collection times to $\mathcal{O}(\mu s)$ and reduced the radiation resistance. However, the spatial resolution was significantly improved.

The monolithic approach has some variants, of which one is presented in the following (DEPFET sensors) and one in Section 4.1 (MAPS).

3.4.1 DEPFET

Depleted p-channel field effect transistors (DEPFET) pixel detectors use a particular type of monolithic pixels, in which each pixel is a single transistor. The structure is shown in Figure 3.7.

In these sensors, the substrate is depleted from the backside p^+ contact and the various p^+ regions near the transistor element (drain, source and clear) towards the n^- substrate. The external potential makes the produced electrons drift towards the top and the holes towards the backside.

The transistor is a p-channel MOSFET that produces a hole current from source to drain controlled by the potential on the external gate. In addition to the MOSFET standard structure, a deep n^+ implant is located some micrometers below the channel, becoming the most positive point in the pixel and a local minimum for the electrons that are therefore collected there.

The electron collection changes the floating potential, making this implant an internal gate electrode that controls the drain-source current with the collected charge.

The collected charge is then removed by applying a positive voltage to the clear contact, which is shielded with a p region, to avoid competition in the collection of electrons.

The DEPFET matrix is readout sequentially, which makes the detectors using this technology quite slow. An example is the Belle II PXD, which has an integration time of 20 µs. However, these detectors can be thinned down to ≈ 50 µm, thus significantly reducing the material budget, thanks to their extremely small noise.

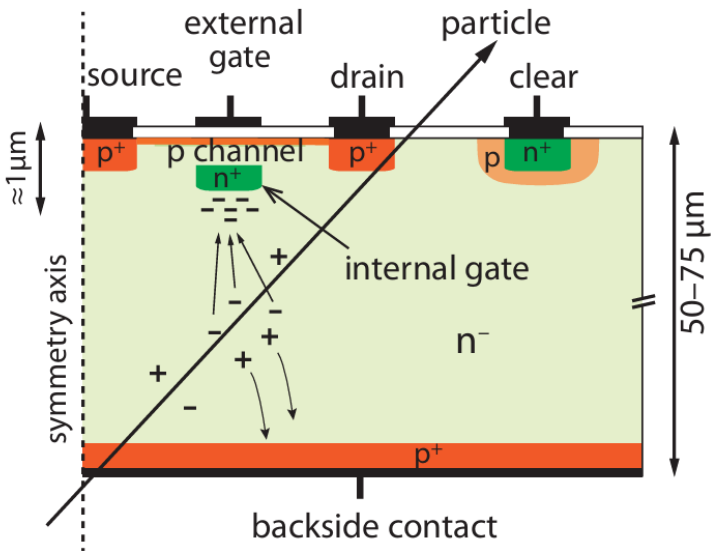

Figure 3.7: Cross section of a DEPFET pixel sensor. p^+, n^+ indicate heavily doped p and n implants, while n^- indicates the lightly doped n-type substrate.

3.5 Temperature effects

The dependence of the behaviour of a sensor on its operating temperature is a central topic in this thesis. For this reason, the effects (sometimes intertwined) of the temperature on the leakage current and the noise, two fundamental parameters of a silicon sensor, are presented.

Leakage current. A characteristic of a reverse biased detector is the leakage current I_L, which can have volume or surface contributions from different physical sources. For example, one of the contributing effects is the movement of minority charge carriers (electrons for the p and holes for the n regions) across the junction.

In general, however, the main contribution is given by thermal agitation, that can provide an electron in the valence band enough energy to jump to the conduction band, according to Maxwell-Boltzmann statistics, generating an electron-hole couple. Furthermore, radiation damage can create impurities in the bulk, thus additional intermediate levels that reduce the band gap and make it easier for electrons to jump to the conduction band. It should be noted that the leakage current depends critically on the density of impurities, that can create generation and recombination centers in the band gap.

The leakage current dependence on the temperature can be parametrized as:

$$I_\mathrm{L} \propto T^2 \exp\left(-\frac{E_a}{2kT}\right) \tag{3.4}$$

where E_a is the activation energy, with a fitted value of $E_a = 1.21$ eV.

Typical values of the leakage current density are of the order of $\mathrm{nA\,cm^{-2}}$.

The leakage current directly affects the noise (shot noise), through the Poissonian fluctuations of the number of collected charge carriers in the sensitive time of the amplifier. The input-referred noise charge (ENC, see Equation 5.1) is proportional to the square root of the current and of the preamplifier shaping time.

Thermal noise. At non-zero temperature the free charge carriers move due to their thermal kinetic energy without a preferred direction, in addition to the coherent motion due to an electric field. This is called thermal noise or Johnson-Nyquist noise and is present in all the conductors or semiconductors with a resistance R.

Thermal noise can keep its frequency independence up to high frequencies, almost behaving as a white noise. Its RMS noise voltage is given by:

$$V_{\text{rms}} = \sqrt{4kTR\Delta f} \tag{3.5}$$

where $k = 8.617 \times 10^{-5}$ eV K^{-1} is the Boltzmann constant, T is the temperature and Δf the bandwidth considered. As could be expected, a higher temperature implies more thermal agitation, therefore more thermal noise.

The effect on the ENC is different depending on how the resistor R is placed in the circuit (series or parallel). For the sensor bias resistor ENC $\propto 1/\sqrt{R}$, requiring large resistors, while for the series resistance along the signal path ENC $\propto \sqrt{R}$, requiring good conductivity.

3.6 Radiation Damage

Another significant parameter to take into account when developing a sensor is its resistance to radiation. In silicon devices there are two main mechanisms, that can be approximately related to the Non-Ionizing Energy Loss (NIEL) and the Total Ionizing Dose (TID).

It is important to note that the radiation damage range interesting for the VTX detector is a rather intermediate one, in which the effects of irradiation are significant but not extreme like in another experiments (i.e. ATLAS and CMS).

3.6.1 Bulk damage mechanism

Ionising energy losses generate electron-hole pairs in the bulk of the sensor but these do not contribute to silicon damage since they can drift and recombine without issues. Instead, bulk damage is caused by non-ionizing energy losses, which consist in the displacement of atoms from their position in the crystal lattice. These displacements create defects that introduce additional energy levels within the silicon band gap, altering the electrical properties of the sensor.

Depending on their position with respect to the valence and conduction energy bands, these new states can act as (see Figure 3.8):

- Donor or acceptor levels, which alter the effective doping concentration and, consequently, the depletion voltage.
- Trapping levels, which reduces the charge collection effciency.
- Generation and recombination centers, which affects the leakage current.

The threshold energy for displacement in silicon is ≈ 25 eV. Atoms can be displaced by massive particles via elastic scattering or by starting a nuclear reaction. Similarly, photons can displace atoms by generating recoil electrons or triggering a nuclear reaction. The displacement results in the formation of a *Frenkel pair*, consisting of two point defects: an interstitial (the atom displaced from its original position) and a vacancy (the empty lattice site it leaves behind).

When an atom receives a recoil energy higher than the threshold, it travels through the bulk losing energy both by ionization and by displacing other atoms. If the energy is suffciently high, the atom can displace multiple atoms in a localized region at the end of its path, producing a cluster defect.

Above $\approx$ 150 K, point defects are mobile and, if an interstitial and a vacancy meet, they can recombine, annihilating each other. This effect is called annealing, and reduces the radiation damage over time.

However, also the opposite effect (reverse annealing) has been observed at high temperature at longer time scales than those of the beneficial annealing. They are interpreted as a slow diffusion of defects that form complex structures that produce additional energy levels which contribute to the damage [20].

When the defect reaches an impurity or dopant atom, it interacts with it and changes the properties of the energy state, forrming a permanent defect, which is at the origin of radiation damage effects.

TID. The Total Ionizing Dose measures the total amount of energy deposited in the sensor through ionization. This kind of damage happens from the ionization of atomic electrons in the silicon oxide (SiO_2) on the top of the bulk and the interfaces (Si–SiO_2) and is generally referred to as surface damage.

In particular, the electron-hole pairs generated are separated by the electric field of the transistor due to the applied bias voltage, and the holes accumulate next to the Si–SiO_2 interface. Their presence there can create a charged layer that changes the characteristics of the transistors, in particular their threshold voltage.

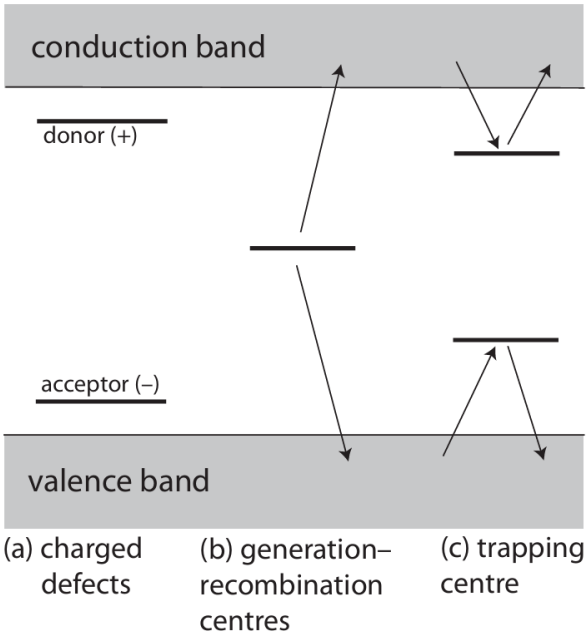

Figure 3.8: Typical localtions of energy levels of defects caused by radiation damage.

The circuitry, therefore, needs to take into account safety margins due to worsened operating conditions of the transistors at higher doses.

Furthermore, in devices such as silicon strips detectors, surface damage can lead to an increase in positive oxide charge, which in turn raises the interstrip capacitance. This is, for instance, the main source of noise on the APV25 preamplifiers. The interstrip capacitance scales with the ratio between the width of the strip and the pitch.

Another effect of surface damage is the increase of leakage current, in which point defects at the $Si-SiO_2$ interface can act as generation centers, contributing to the leakage current. However, this contribution is small if compared to the leakage current originating in the bulk.

NIEL. The maximum elastic recoil energy and the cross section of other available processes, both related to radiation damage, depend on the type and energy of the incoming radiation particle. A model provided by the non-ionizing energy loss (NIEL) hypothesis helps to compare effects of different radiation particles.

The fundamental assumption of this model is that any effect of displacement damage scales linearly with the recoil energy that produces the displacing collision. The displacement damage cross section ($D(E)$) provides the average recoil energy released by a particle of energy E per unit particle fluence, considering all possible interactions and the distribution of the energy lost to displacement. Figure 3.9 shows it for different particles.

The average recoil energy per particle fluence Φ can be obtained by integrating $D(E)$ over the spectrum (when known) of a radiation field. This result is usually normalized to the one obtained with 1 MeV monochrormatic neutrons ($D_n(1\,\mathrm{MeV}) = 95\,\mathrm{MeVmb}$), from which the hardness factor k and the equivalent 1-MeV neutron fluence $\Phi_{\mathrm{eq}} = k\Phi$ can be extracted, resulting in a useful tool to compare the effects of different radiation fields. Since these effects mainly affect the volume of the silicon, this kind of damage is referred to as bulk damage.

Part of the damage done according to this mechanism can be reverted thanks to annealing, which can be enhanced by increasing the temperature. It has been shown, however, that there is an optimal point for annealing, before the reverse annealing worsens the previous effects of the radiation damage.

In the following, some of the main effects of bulk damage are listed.

- *Increase of the leakage current.* The formation of additional accessible energy levels between the valence and the conduction bands favors the generation of thermal pairs, significally contributing to the leakage current of the sensor. Under the NIEL hypothesis, in silicon the increase can be modeled with:

$$I_{\mathrm{L}} = \alpha \phi_{\mathrm{eq}} V \tag{3.6}$$

  where α is the damage rate, that depends on the temperature and the annealing of the silicon, V is the volume of the sensor and ϕ_{eq} is the equivalent fluence of 1-MeV-$\mathrm{n_{eq}}/\mathrm{cm}^2$.

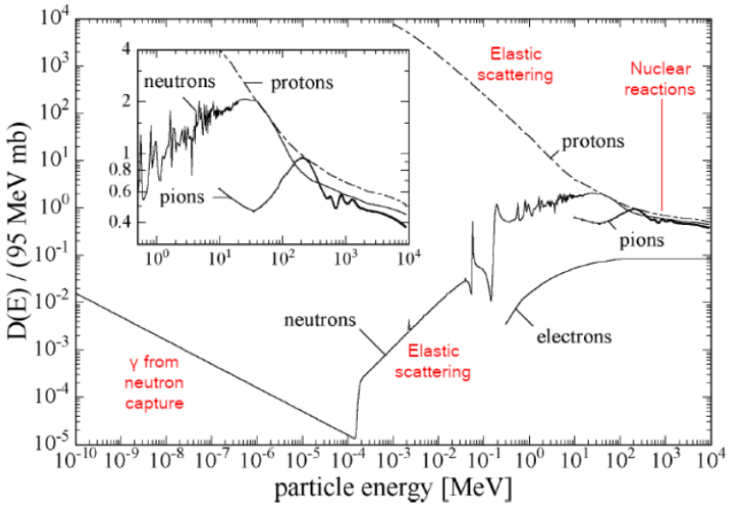

Figure 3.9: The displacement damage cross section for different particles, as a function of their kinetic energy. The main process responsible for displacement is indicated. Taken from [20, 21].

- *Recombination-generation centers.* The electrons and holes generated by charged particles via ionization, while drifting towards the collection electrode, can be captured by defects generated by bulk damage. These carriers, then, are only re-emitted after the integration time is finished, effectively only contributing to leakage.

- *Effective doping concentration and depletion voltage.* The bulk damage also modifies the effects of the dopant atoms, causing a change in the concetration of charge carriers in the silicon. The effective doping concentration N_{eff}, therefore, changes depending on the equivalent 1 MeV neutron fluence Φ_{eq}.

  Due to annealing, the analytical description of the effective doping concentration is rather complex, depending not only on the equivalent neutron fluence but also on the temperature of the sensor and how long that temperature was kept. However, a qualitative description of the effect is possible, with a decrease of the n-type concentration at increasing equivalent fluences Φ_{eq} until a minimum is reached at Φ_{eq} of $\mathcal{O}(10^{12}\,\text{cm}^{-2})$, where the so-called type inversion happens, and, at higher fluences, the effective doping concentration increases again. This dependence is shown in Figure 3.10, also showing the dependence of the depletion depth on the equivalent fluence.

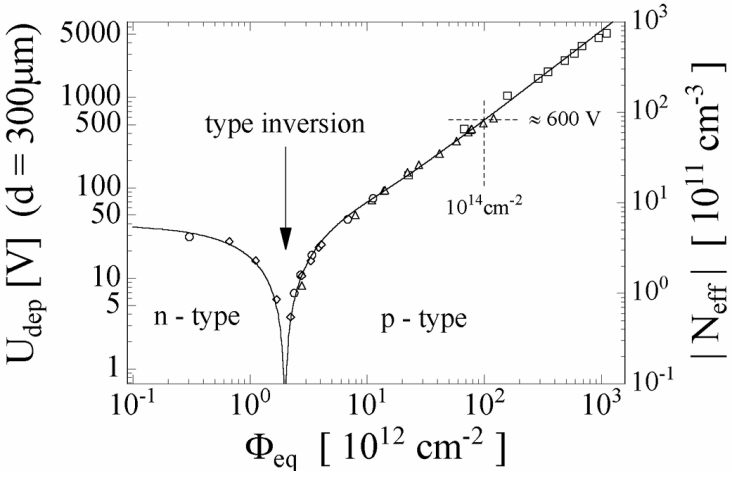

Figure 3.10: The dependence of the depletion voltage U_{dep} and the effective doping concentration N_{eff} on the equivalent neutron fluence Φ_{eq}. Taken from [20].

Chapter 4

CMOS MAPS sensors

Complementary Metal-Oxide-Semiconductor (CMOS) technology is the most widely used process for manufacturing integrated circuits. It combines p-type and n-type MOSFETs in a complementary arrangement, enabling efficient logic design with low static power consumption. The principle advantage of CMOS lies in the fact that current flows only during switching, which significantly reduces power dissipation compared to earlier technologies such as NMOS or bipolar logic.

The basic structure of CMOS transistors is shown in Figure 4.1.

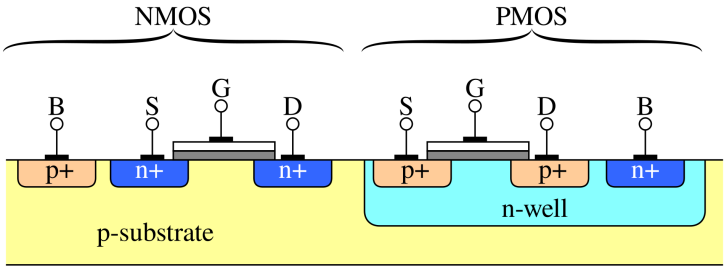

Figure 4.1: Schematic cross section.

CMOS devices are highly scalable, allowing continous miniaturization according to Moore's law, and are capable of integrating billions of transistors on a single chip. This has made them the backbone of digital electronics, powering processors, memory devices, and application-specific integrated circuits. Over time, CMOS has also expanded into analog and mixed-signal applications, including sensors and communication circuits.

As discussed in Chapter 3.4, in particle physics experiments, CMOS technology has found applications in vertex detectors, where custom monolithic active pixel sensors (MAPS) provide fine granularity, low material budget, and radiation tolerance.

Monolithic Active Pixel Sensors (MAPS) for charged particles are derived from the development of CMOS cameras, that today are employed everywhere, from mobile phones, surveillance devices and professional camera equipment. The challenges for charged particle detectors are that the released charge is much smaller than for visible and for most application a much faster readout is required.

In this chapter, after a general presentation of CMOS MAPS sensors, the TJ-Monopix2 and OBELIX devices, relevant for the VTX Upgrade Project, are discussed in detail.

4.1 CMOS Monolithic Active Pixel Sensors

The first realization of a monolithic pixel detector, in which the electronics was implemented on top of the epitaxial silicon, was proposed and realized in the first half of the 1990s [22]. The next step was to implement the full CMOS logic into these detectors, developing the Monolithic Active Pixel Sensors.

The charge is usually collected by a n-type electrode, while the CMOS logic inside the active pixel area is implemented using NMOS and PMOS transistors. To avoid conflicts in charge collection, additional p- and n-wells are added to shield the electronics from the sensitive region. In particular, in the example in Figure 4.2, an additional deep p-well is added below the n-well to shield it from becoming a competing collection node.

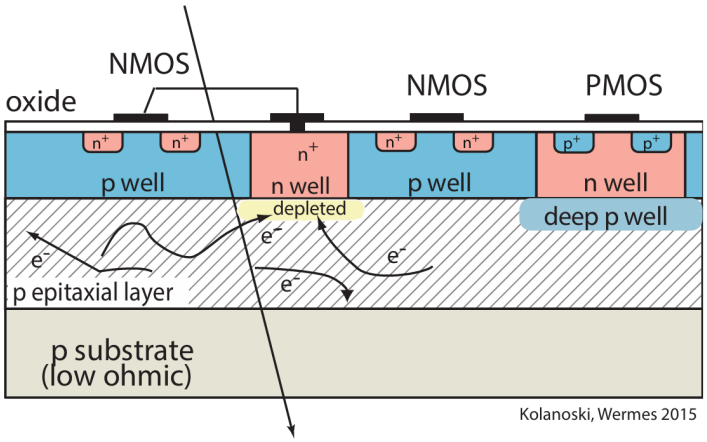

Figure 4.2: Cross-section of a MAPS, with the collection mechanism and the CMOS logic shown.

In the first detectors of this kind, the depletion region was limited to a small volume around the collection electrode, thus the charge collection mainly exploited the diffusion of the deposited charge. The substantial contribute of the charge diffusion to the signal implies long collection times (~ 100 ns), with a reduced collected charge due to trapping effects and the absence of a directional drift field outside the small depletion region.

While this is not an issue when these detectors are used for light detection (e.g. CMOS cameras), due to the large amount of photons that homogenously collide within each pixel cell, it becomes particularly relevant when this technology is applied to High Energy Physics experiments. The reduced thickness allows only for a small deposited charge ($\sim 2000\, e^-$), therefore a further reduction makes it even more difficult to detect traversing particles.

Although the reduced collected charge and the slow readout do not allow for the operation in high-rate environments such as trackers for ATLAS or CMS, the small material budget ($50 - 100$ µm of thickness) makes them good candidates for other applications, such as the vertex detector of the STAR experiment, which uses the MIMOSA design, developed by IPHC in Strasbourg [23]. In particular, the sensors used in the STAR experiment (called ULTIMATE) are made with a higher resistivity silicon (400 $\Omega\,$cm) with respect to the standard MIMOSA sensors (10 $\Omega\,$cm), thus increasing the depletion depth from a fraction of a µm to several µm.

More recently, the ALICE collaboration has chosen MAPS pixels for the upgrade of the Inner Tracking System, developing the ALPIDE sensor, based on the TowerJazz [24] 180 nm CMOS process. To increase the depletion depth, these sensors exploit a high silicon resistivity (> 1 k$\Omega\,$cm), using low bias voltages (< 10 V) to create a depletion thickness of several tens of µm [25].

4.1.1 Depleted MAPS

Fast and complete charge collection is required in high rate and high radiation environments. The depletion region must be increased as much as possible, providing a larger and faster signal. For this reason, the Depleted MAPS detectors have been implemented, in which an enlarged depletion region is obtained operating the moderately high-resistivity sensor in the reverse-bias regime.

The depletion depth d of a sensor is given by the:

$$d = 0.53\,\mu\text{m}\sqrt{\rho\,[\Omega\,\text{cm}]V\,[\text{V}]} \tag{4.1}$$

where V is the bias voltage and ρ the resistivity. Their optimization allows to reach a depletion depth in the range $d = 25 - 150$ µm, with a collection time < 20 ns.

The low bias voltage is also essential to be able to maintain the depleted region thickness in spite of the changes in effective dopant concentration caused by radiation damage, as discussed in Section 3.6.

A substantial difference in the design of a DMAPS is given by the dimensions of its collection electrode, which affects the charge collection efficiency and uniformity, the preamplifier input capacitance as well as the detrimental effects of charge injection into the sensor caused by the CMOS transistor switching.

Large collection electrode In Figure 4.3, the cross section of a MAPS with a large collection electrode is shown. In this design, a deep n-well is at the same time a collection electrode and a shield for the CMOS electronics. The

depletion region can be produced from the top side only or also including a rear contact with a backside processing, which allows the creation of a depleted region between the two sides.

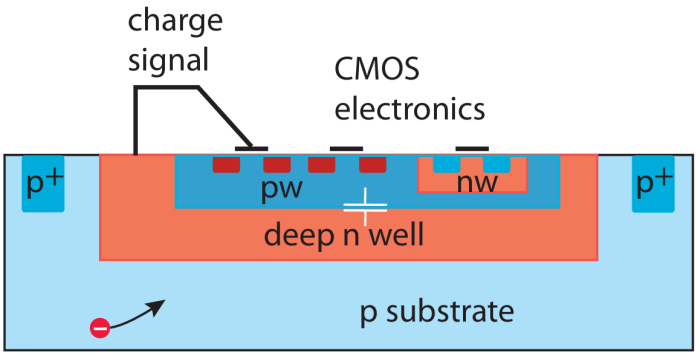

Figure 4.3: Cross-section of a MAPS with a large collection electrode.

One of the main advantages of this design is the small average drift distance of charges to reach the collection electrode, thus reducing the trapping probability and increasing the radiation resistance. However, one of the disadvantages is given by the large detector capacitance at the amplifier input.

The large detector capacitance C_{D} scales with the dimension of the electrode, reaching up to 400 fF, thus decreasing the voltage amplitude at the amplifier input according to:

$$dV = \frac{dQ}{C_D} \tag{4.2}$$

and increasing the input referred amplifier noise (ENC), which scales with the detector capacitance [26].

Small collection electrode The alternative design has a small charge collecting electrode separated from the CMOS electronics, as shown in Figure 4.4. This variant has a collection node capacitance as low as $C_{\mathrm{D}} \simeq 5 - 20$ fF, which results in a larger signal at the input of the preamplifier, according to Equation 4.2. However, it is harder to achieve high radiation resistance due to the longer average drift paths (thus higher trapping probability) and the non uniform electric field in the bulk, which is stronger near the collection electrode and weaker in the pixel corners.

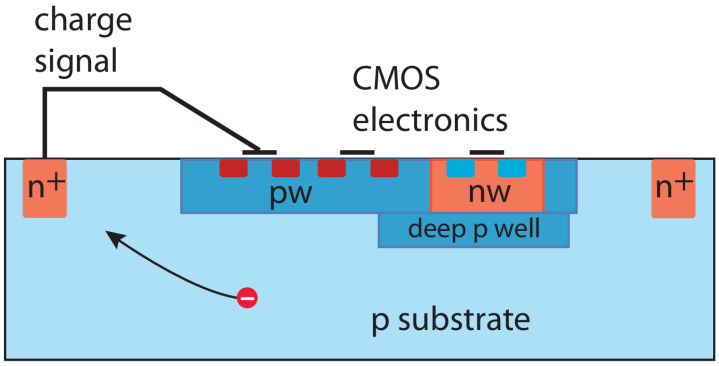

Figure 4.4: Cross-section of a MAPS with a small collection electrode.

These detectors are typically operated applying a bias to the deep p-well and the backside of the chip, which is usually limited by the maximum voltage that the CMOS transistors of the p-well can sustain. Furthermore, the difference between the two bias voltages (the one applied to the deep p-well and the one applied to the backside of the chip) can not usually exceed 1 V, to avoid punch-through. In this way, however, the depletion region that can be reached by this design is further limited, thus reducing the charge collection effectiveness and the range of the possible uses of this design. Improved depletion and charge collection, however, can be achieved with modifications of the doping profile.

4.1.2 Process modifications

The TowerJazz 180 nm CMOS imaging process, employed in the ALPIDE sensor, is not sufficient to achieve full depletion of the active volume, which results in lower signal amplitude and slower charge collection ($\sim$ µs) after irradiation with fluences higher than 10^{12}-10^{13} 1-MeV-n_{eq}/cm^2. To improve the radiation resistance to fluences $>$ 10^{15} 1-MeV-n_{eq}/cm^2, several iterations of process modification have been carried out.

Additional n-type layer. As can be seen from Figure 4.5a, the depletion in the standard process starts at the junction of the collection electrode at the center, without fully depleting the sides of the pixel. To achieve full depletion, an electric field gradient configuration similar to a planar junction is required.

This is achieved by adding a low dose continous n-type layer above the epitaxial layer (Figure 4.5b), which creates a depletion region that starts from the two p-n junctions (formed by the n-layer with the p-wells and the p-epi layer) and extends to the entire pixel. The collection field is directed towards the collection electrode, strengthening the lateral collection of charges. To fully deplete the area around the collection electrode, a reverse bias ≤ 6 V has to be provided.

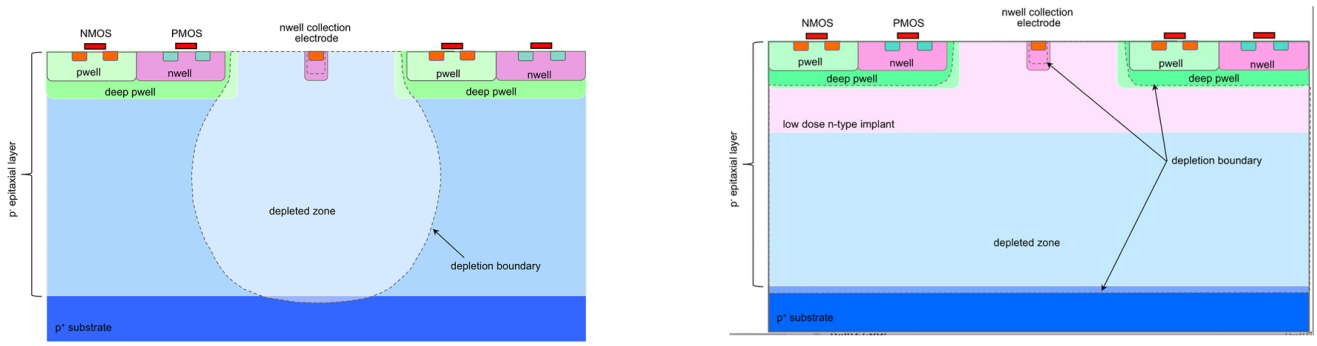

(a) Standard process

(b) Addition of n-type layer

Figure 4.5: Cross-section of the sensor in the standard process (a) and after the addition of a n-type layer (b).

The tests on the prototypes (i.e. TJ-Monopix1) with this first modification showed an increased radiation resistance, but still a significant reduced collection efficiency in the pixel corners was observed after irradiation up to fluences of 10^{15} 1-MeV-n_{eq}/cm^2, with average detection efficiency decreasing from 97% to 70% [27, 28].

As can be seen in Figure 4.6a, the electric field has a minimum in the pixel corners below the p-well, highlighted by the star symbol. The charges produced on the sides are pushed by the collection field into this region with low drift field, increasing the trapping probability.

A second modification of the process to mitigate this behaviour introduced a gap in the sides of the n-type layer, thus increasing the lateral field component near the pixel corners. As shown in Figure 4.6b, in this design the minimum of the electric field is deeper in the volume, bending the field lines toward the collection electrode, thus reducing the drift path length. The tests on the detectors produced with this modification (TJ-Monopix1 and TJ-Malta1) showed an efficiency of 85% after irradiation with 10^{15} 1-MeV-n_{eq}/cm^2 [29].

4.2 TJ-Monopix2 sensor

The iteration of the process optimization for the TowerJazz 180 nm CMOS process continued with the design and production of the TJ-Monopix2 sensor. This new sensor, designed for the development process of the ATLAS ITk, has been designed using four different geometries, given by the implementation of two approaches in two different silicon substrates. In particular, the process modifications are the n-gap design, already described in the previous section, and the additional p-well, in which a p-type implant is added below the deep p-well, altering the electric field in a similar way to the n-gap design method. The two possible substrates are a 30 µm thick epitaxial silicon on a low-resistivity substrate or highly resistive Czochralski silicon, which can reach up to 100 µm of thickness, increasing the maximum depletion depth achievable.

This sensor has a reduced noise and threshold dispersion with respect to its predecessor TJ-Monopix1, with the possibility to operate the sensor with lower threshold ($\sim 200\,e^-$) and improve detection efficiency after irradiation. Notably, the threshold dispersion across the matrix can also be controlled with a threshold tuning circuit.

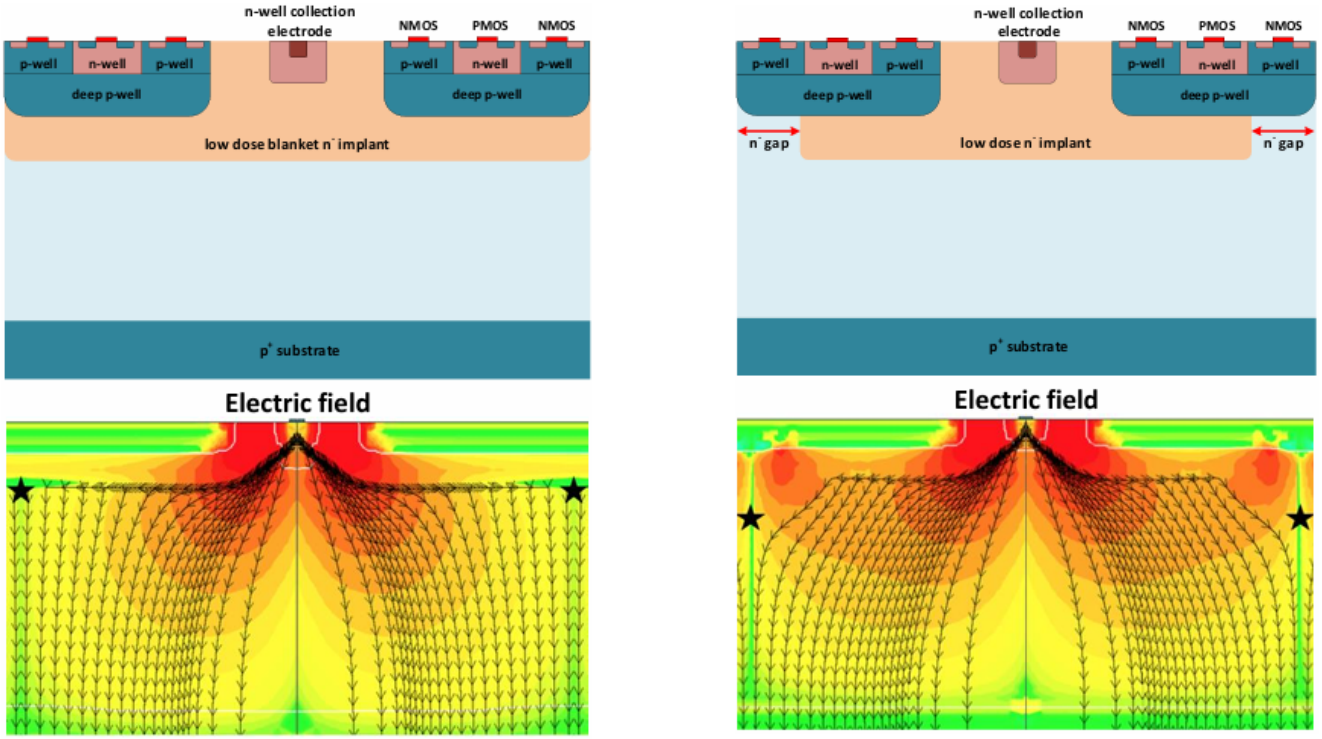

(a) Addition of n-type layer

(b) Gaps on sides of n-type layer

Figure 4.6: Comparison of the lateral field for the modified process (a) and the modified process with the additional gaps on the sides of the n-layer (b). TCAD simulations in the second row taken from [30].

This sensor has been chosen as the prototype for OBELIX, the new pixel sensor of the upgrade of the Belle II vertex detector, which will be produced with the same process modification.

4.2.1 Matrix and flavors

The pixel matrix (shown in Figure 4.7) is made of 512×512 square pixels with a 33.04 mm pitch, for an active area of $\simeq 286$ mm^2. The matrix is divided in four submatrices (*flavors*), each with different variations of the front-end amplifier and the biasing scheme. All the pixels are designed with the reduced deep p-well geometry described in Section 4.1.2.

The biasing scheme differs for the coupling of the collection electrode, which can be either DC or AC depending on pixel flavor. In particular, the signal is coupled directly to the front-end electronics in the DC and via a capacitor in the AC.

In the flavors with DC coupling, the n-type collecting electrode is directly connected to the input of the amplifier (Figure 4.7), with maximum bias set to 1.8 V, as defined by the technology node, so the sensor bias can be applied via a negative potential on the substrate (PSUB) and deep p-well (PWELL). In literature these flavors are also referred to as Normal front-ends.

The maximal reverse bias voltage applicable to the p-wells is limited by the CMOS circuitry to -6 V [31]. Before irradiation the potential on PSUB and PWELL must be equal to avoid the punch-through effect: while the deep low-dose implant isolates the p-wells from the backside substrate and allows for a higher reverse bias on the substrate, the n-gap modification, instead, weakens this isolation, resulting in a high current flow between the p-wells and the backside substrate (punch-through) [30].

After irradiation, due to the change in the effective doping of the epitaxial p-layer, the PSUB potential can be increased before reaching the punch-through, achieving a larger depletion zone and improving the collection in the angles of the pixel.

In the flavors with AC coupling (called HV in this thesis), instead, a positive voltage is directly applied to the collection electrode, since this is decoupled from the input of the preamplifier. This design allows the application of relatively high voltages (above 40 V even before irradiation), then potentially enhancing the charge collection

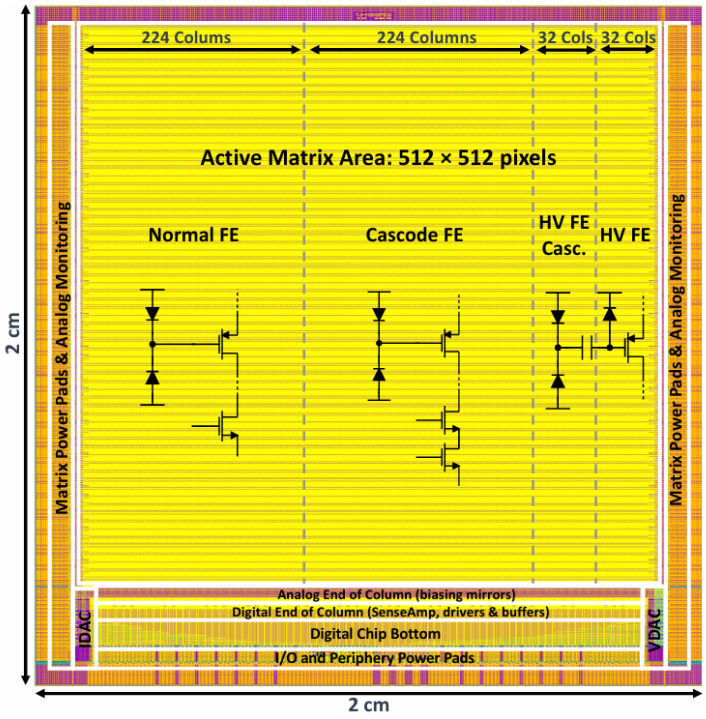

Figure 4.7: Matrix of the TJ-Monopix2 sensor with the different front-ends.

capability. However, with AC coupling, due to the capacitive voltage divider formed by the coupling capacitor and the combined gate and stray capacitances, only about 40% of the signal voltage generated by the collected charge is transferred to the amplifier input, as shown in Figure 4.8b. As a reference, also the DC preamplifier input circuit is shown (Figure 4.8a). The operation point of the HV front-end has then to be optimized to compensate this effect.

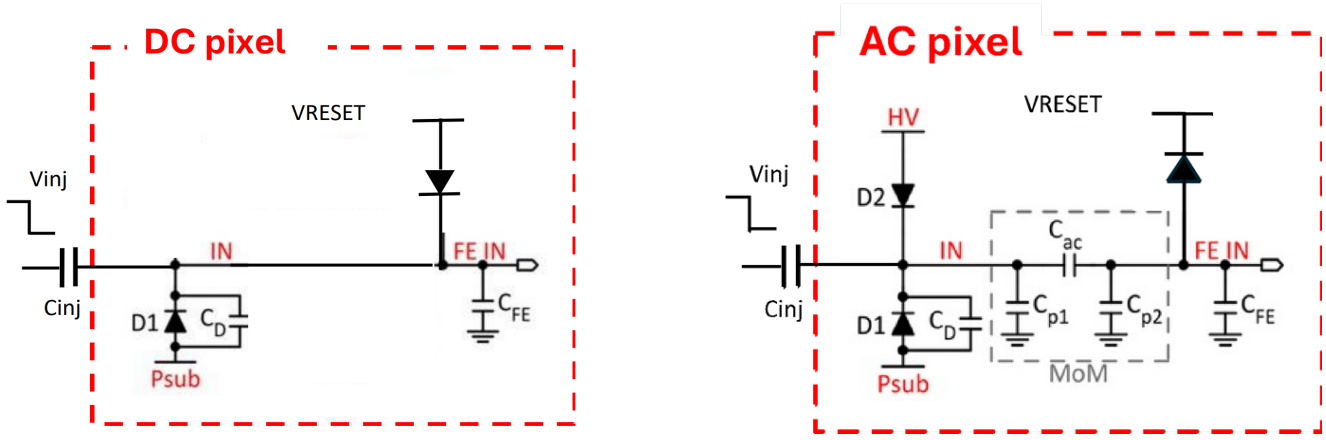

(a) DC pixel

(b) AC pixel

Figure 4.8: Preamplifier input circuits of the pixels in the DC and HV flavors.

Both types of front-end are also implemented with a variant in which an additional cascoded transistor is added to reach a higher gain. These flavors are called DCC and HVC. The comparison of the performance of the DC and AC coupled sensors after irradiation and at high temperature ($20 - 40$ °C) was one of the main goals of the characterization in lab and with beams of this thesis.

As shown in Figure 4.7, the DC and DCC front-ends cover 224 columns each, while the HV and HVC front-ends only 32 each.

4.2.2 Input circuit

Each pixel contains an analog amplifier and discriminator to convert the charge signal into a digital pulse, schematically shown in Figure 4.9.

The charge signal is converted in a voltage signal through a small capacitance (C_D = 3 fF), then it goes to a pre-amplifier and then to a discriminator, providing a digital output signal when the input is above the set threshold. The small detector capacitance allows the use of a voltage amplifier instead of the more common charge sensitive amplifiers with a small feedback capacitor used in standard electronics. The length of the output signal is the Time Over Threshold (TOT), which also provides information about the signal charge. The pre-amplifier and the discriminator working conditions are defined by several chip registers. The collected data are finally sent to the chip periphery in order to transmit and store them outside the chip.

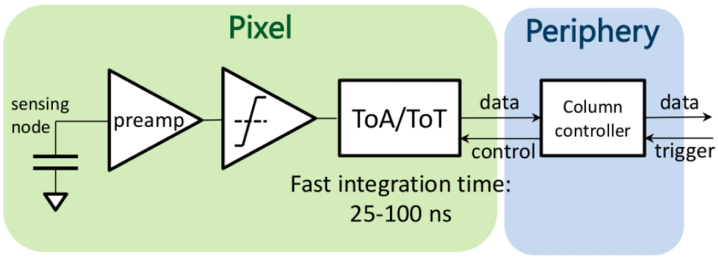

Figure 4.9: Schematics of the voltage amplification and readout steps.

The circuit is shown in detail in Figure 4.10. The operating point of the amplifier is controlled by several voltages and currents, generated in the periphery by a group of 8 bit Digital-to-Analog Converters (DACs). The DAC-groups are repeated 16 times along the chip periphery and supply 32 columns each. While the currents are distributed as voltages, they form half of a current mirror in the periphery and the other half in the amplifier.

A dedicated circuit can be employed to fine-tune the threshold of each individual pixel according to the value of a 3-bit DAC, called TDAC (see also Section 5.2).

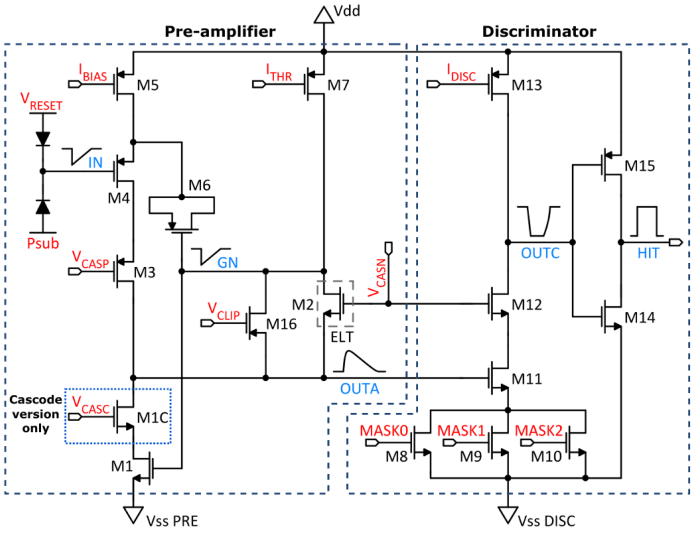

Figure 4.10: Schematics of the TJ-Monopix2 circuit with the improvements from the TJ-Monopix1 sensor. The cascode variant with the M1C transistor to improve the gain is also shown.

List of parameters. The various DACs are controlled by a set of parameters, whose values are set during the sensor's configuration.

The V_{RESET} is a potential directly applied via a diode to the amplifier input and is used to modify the input baseline, compensating for sensor leakage.

The amplifier is composed of three stages, each with individual bias currents. The first stage is supplied with the I_{BIAS} parameter, which controls the gain and, therefore, the threshold and the threshold dispersion. The second stage is controlled by the I_{THR}, which acts on the feedback strenght and speed of the amplifier, also changing the gain and thus threshold, and the third by the combination of I_{DB} and I_{TUNE}. The latter stage, in particular, controls the in-pixel tuning, described in Section 5.2. The V_{CASC} voltage is applied to the cascoded transistor (in the front-ends in which it is present) and, together with V_{CASP}, changes the operating point of the first stage of the amplifier.

I_{CASN} mainly controls the baseline of the output of the preamplifier and is set by a dedicated circuit. I_{CASN} allows to reach a wide range of thresholds of the front-end only by changing the baseline voltage, without changing other working conditions of the circuit.

An important part of the hit signal is given by the timing information from the sampling of a 7-bit timestamp called BCID, which is distributed from a gray encoded 40 MHz counter. The BCID is distributed to each pixels, but the propagation delay along the columns of the chip requires a compensation, with a circuit dedicated to the delay of the hit signal depending on the position of the pixel. This delay can also be globally set with the I_{DEL} parameter.

The timing information is also important for the calculation of the Time over Threshold (ToT), which depends on the collected charge. A maximum value for the ToT can be set with the V_{CLIP} parameter, resulting in a similar ToT for all the signals above a certain value. If set to 255 no clipping is performed.

Furthermore, when I_{THR} is decreased, the time that the analog output takes to get back to the baseline increases, thus increasing the maximum ToT value.

Finally, I_{COMP} sets the bias current for the comparator for the bit-lines of the data bus in the perifery, while I_{RAM} the driving strength of the bit-lines in the pixel [13].

4.2.3 Digital circuit

At the output of the analog circuit is the HIT signal, which gives the digital information of the hit for each pixel. From this signal also the information on the collected charge can be extracted, using the measurement of the ToT. This technique, shown in Figure 4.11, exploits the sampling of the BCID at the start and at the end of the signal. In particular, when the analog signal value goes over the threshold the Leading Edge (LE) is sampled, while the Trailing Edge (TE) is sampled when the signal returns below it. The ToT value is thus calculated from their difference in 25 ns units.

The values of LE and TE are kept in a Random Memory Access (RAM) implemented in the in-pixel circuitry together with a Read-Only Memory (ROM) to store the pixel address and the control logic.

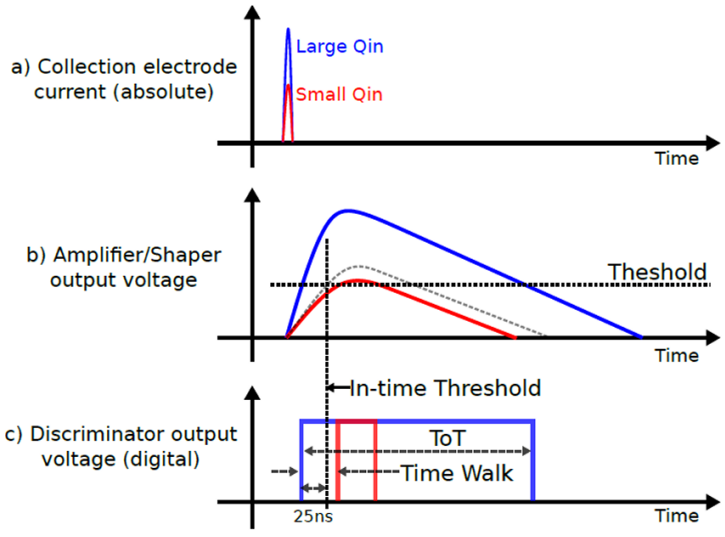

Figure 4.11: Time-over-Threshold technique.

The column-drain readout architecture. The readout of the pixel is column-based, with all the pixels of a double column sharing a common column-bus, which can be accessed by one pixel at a time. The column bus

includes the BCID timestamp, the data (LE, TE, address) and the control signals.

The columns are read out by the End Of Column (EoC) block, which also transmits the signals, while the Digital Chip Bottom (DCB) processes the hit information. The overall scheme of TJ-Monopix2 is shown in Figure 4.12.

The readout uses a column-drain architecture, in which each pixel with a non-zero signal is readout using a token signal. This allows to individually readout the pixels in a controlled order, while also speeding up the process by processing only the pixels with a signal. The hit pixels remain frozen until they are readout due to the absence of a local buffer.

In particular, two token signals are implemented: a fast one, that defines the higher level priority among the groups of 2×2 cores and propagates across the double column, and a local one, which defines the priority within the group. When the readout controller receives the information from the token, the matrix is frozen by asserting the FREEZE signal. The READ signal is then raised and data (TE, LE, pixel address information) are transmitted to the periphery through the column data-bus.

The discriminator output (the Hit signal) is also connected through a chain of OR gates to the bottom of each column to an output pad of the chip, which makes it available externally. This signal is called HitOr, it is the fastest available response to a particle hit and can be used as a trigger for measurements. The output signal is provided as logical OR of all pixels and it is asynchronous, preserving any timing information from the pixel.

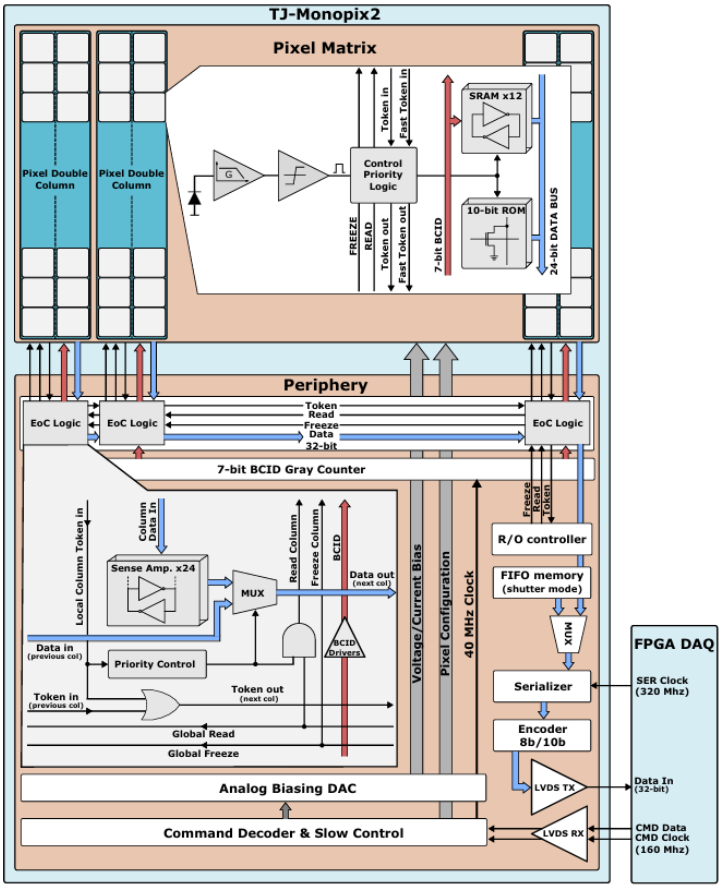

Figure 4.12: Overall scheme of TJ-Monopix2.

4.2.4 In-pixel injection circuit

TJ-Monopix2 is equipped with features for characterization and debugging purposes. The principal one is the in-pixel charge injection circuit that mimics charge collection by the sensor by the artificial injection of charge at the input of the amplifier. This circuit is schematically shown in Figure 4.13.

With an injection pulse V_{inj} sent to the injection capacitance C_{inj}, a signal charge Q_{inj} accumulates on C_{inj} and mimics the same signal charge on the detector capacitance C_{D}. C_{inj} has to be way smaller than the detector

capacitance C_D, which is connected in series, to maximize the charge at the input node. The design value is 230 aF, with typical detector $C_D \sim 3$ fF.

A dedicated register (PulseStartCnfg) delays the time of injection with respect to the 40 MHz BCID counter reset with a precision of 3.125 ns. Other registers set the 8-bit DACs that generate the necessary currents and voltages, for example the injection voltage, which can be set in discrete DAC units from 0 to 140. At higher DAC values the buffers of the DACs that control the injection are not linear anymore, preventing quantitative measurements at higher voltages.

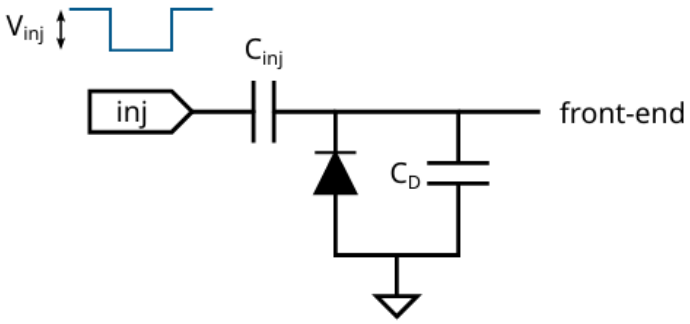

Figure 4.13: Injection circuit in TJ-Monopix2.

Furthermore, the matrix contains eight pixels whose analog signal can be accessed through the PCB, of which four are located in the top left, and four in the top right corner of the matrix.

4.3 OBELIX sensor

A DMAPS chip is being developed specifically for the Belle II VTX Upgrade. This sensor is called OBELIX (Optimized BELle II pIXel sensor) and it is currently in the final design stage before its first submission. The matrix design (i.e. the amplifier and the ToT analog information, the column-drain readout and the in-pixel tuning) is inherited from TJ-Monopix2, while the digital periphery and the powering scheme have been reworked and new features added. Both sensors are fabricated in the modified TowerJazz 180 nm CMOS process.

Comparing to its predecessor, the size of the matrix has been adjusted to fit into the VTX geometry. It is composed by 896×464 square pixels with the same 33.04 µm pitch of the TJ-Monopix2 sensor, for a total active area of 29.60×15.33 mm^2, almost 454 µm^2. The physical dimension of the OBELIX chip is 30.17×19.36 mm^2

In the original design, in the first submission the matrix was equally divided between the DCC and HVC flavors already described for TJ-Monopix2, while in the second submission only one front-end would be implemented. Recently (September 2025), however, the VTX Upgrade Collaboration has decided to only implement the DCC flavor, due to its significantly better performance after irradiation with 5×10^{14} 1-MeV-n_{eq}/cm^2, shown by the test beam results in Section 6.3.1. The original floorplan is shown in Figure 4.14, while the comparison between the initial specifications, TJ-Monopix2 and the current OBELIX specifications is shown in Table 4.1. The specifications from the detector, in particular the ones linked to the timing properties, required the development of a dedicated sensor.

The request of a low material budget in each VTX layer brings to the choice to thin the sensor up to 40 µm.

One of the main changes with respect to TJ-Monopix2 is the implementation of a triggered readout, to cope with the high hit rate foreseen at Belle II keeping the readout bandwidth reasonable. For this reason the trigger latency has been set between 3 and 12 µs, with a configurable value.

Since Single Event Upset (SEU) is a significant concern for future detector operation, an important feature of the chip is to ensure that the control system is able to reset the sensor registers to default operational values very often (10 Hz).

The room temperature cooling system foreseen for VTX limits the chip power to no more than 200 and 300 mW cm^{-2}, which has required halving of the BCID frequency, from 40 MHz to 21.2 MHz, also reducing the BCID timestamping precision to slightly less than 50 ns.

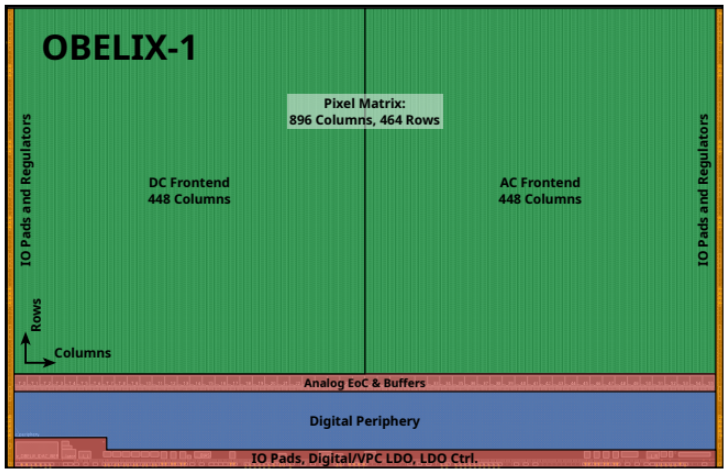

Figure 4.14: Matrix of the first submission of the OBELIX chip (OBELIX-1).

	Initial Specification	OBELIX	TJ-Monopix2
Pixel pitch	< 40 µm	33.04 µm	33.04 µm
Sensitive layer thickness	< 50 µm	30 µm	30 and 100 µm
Sensor thickness	< 100 µm	> 40 µm	-
Hit rate capability in the matrix	> 600 MHz cm^{-2}	> 600 MHz cm^{-2}	> 600 MHz cm^{-2}
Hit rate capability at the sensor output	> 120 MHz cm^{-2}	120 MHz cm^{-2}	1 MHz cm^{-2}
Trigger latency	> 10 µs	3 to 12 µs	-
Trigger rate	30 kHz	> 100 kHz	-
Overall integration time	< 100 ns	47.1 ns	-
Time resolution	< 50 ns	3 ns in oVTX	-
Total ionizing dose tolerance	100 Mrad	100 Mrad	-
NIEL fluence tolerance	5×10^{14} n$_{eq}$/cm^2	5×10^{14} n$_{eq}$/cm^2	5×10^{14} n$_{eq}$/cm^2
SEU tolerance	flash configuration (min^{-1})	up to 10 Hz	-
Matrix dimensions	$\sim 30 \times 16$ mm^2	29.60×15.33 mm^2	19×19 mm^2
Overall sensor dimensions	$\sim 30 \times 19$ mm^2	30.17×19.36 mm^2	20×19 mm^2
Powering	through voltage regulators	on chip LDOs	-
Outputs	one at < 200 MHz	one at 339 MHz	one at 160 MHz
Max. operating temperature	room temperature	< 40 °C	< 40 °C

Table 4.1: OBELIX sensor specifications (initial and current) compared to TJ-Monopix2.

4.3.1 New OBELIX digital periphery

A significant upgrade from the TJ-Monopix2 chip is the triggered readout, with the addition of the Trigger Unit (TRU) [13]. In OBELIX, the readout of each double column is carried on independently by an End of Column controller (EoC), which increases the readout bandwidth for the pixel matrix.

The TRU is composed of 112 Trigger Groups (TRGs), each processing 4 double columns, and is in charge of selecting the fired pixel information from the matrix which are in-time with the triggers sent by the Belle II system. For this purpose, each TRG employs two stages of memory (Figure 4.15): the first stage has to store the pixel information during the trigger delay; the second memory has to compare the BCID of the fired pixel with each trigger time information buffered in a dedicated global memory. When they have a match, the pixel data is transferred to the Transmission Unit (TXU), which then sends the data to the backend system (Leading Edge and Trailing Edge BCID, column and row, trigger ID).

Inside each TRG there is another module, called Peripheral Time to Digital converter (PTD), that is used to compensate the almost halved BCID timestamping frequency with respect to TJ-Monopix2, improving the time resolution of the sensor, in particular for the outer layers of VTX, up to $3 - 4$ ns. This module uses an auxiliary feature of TJ-Monopix2, the HitOr signals (see [13]), which allow for a fast arrival of the hit information, without

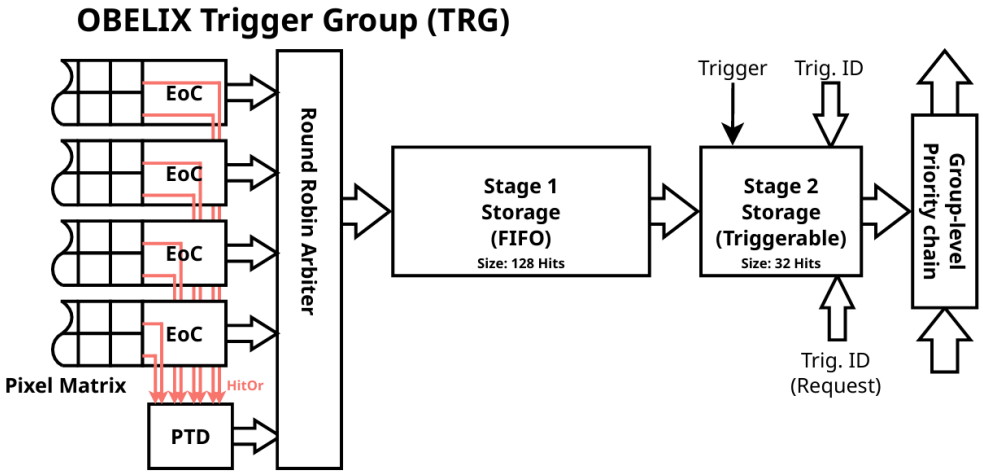

Figure 4.15: Scheme of the two stages of memory of a single trigger group.

waiting for the ToT measurement. Together with the signal, also the BCID is sampled, which allows the offline reconstruction of the event.

This feature will only be activated in the outer layers of VTX because it significally increases the power consumption and the cooling option chosen for the inner layers could not be able to compensate also this temperature increase.

Another feature of OBELIX related to the trigger is the Track Trigger Transmission module (TTT), which allows to contribute to the Belle II trigger. In particular, the expected reduction of the performance of the inner layers of the CDC requires a contribution from the VTX to it. To implement this possibility, at least the outer layers of VTX (given their lower occupancy due to the reduced hit rate) will be integrated in the trigger of the detector.

Therefore, OBELIX has been developed with the ability to generate information to be used for a fast track reconstruction at trigger time. The TTT module divides the matrix in 8 logic regions (called macropixels) and generates a one-byte word depending on the region firing. The macropixels can also be grouped together, creating larger regions, extending even over multiple chips. This fast signal is then sent to the Belle II trigger system, for a first rough estimation of the track. If the track is succesfully reconstructed, then, the Belle II trigger signal is distributed across the full matrix.

4.3.2 Timeline

The first submission of the OBELIX chip is expected between the end of the 2025 and the beginning of 2026. The sensor should be ready for testing at the end of summer 2026. The following steps are the characterization of the sensor before irradiation, the irradiation campaign and the characterization after irradiation. An improved version of the sensor is scheduled to be available for testing in 2028, in order to complete its characterization before assembling the VTX detector.

Chapter 5

TJ Monopix 2 characterization - Laboratory

In this chapter the tests conducted in laboratory on irradiated and non-irradiated TJ-Monopix2 sensors are presented, summarizing the sensor characterization process and describing its properties after irradiation.

In particular, the tests and their results from the final part of this process are shown, which were conducted during a crucial phase of the VTX upgrade project, in which the designs of both the detector and the OBELIX chip needed clear indications from measurements on several aspects.

The importance of this study for the OBELIX development is clear, as it explores some of the flaws of the sensor's prototype and suggests potential mitigation strategies. Moreover, it establishes testing procedures that can be also used in the future characterization effort of the new sensor. Furthermore, it gives clear indications on the operating limits that can be reached by the sensor, directing the designers towards solutions that can accomodate them.

The TowerJazz 180 nm process, modified with respect to the one used in ALPIDE, has already shown good radiation resistence in other sensors, such as TJ-Monopix1 and TJ-Malta1 [27, 32], for an equivalent fluence of 1×10^{15} 1-MeV-n_{eq}/cm^2. However, these measurements have been conducted at low temperature. The VTX requirement of operating at room temperature, to reduce material and system complexity, makes the effect of the increase of leakage current due to radiation damage critical, which degrades the sensor's performance.

In particular, in previous Test Beams on a TJ-Monopix2 sample irradiated with 5×10^{14} 1-MeV-n_{eq}/cm^2 at room temperature ($\sim 30 - 35$ °C) efficiency drops at increasing threshold have been observed, which motivated an additional investigation on the origin of this performance variation at different temperature and fluence.

Although the most important results for the designs are related to the efficiency measurements from the operation with beams, presented in Chapter 6, the tests in the laboratory have been of critical importance to prepare the sensors for the operation at the Test Beam. Additionally, the tests in the laboratory have also focused on understanding the clock signal cross-talk effect and its consequences on the operation of the sensor.

The tests have been conducted on a wide range of temperatures, from 10 to 50 °C, but the most important for the VTX design are the ones near 30 °C, which has been given by the simulations as the lowest limit for the detector's operation.

These measurements have been crucial in the definition of the temperature specifications of the sensor and the VTX detector but also in the choice of the DCC front-end for the OBELIX sensor.

5.1 Tested sensors

For this work one non-irradiated and four irradiated TJ-Monopix2 chips have been tested. Three of them have been irradiated with 24 MeV protons to a NIEL equivalent fluences of 1×10^{14}, 2.5×10^{14} and 5×10^{14} 1-MeV-n_{eq}/cm^2 at the Cyrcé Cyclotron in Strasbourg, France, while one has been irradiated with 90 MeV electrons to a NIEL equivalent fluence of 5×10^{14} 1-MeV-n_{eq}/cm^2 at the Tohoku University in Sendai, Japan.

The choice of these fluences for the irradiation with protons was driven by the will to test the evolution of the effects of radiation damage on operation in the expected fluence range, while the choice of the irradiation with electrons was to understand the actual effect of electrons on these chips, since they compose the majority of the Belle II background.

During the tests after the irradiation campaign, the HVC front-end of the chip irradiated with a 2.5×10^{14} 1-MeV-n_{eq}/cm^2 fluence became non-functional, thus no measurements on this front-end are available at this fluence.

The non-irradiated and the proton-irradiated chips were tested in Pisa and at DESY during the test beam campaign, while the electron-irradiated chip was characterized at KEK and DESY.

In Table 5.1 the tested chips are listed together with their irradiation features.

Chip	Particle	Fluence [1-MeV-n_{eq}/cm^2]	Working FE
W8R13	//	//	DCC & HVC
W8R4	p	1×10^{14}	DCC & HVC
W2R17	p	2×10^{14}	DCC
W8R6	p	5×10^{14}	DCC & HVC
W2R5	e	5×10^{14}	DCC & HVC

Table 5.1: Chips' characteristics.

5.2 Threshold and noise

As discussed in Sec 4.2, TJ-Monopix2 has a digital readout, generating a hit when the input signal exceeds a programmable threshold.

The average value of the total charge of a signal produced by a minimum ionizing particle (mip) in the 30 µm of MAPS sensitive thickness is around 3200 e^- (assuming 107 e^-/ µm), while the most probable value (MPV) is only about 2300 e^- (assuming 77 e^-/µm) [16]. Such low signals, even reduced due to radiation damage (see Section 3.6), require a careful optimization of the sensor's operating threshold at the operating point, since it has to balance the need to retain high detection efficiency compatible with a stable operation of the sensor. Two important figures of merit determine the minimum operating threshold: the noise and the threshold dispersion across the matrix.

Noise and equivalent noise charge. Many electronic effects concur to create time-varying voltage fluctuations at the pre-amplifier output, which are collectively referred to as noise. The Root Mean Square (RMS) of the voltage fluctuations is called noise output voltage. To quantify it, a quantity called *equivalent noise charge* (ENC) is defined, which corresponds to the input signal in units of electrons that creates a signal as large as the observed noise at the output of the amplifier:

$$\mathrm{ENC} = \frac{\text{noise output voltage}\,[\mathrm{V}]}{\text{gain}\,[\mathrm{V}/e^-]} \tag{5.1}$$

Thus the signal-to-noise ratio S/N is given by [33]:

$$\frac{S}{N} = \frac{Q}{q\mathrm{ENC}} \tag{5.2}$$

where Q is the input charge, q is the charge of an electron and ENC is the equivalent noise charge of the input.

Operating threshold and threshold dispersion. The global detection threshold of the sensor has to be set to a value as low as possible in order to maximize the detection efficiency. However, it can not be set to a too low value, to keep the hits from noise fluctuations at an acceptable level. A compromise must be found between these two requirements.

In addition to noise, the choice of the operating threshold is affected by the threshold dispersion across the matrix, originating by differences in the parameters of the integrated components. The main elements that contribute to threshold dispersion are the quiescent voltage at the output of the pre-amplifier and the discriminator voltage offset.

The threshold and its dispersion are also usually quantified reporting the corresponding charge, in electrons, at the input of the channel that gives an output signal corresponding to the threshold voltage and its dispersion [34]:

$$\mathrm{THR}(e^-) = \frac{\text{voltage threshold}\,[\mathrm{V}]}{\text{gain}\,[\mathrm{V}/e^-]} \tag{5.3}$$

$$\sigma_{\mathrm{thr}}(e^-) = \frac{(\text{threshold dispersion})_{\mathrm{RMS}}\,[\mathrm{V}]}{\text{gain}\,[\mathrm{V}/e^-]} \tag{5.4}$$

In order to avoid too many noise hits, the operating threshold lower limit is usually chosen to be at least 5 or 6 times higher than the combined threshold dispersion and noise standard deviation:

$$\mathrm{THR} = (5-6) * \sqrt{\mathrm{ENC}^2 + \sigma_{\mathrm{thr}}^2} \tag{5.5}$$

A typical value of the threshold of non-irradiated sensors is $\sim 220\,e^-$, while the threshold dispersion of a non-irradiated sensor is 1.5-2 times higher than the noise (i.e. for the W14R12: $\sigma_{\mathrm{thr}} = 12\ e^-$ and ENC $= 7\ e^-$). Instead, typical values of the threshold dispersion of an irradiated sensor are about 1.5-2 times lower than the noise (i.e. for the sensor irradiated at 5×10^{14} 1-MeV-$\mathrm{n_{eq}/cm^2}$ at 30 °C: $\sigma_{\mathrm{thr}} = 15\ e^-$ and ENC $= 26\ e^-$). Therefore, fine tuning the threshold locally on a per-pixel basis can reduce the threshold dispersion, effectively reducing the minimum value of the operating threshold. This possibility has been implemented in the TJ-Monopix2 sensor with a dedicated circuit.

After tuning, the dispersion of the threshold is inversely proportional to the number of bits of the tuning DAC (TDAC) n_{DAC}:

$$\sigma_{\mathrm{thr,tuned}} = \frac{\sigma_{\mathrm{thr}}}{2^{n_{\mathrm{DAC}}}} \tag{5.6}$$

The global threshold of the chip, as defined in Equation 5.3, is determined both by the pre-amplifier's operating point and the discriminator's voltage threshold, that can be adjusted acting on several registers of the chip that define the voltage and the current supplied to the front-end (see also Section 4.2.2).

To measure the threshold and noise of the whole matrix, the response of each pixel has been characterized by internal charge injection, using the injection circuit included in TJ-Monopix2 and shown in Section 4.2.4, which produces artificial hits on each pixel through an injection capacitance C_{inj} connected to the collection electrode (more details also in Section 5.3).

S-Curve method The response of each pixel is measured injecting a variable charge N_{inj} times (typically $N_{\mathrm{inj}} = 100$) and recording the number of hits above threshold N_{hits}. For each value of the input signal the occupancy is given by the fraction of events where the pixel has registered a hit and it has the typical S-curve shape shown in Figure 5.1.

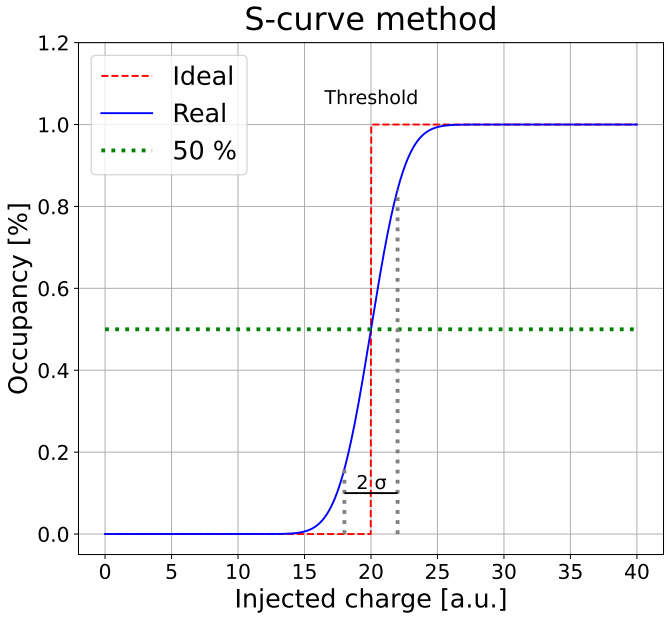

Figure 5.1: Ideal and real response of the front-end to charge injection. The threshold is defined as the charge at which the percentage of hits crosses 50%. The width of the function compared to an ideal step function can be used to determine the noise of the front-end

The ideal result without noise is a step function, with $N_{\mathrm{hits}} = 0$ for injected charges below the value of the threshold and $N_{\mathrm{hits}} = N_{\mathrm{inj}}$ for injected charges above this value. Due to noise fluctuations, however, (especially

after irradiation) the occupancy curve of the pixels shows a smearing, resulting in the S-curve shape. The threshold of the pixel is defined as the injected signal that gives 50% occupancy, while the noise influences the slope of the S-curve.

Since the noise fluctuations are assumed Normally distributed, the S-curve can be fitted with a sigmoid function given by the cumulative distribution function of the Normal distribution:

$$N_{\text{hit}}(Q) = \frac{N_{\text{inj}}}{2}\left[1 + \text{erf}\left(\frac{Q - Q_{\text{thr}}}{\sqrt{2}\sigma}\right)\right] \tag{5.7}$$

where erf is the Gauss error function, Q is the injected signal, Q_{thr} and σ are the threshold and the noise of the pixel, respectively. When reporting the operating threshold of a sensor (or, more precisely, of a front-end), the $1\,\sigma$ width of the threshold distribution of the sensor's pixels is usually quoted as the threshold dispersion.

An example of the results of this measurement is provided in Figure 5.2a, where the S-curves of all the (enabled) pixels of the DCC matrix of a non-irradiated sensor are plotted, and in Figure 5.2b, where the distribution of the thresholds of these pixels is fitted with a gaussian to extract the average value, which is quoted as the matrix's threshold. In Figure 5.2c, finally, the noise distribution of the pixels is shown, together with the gaussian fit to extract the average value.

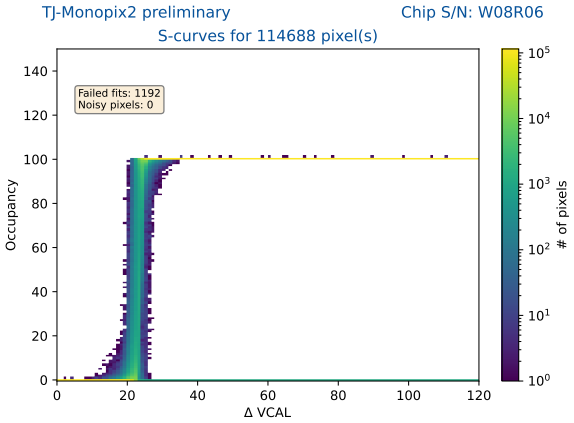

(a) S-curve

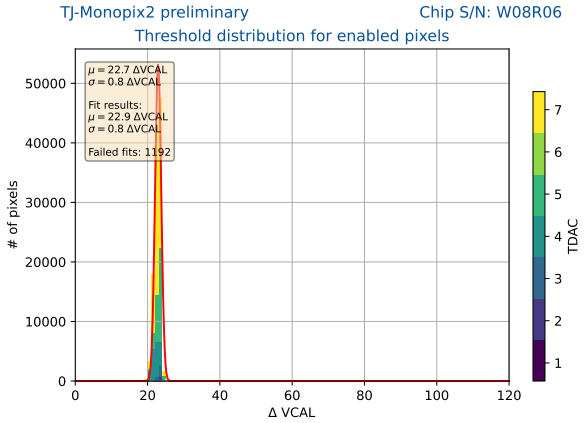

(b) Threshold distribution

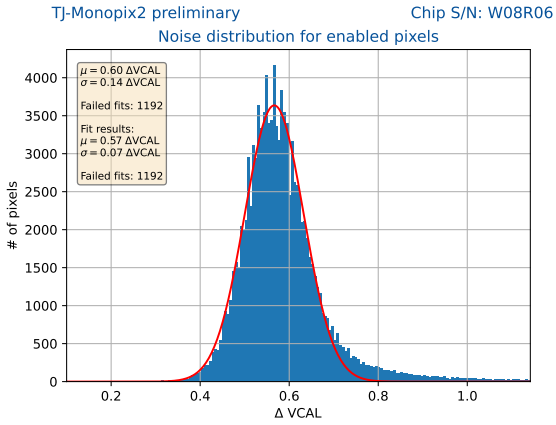

(c) Noise distribution

Figure 5.2: Threshold and noise measurement for the full DCC front-end of the W8R6 chip before irradiation. In these plots 1 DAC $= 9\,e^-$ (see Section 5.3).

This kind of measurement, also referred as *threshold scan*, is one of the main tools used in the characterization work presented in this thesis.

TDAC tuning As already mentioned, the threshold dispersion is a relevant factor to take in consideration when operating the sensor. The matrix threshold is set by global registers, but its dispersion can be large. To correct for this, an in-pixel threshold tuning mechanism is implemented.

Specifically, the analog part of the in-pixel front-end includes the 3-bit threshold tuning DAC (TDAC) circuit, shown in Figure 5.3a, which can be used to adjust the discriminator threshold of each pixel in order to uniformize the pixel threshold on the matrix, thus reducing the threshold dispersion. As can be seen in Figure 5.4, after tuning the threshold dispersion is reduced to one third of the original one, passing from 13 to 5 e^-. This is particularly important when operating the matrix with low threshold, especially after irradiation, when the charge collection efficiency is reduced due to radiation damage.

This circuit controls the discriminator active load current I_{DISC}, which is responsible for the setting of the pixel threshold. The circuit does not generate I_{DISC} but works as an analog multiplexer, which selects one of seven lines generated by the main 8-bit biasing DAC. This means that the value of this current is given by two contributes:

$$I_{\mathrm{DISC}} = I_{\mathrm{DB}} + (\mathrm{TDAC} - 1) I_{\mathrm{TUNE}}\,, \;\; 1 \leq \mathrm{TDAC} \leq 7 \tag{5.8}$$

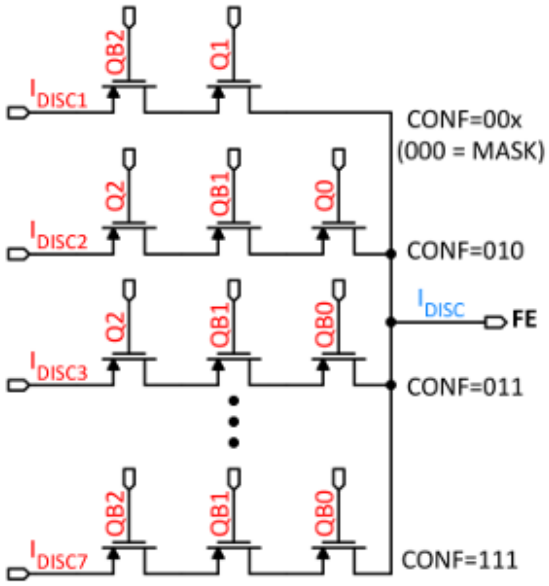

(a) Schematic of the 3-bit tuning DAC.

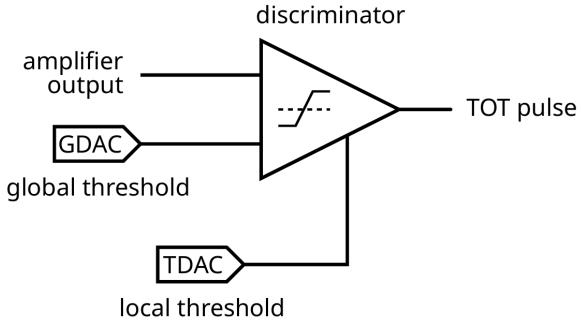

(b) Schematic of the in-pixel discriminator and threshold DACs.

Figure 5.3: Schematics of the circuits that set the threshold for the pixels.

Of the 8 available values of the TDAC, the values from 1 to 7 are used to tune the threshold, while the 0 is used to individually disable the pixels. The default value of TDAC is 4 and changing this parameter can significantly modify the threshold in a range of values as big as 40% (DCC) and 70% (HVC) of the default one. This design choice simplifies the in-pixel circuitry, since only a multiplexer instead of a DAC is required, while maintaining the flexibility of individually tuning the pixel threshold,

A crucial part of the preparation of the sensor for testing or operation is the tuning of the pixel threshold. This process requires to initially set the working point (gain and baseline) of the amplifier and the global discriminator voltage threshold (GDAC) to reach a given threshold in e^-, varying appropriately the chip parameters (see Section 4.2.2). After the global threshold value is set, a fine tuning of the single pixel discriminator value (TDAC) is done to reduce the threshold dispersion in the matrix.

The TDAC adjustment procedure, in particular, is carried on with a binary search procedure, with the goal of achieving a Gaussian distribution of TDAC centered around 4. The effectiveness of this tuning depends on the value of I_{TUNE}, whose choice is the compromise between a finer tuning (thus smaller I_{TUNE}) and a wide enough range of threshold values reached (thus bigger I_{TUNE}).

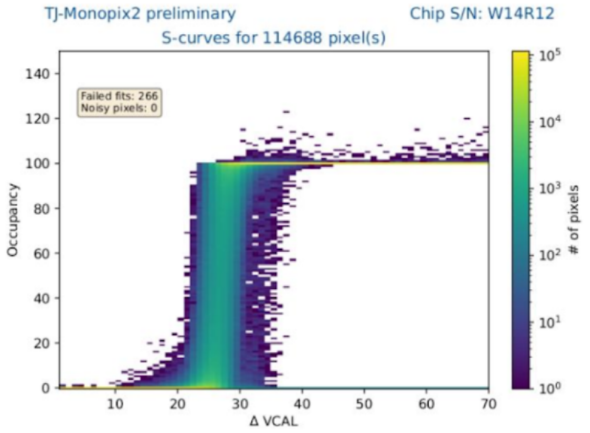

(a) S-curve before threshold tuning.

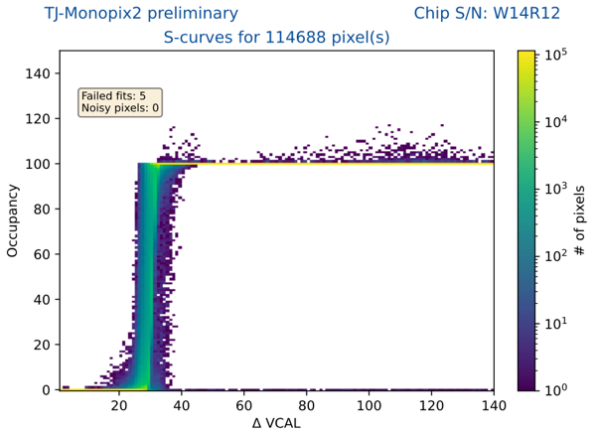

(b) S-curve after threshold tuning.

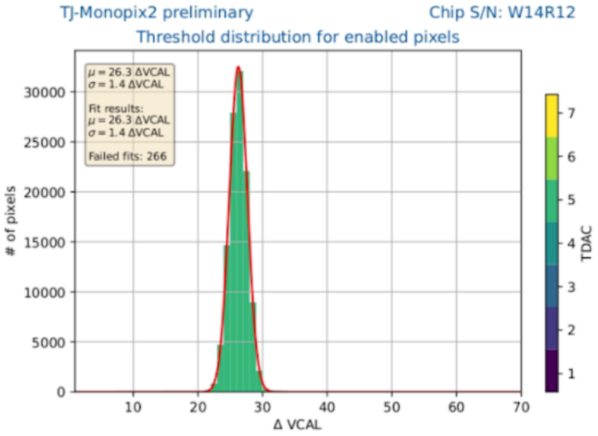

(c) Threshold distribution before threshold tuning.

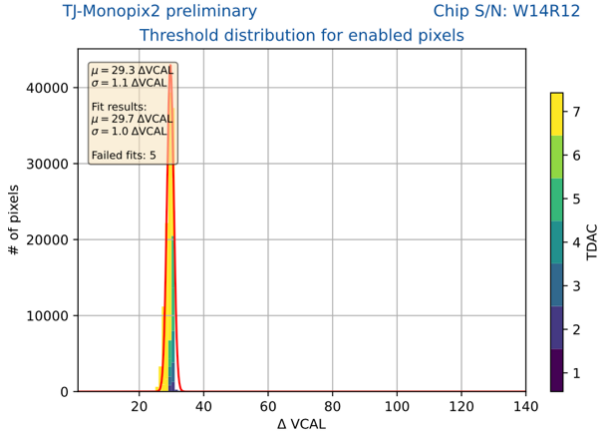

(d) Threshold distribution after threshold tuning.

Figure 5.4: S-curve and threshold distribution before (a, c) and after (b, d) threshold tuning for the non-irradiated chip. In these plots 1 DAC = 9 e^- (see Section 5.3).

5.3 Conversion factors and constants

A crucial element of the sensor is the Digital-to-Analog Converter (DAC), used for example to provide the required voltages to the registers that define the operating point of the front-end during configuration. The chosen DAC has 8 bits, with the Least Significant Bit (LSB) of LSB = 1.8 V/256 = 7.03 mV.

The voltage step used in the injection circuit is set in DAC, corresponding to the voltage step ΔV_{inj}, and the corresponding injected charge in e^- can be calculated with the conversion factor from DAC to e^- that corresponds to the value of injection capacitance C_{inj}. This is of particular importance since it is needed when quoting the threshold of the sensor, in order to properly understand its behaviour.

As already stated, a relevant part of this characterization was carried out using internal injection tests. The charge injected in these tests is proportional to the injection voltage pulse amplitude, according to $Q_{\text{inj}} = C_{\text{inj}} \cdot \Delta V_{\text{inj}}$, which is set by two registers (V_{L} and V_{H}, with $\Delta V_{\text{inj}} = V_{\text{H}} - V_{\text{L}}$), and the minimum injection step is given by the DAC LSB. The injected signal can go from 0 to 140 DAC units, without exploiting the full DAC range due to an unwanted saturation in the injection circuit.

The injected signal is then expressed in DAC units and can be converted to electrons using the value of the injection capacitance C_{inj}. Its design value for all the front-ends is $C_{\text{inj}} = 230$ aF [34], corresponding to a conversion factor K of 10.1 e^-/DAC, as shown in Equation 5.9.

$$K = C_{\text{inj}} \cdot LSB = \frac{230\,\text{aF}}{q_{e^-}} \cdot 7.03 \frac{\text{mV}}{\text{DAC}} = 1.4375 \frac{e^-}{\text{mV}} \cdot 7.03 \frac{\text{mV}}{\text{DAC}} \approx 10.1 \frac{e^-}{\text{DAC}} \tag{5.9}$$

However, the absolute calibration of the conversion factor, performed with a ^{55}Fe source, has shown that the actual value of C_{inj} is significantly different in the two front-ends.

The calibration of this conversion factor, thus the measurement of the injection capacitance, was performed before the start of this work using radioactive sources. The calibration consists in the measurement of the Time-Over-Threshold response of each pixel to a known signal, like the emission peaks of radioactive sources, and then comparing the results with the response from the internal injection. The procedure is shown in Figure 5.5.

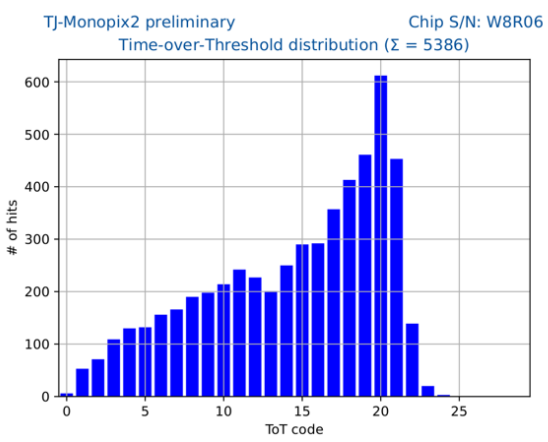

(a) ToT of the ^{55}Fe.

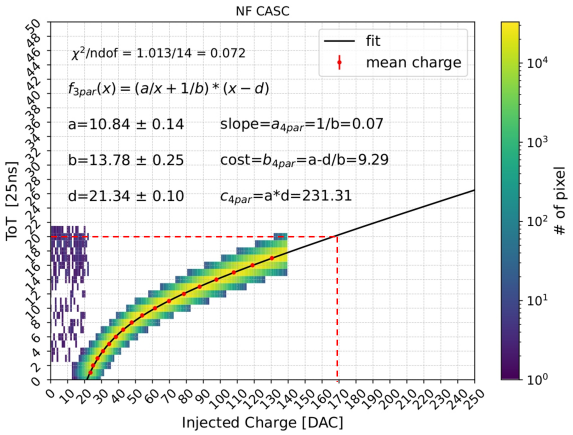

(b) ToT of the internal injection.

Figure 5.5: ToT of the ^{55}Fe source (a) and ToT of the internal injected signal with extrapolations for the calibration (b) before irradiation for the DCC front-end. The fit is performed with Equation 5.10 in the range highlighted by the green region.

This measurement has been conducted exploiting the 5.9 keV peak of the ^{55}Fe source, which corresponds to roughly 1616 e^- deposited when taking into account the energy of 3.65 eV needed for the production of an electron-hole couple in silicon. The charge of 1616 e^- can not be reached by the internal injection of the chip, so the corresponding ToT is extrapolated from the data. This extrapolation is possible because that value is in a range of linear response of ToT with respect to Q_{inj}.

To extract the ToT, in particular, its dependence on the injected charge Q_{inj} is fitted with an empirical function:

$$\text{TOT}(Q_{\text{inj}}) = \left(\frac{a}{Q_{\text{inj}}} + b^{-1}\right) \cdot \left(Q_{\text{inj}} - d\right) \tag{5.10}$$

which well describes its evolution for charge values higher than the threshold.

The results shown in Figure 5.5 for the DCC matrix give a ToT peak of the ^{55}Fe = 20 DAC, that corresponds to an injected charge of 170 DAC from the calibration curve. This results in a measured conversion factor: $K = 1616\,e^-/170\,\text{DAC} = 9.5\,e^-/\text{DAC}$.

The results obtained from measurements on several chips and used as conversion factors in this work are:

$$K_{\text{DCC}} = 9\,\text{e}^-/\text{DAC} \text{ and } K_{\text{HVC}} = 18\,\text{e}^-/\text{DAC} \tag{5.11}$$

While the DC front-ends show good agreement with the design value (Equation 5.9), the large discrepancy measured in the AC coupled front-ends has been investigated by the designers and confirmed to be due to the significant contribution of parasitic capacitance to the injection capacitance C_{inj}.

The values in Equation 5.11 have been used to convert the information of the injected charge from DAC unit to electrons unit in all the measurements in which an e^- result is quoted.

5.4 Effects of bulk irradiation on sensor's operation

An essential part of this study is to understand how irradiation affects sensor operation. While the main bulk damage mechanisms have already been discussed in Section 3.6, the present section focuses on their implications for the characterization and operation of irradiated sensors. The discussion is restricted to bulk damage, as surface damage has only a minor impact on sensor performance. This has also been confirmed by previous measurements

on a sensor irradiated up to 100 Mrad, which did not show an increase in the leakage current (main cause of the effects shown in this section) and showed only a slight increase of the noise up to $20\,e^-$, which has only limited effects on the operation of the sensors.

Bias voltage. As already described in Section 4.2.1, the reverse biasing of the sensor can be done with three potentials: the PWELL, the PSUB and the HV.

When biasing the DCC flavor, the PWELL and PSUB are employed and, before irradiation, they must be kept equal, to avoid punch-through. Furthermore, the maximum reverse bias voltage that can be applied on the p-well is limited by the CMOS circuitry to -6 V. After irradiation, the bulk damage changes the doping concentration, thus a higher voltage is needed to fully deplete the bulk and reach high detection efficiency. This higher voltage is supplied only to the p-substrate, allowing for a larger depletion zone, in particular in the corners of the pixel.

In the HVC flavor, instead, the biasing is usually provided only with the HV, which allows for a higher voltage also in the non-irradiated sensors. The main difference after irradiation is that, due to the change in doping concentration, a higher voltage is needed to reach full depletion and therefore high detection efficiency.

Leakage Current. One of the main effects of irradiation bulk damage in silicon sensors is the increase of the leakage current (see Section 3.6). This increase affects many features of the sensors, such as threshold, noise and Time over Threshold, as can be seen from Figure 5.6. Its variation with temperature makes it crucial to properly monitor and control the operating temperature.

Threshold. The creation of trapping defects due to bulk damage reduces the collected charge and requires to operate the sensor with lower threshold to preserve good detection efficiency. On the contrary, after irradiation it was observed that with the same operating settings the threshold increases as shown in Figure 5.6, where an increase from 20 to 40 DAC ($\sim$ 200 to $\sim$ 400 e^-) was observed at room temperature for a sensor irradiated at 5×10^{14} 1-MeV-n_{eq}/cm^2.

In TJ-Monopix2, the threshold increase after bulk damage is related to the increase of leakage current from the following mechanism: the discharge of the collecting electrode via the bias diode shown in Figure 5.7b is determined by a time constant RC, where R is the reset diode small signal resistance inversely proportional to the sensor leakage current [29]; high leakage current will discharge the collecting electrode in a timescale comparable to the amplifier signal processing time.

In this way, the amplitude of the output signal is significantly reduced, thus increasing the amount of deposited charge necessary for the recording of the hit (i.e. threshold increase). The discharge of the electrode also significantly reduces the Time over Threshold value of the signal, as shown in Figures 5.6c and 5.6d, where the slope of the ToT is significantly reduced.

The effect of the discharge of the collecting electrode is shown in Figure 5.8, where it is measured accessing the analog monitoring pixels available in the matrix for debugging purpose.

In these figures the input signal (yellow), connected to the collecting electrode, and the signal output of the preamplifier (pink) signals of the preamplifier are shown for an irradiated chip with two different temperatures and leakage currents. The first falling edge is the relevant one for the measurements, corresponding to the start of the charge collection on the collection electrode. The signal of a non-irradiated sensor is a step function, while for an irradiated one the leakage current discharges the electrode, thus altering its shape.

In particular, in these figures the 140 DAC signal injected in the pixel has a bigger amplitude and lasts longer in the configuration with lower temperature and leakage current (Figure 5.8a).

The second signal that appears in the two figures, while also due to the discharge, is a spurious effect due to the rising edge of the injected voltage step and not relevant for this analysis.

Since the leakage current strongly increases with temperature, the threshold shows the same dependence (as can be seen from Figure 5.9).

Noise. The increased shot noise, due to the increased leakage current, is one of the main consequences of radiation damage, which makes it more difficult to operate the sensor at low thresholds.

The increased noise can be immediately seen when comparing the S-curves of a non-irradiated sensor (Figure 5.6a) with the S-curves of an irradiated one (Figure 5.6b), which shows a significant decrease in the slope of the S-curve, symptom of a higher noise (cfr. Figure 5.1). This is also shown by the noise distribution before (Figure 5.6e) and after irradiation (Figure 5.6f), which shows a significant increase of the average value of the noise.

The dependence of the leakage current (and consequently of threshold and noise) on the operating temperature has important consquences for testing and operation:

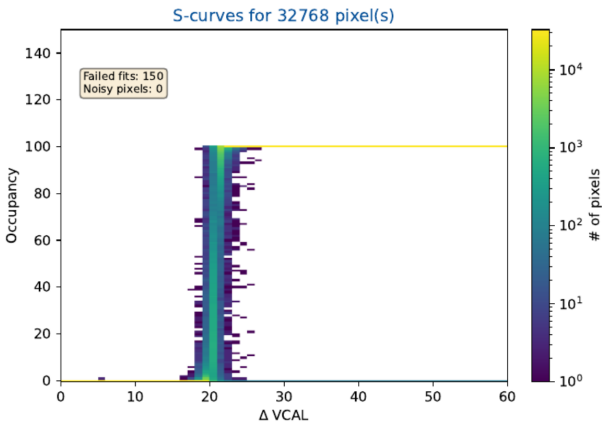

(a) S-curve before irradiation.

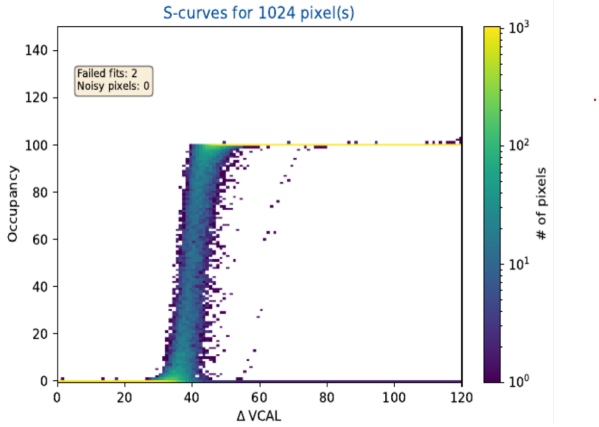

(b) S-curve after irradiation.

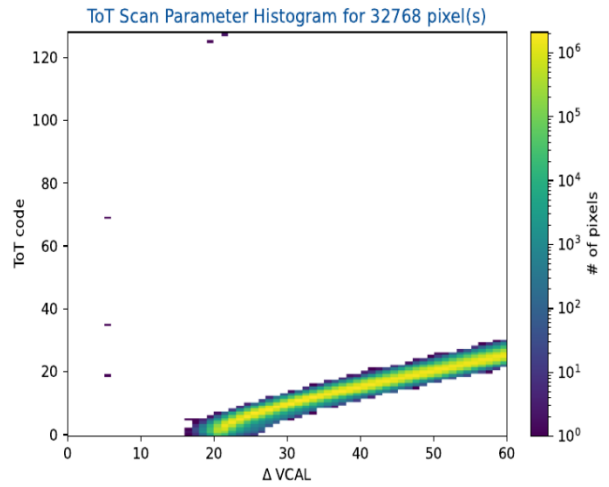

(c) ToT before irradiation.

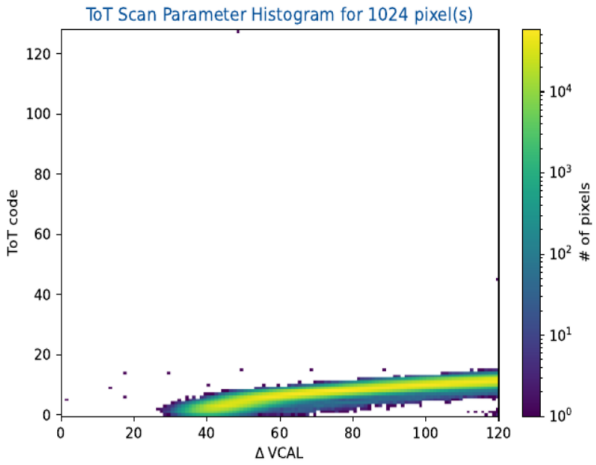

(d) ToT after irradiation.

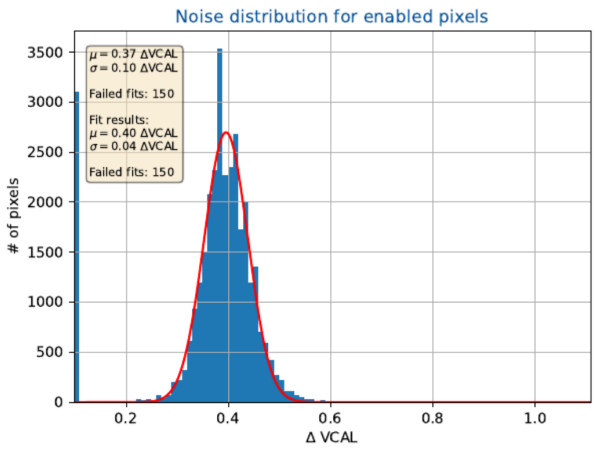

(e) Noise before irradiation.

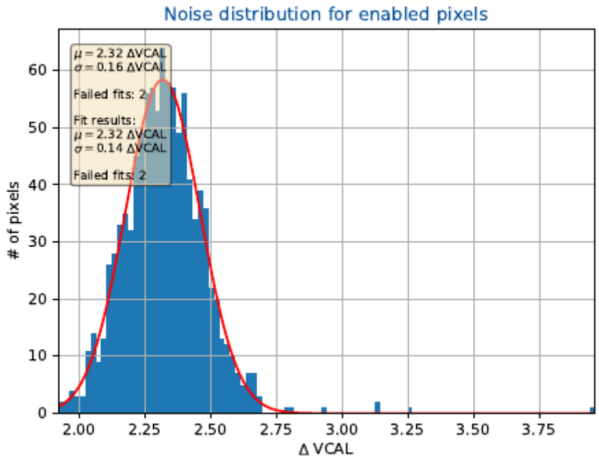

(f) Noise after irradiation.

Figure 5.6: S-curve, ToT and noise distribution before and after irradiation at a fluence of 5×10^{14} 1-MeV-n_{eq}/cm^2 of the HVC front-end of the W8R6 chip at the same settings. The measurements have been conducted at room temperature. In these plots 1 DAC = $18\,e^-$ (see Section 5.3).

- A more complex testing setup is required (e.g. including temperature control).

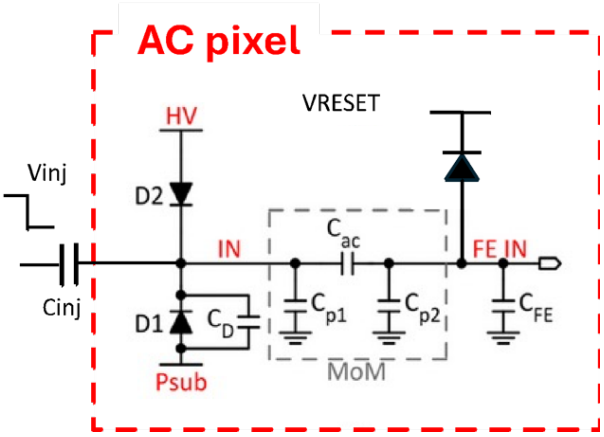

(a) HV pixel

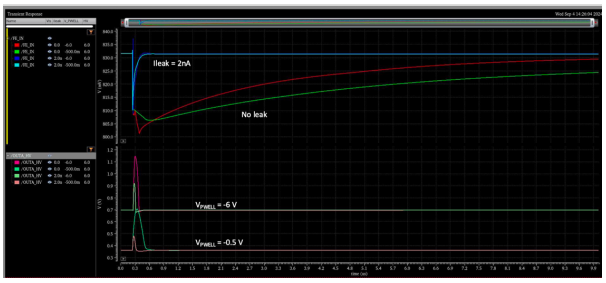

(b) Discharge simulation

Figure 5.7: HV pixel circuit (a), electrode discharge simulation for a leakage current of 2 nA/pixel ((b), by G. Traversi, UNIBG).

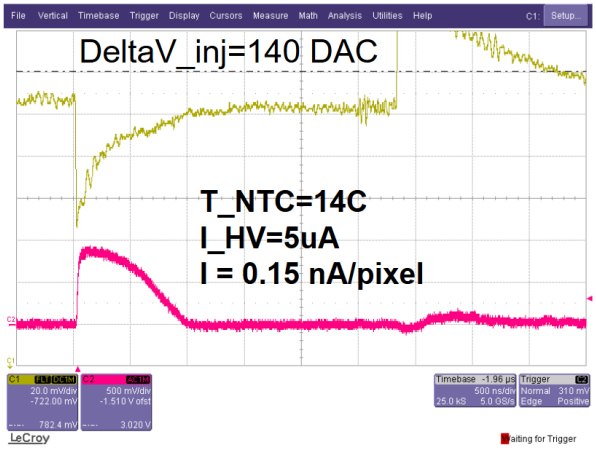

(a) Temperature 14 °C, leakage current 0.15 nA/pixel

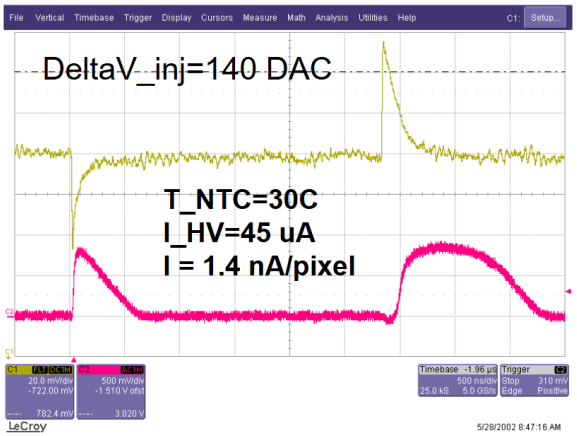

(b) Temperature 30 °C, leakage current 1.4 nA/pixel

Figure 5.8: Electrode discharge dependence on temperature and leakage current.

- Front-end registers must be optimized at different temperatures to maintain low threshold and high efficiency.
- The design of the new VTX detector must include proper monitoring and control of sensor temperature, with a cooling system ensuring operation at sufficiently low temperature to maintain high detection efficiency, still minimizing the material budget.

5.5 Laboratory setup with temperature control

The main goal of this characterization effort was to study the sensor behaviour at different temperatures. As a consequence, the experimental setup needed to be able to heat and cool the chip in a controlled way, while continously monitoring all the relevant parameters.

In particular, in order to avoid damage to the sensor, it is important to avoid both overheating it and cooling it to a temperature lower than the dew point, which could cause condensation on the chip surface. At the same time, the possibility of monitoring the currents of the sensor was needed, which could provide a better overview on their evolution during operation.

To meet these requirements, a dedicated setup (shown in Figure 5.10b) was specifically built in Pisa.

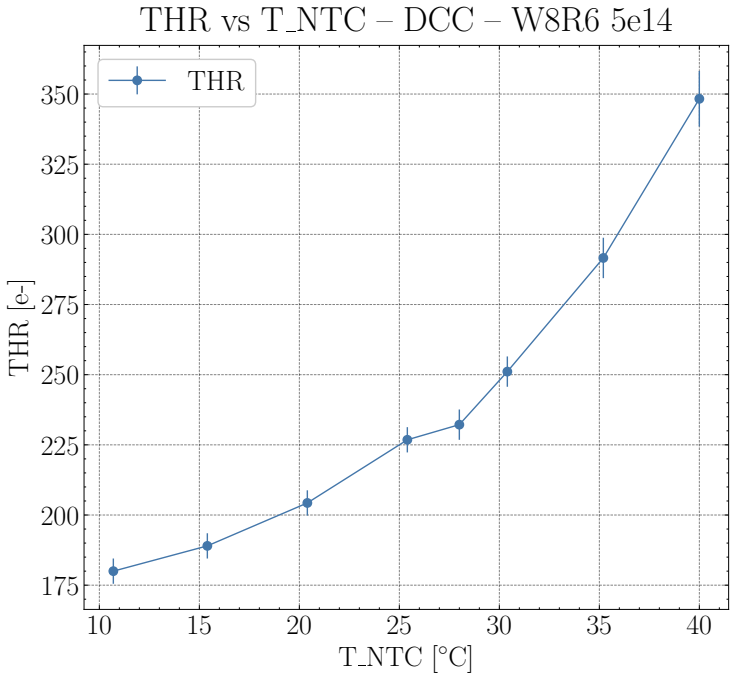

Figure 5.9: Threshold dependence on the temperature of the sensor irradiated with 5×10^{14} 1-MeV-n_{eq}/cm^2 fluence. The error bars are the threshold dispersion.

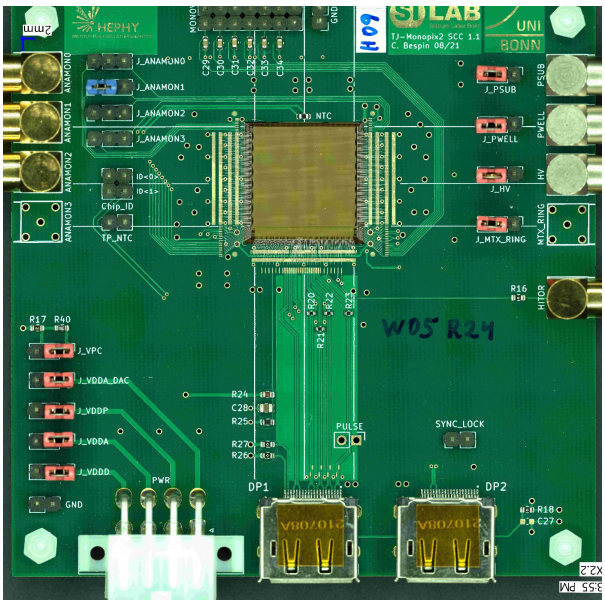

(a) PCB with the chip.

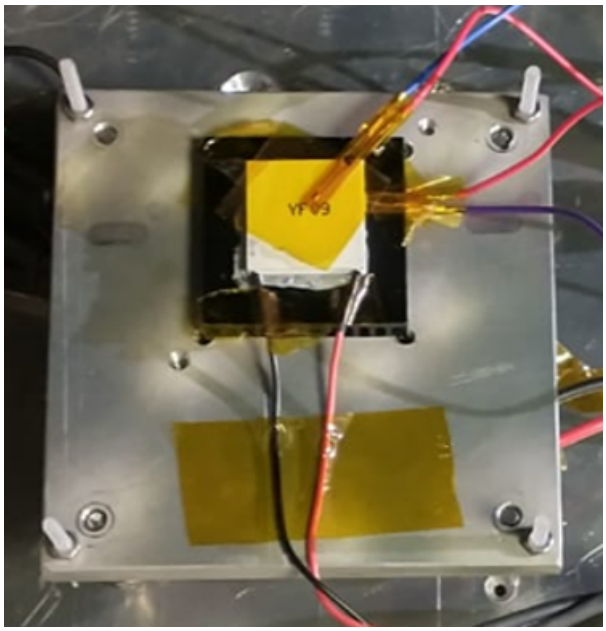

(b) Top view of the laboratory setup used in Pisa.

Figure 5.10: Pictures of the PCB with the chip (a) and of the setup used in Pisa (b). The NTC is placed next to the matrix, while the biasing is provided from the connectors on the top right of the picture.

The setup. This setup allowed temperature control of the sensor using a Peltier cell and a fan for both heating and cooling it. The Peltier cell is a solid state heat pump that exploits the Peltier effect to heat or cool its surfaces when a current is applied to it. Usually one of its surfaces is heated while the other is cooled, allowing temperature control via thermal contact. The temperatures of the chip and the Peltier's sides and the air humidity were monitored using sensors (i.e. NTC, ...) controlled by an Arduino.

The Negative Temperature Coefficient (NTC) thermistors are non-linear resistors that alter their resistance with

temperature. In particular, their resistance decreases at increasing temperatures. As shown in Figure 5.10a, the NTC that monitored the temperature of the sensor is the one placed on the PCB, next to the pixel matrix, while the NTCs that monitored the temperature of the faces of the Peltier cell were placed on top of them.

The thermal coupling between the Peltier and the sensor (while avoiding direct contact that could damage it) was obtained using a thermal conductive film (Keratherm® 86/600).

The temperature on the Peltier cell and the power of the fan were controlled manually by changing the tension provided with dedicated power supplies. The humidity of the air was controlled using a flow of dry air, which helped bringing down the dew point to avoid condensation while operating at low temperatures. The tensions were provided and the currents measured with three different Keithley 2450 source meter units (SMUs).

This setup allowed the testing of sensors in a range of temperature that goes from 12 to 45 °C. The upper and lower temperatures reached were due to a non perfect thermal coupling between the Peltier cell and the sensor and the unsufficient dissipating power of the fan, which could not manage to cool enough the Peltier cell while trying to lower the sensor temperature. Note that from the latest calibrations, conducted at HEPHY, the temperature measured by the NTC (and quoted in this work as T_{NTC}) is $\simeq 7$ °C lower than the actual chip temperature. This clearly needs to be considered when giving the operating limits to the designers of the VTX detector.

The online monitoring. My first contribution to the characterization effort shown in this thesis has actually been the development of the software part of the setup. In particular, I developed the software to monitor the temperatures and humidity and significantly contributed to the remote control of the power supply to smoothen the turning on and off operations of the setup, while also ensuring that the bias was provided in the correct order to avoid damage to the sensor.

All the software is written in Python and, for the online monitoring part, it uses the Qt framework to build the interface. In Figure 5.11 the currents control part of the online monitoring is shown. A similar page was used for the monitoring of the temperatures.

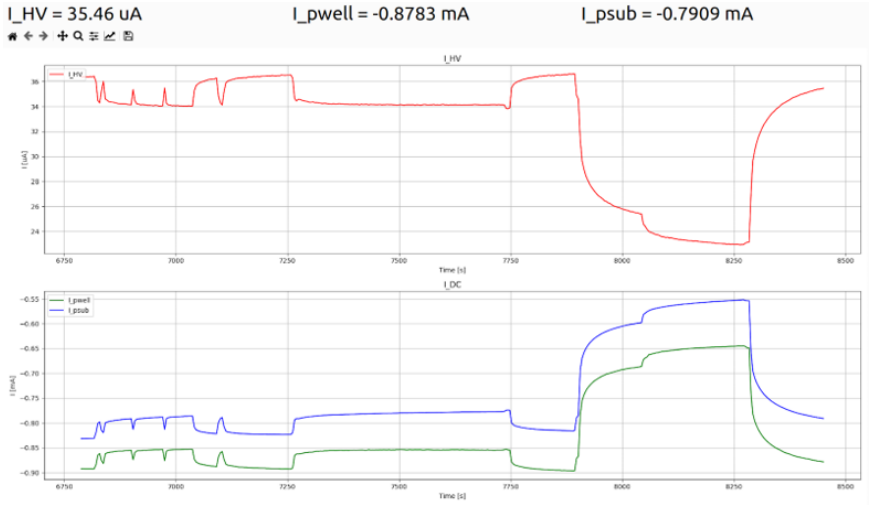

Figure 5.11: View of the current monitor that I implemented in the setup.

5.6 Operation condition tuning and masking procedure

One critical part of the testing and operation of the sensors is their preparation, which mainly consists in tuning their settings to a given target threshold, minimize the threshold disperion with the TDAC tuning, and masking the defective pixels, either those that fire too frequently ("hot pixels") or those that do not function properly.

The main goal of this phase was to establish a reference set of operating parameters for each sensor, providing a reliable baseline configuration with minimal threshold and stable operating conditions. From this reference, only few specific registers could be adjusted to investigate how the sensor's behaviour changes under different conditions, without the need to reestablish the functional configuration each time.

A previous test campaign on a sensor irradiated at a fluence of 5×10^{14} 1-MeV-$n_{\mathrm{eq}}/\mathrm{cm}^2$ indicated that high efficiency could be achieved with a threshold of $\sim 250\ e^-$ at 30 °C. This value has then been chosen as the reference target operating point of the sensors.

The tuning of the settings for the W8R6 chip (irradiated with 5×10^{14} 1-MeV-n_{eq}/cm^2 fluence), which is the one that has been tested the most in Pisa during my work, has been done in previous campaigns [34], with the same settings also used for the other proton-irradiated sensors (with the sole exception of the W2R17's I_{CASN} that had to be lowered to 5). The choice of the starting values of the settings' tuning previously done was made starting from simulations and suggestions of the designers. Note that for the W2R17 sensor (irradiated with 2.5×10^{14} 1-MeV-n_{eq}/cm^2 fluence) it was not possible to reach a threshold lower than $330\,e^-$ in the laboratory and $400\,e^-$ with beams when operating it at 30 °C.

The electron-irradiated one (W2R5), instead, needed a dedicated tuning due to some operating issues and differences in the testing setup with KEK, where it is usually tested. In particular, its DCC front-end could only be operated enabling a maximum of 88 columns and both front-ends could be operated only using different settings.

5.6.1 Hot pixels

When a pixel has a high noise or a low threshold, it can fire with a significantly higher rate than the others, which can deceive the track recostruction algorithm and mimic a hit from a particle. When operating the TJ-Monopix2 sensor, a high Fake Hit Rate (even originating from a single pixel) can block the readout. This issue often arises during internal injection tests, disrupting the measurement procedure.

The most effective way to cope with these *hot* pixels is to disable (or *mask*) them. The masking of these pixels was conducted in an iterative process, which is divided in multiple steps:

- The temperature of the sensor is brought to the minimum allowed by the setup to reduce the leakage current, thus also the noise.
- The matrix of the tested front-end is fully enabled and its TDAC distribution is set to its default value. The threshold of the pixels is set to a high value by lowering as much as possible the I_{CASN} register (see Section 4.2.2).
- For a certain amount of time (usually 100 s) the matrix is operated without injecting charge, in order to see the number of pixels firing due to noise or malfunctionalities (Figure 5.12).

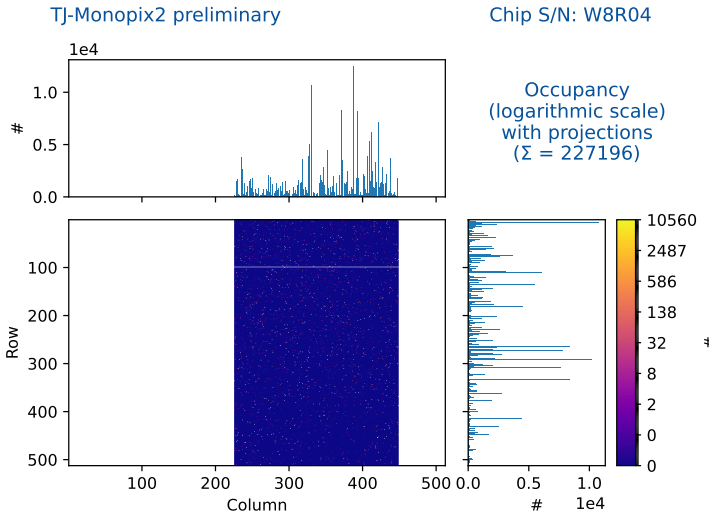

Figure 5.12: Hitmap of the full DCC matrix enabled without injecting charge. Note that the 'Occupancy' quoted in the figure is actually the total number of hits in the matrix.

- These pixels are identified by choosing a cut on the number of hits per second and then are masked (Figure 5.13). The value for the cut is usually chosen at the end of the continous part of the distribution of the number of hits per pixel, to mask only the ones in the tail of the distribution, which usually are the main contributors to Fake Hit Rate.
- The TDAC distribution is then optimized to have the narrowest possible threshold distribution.

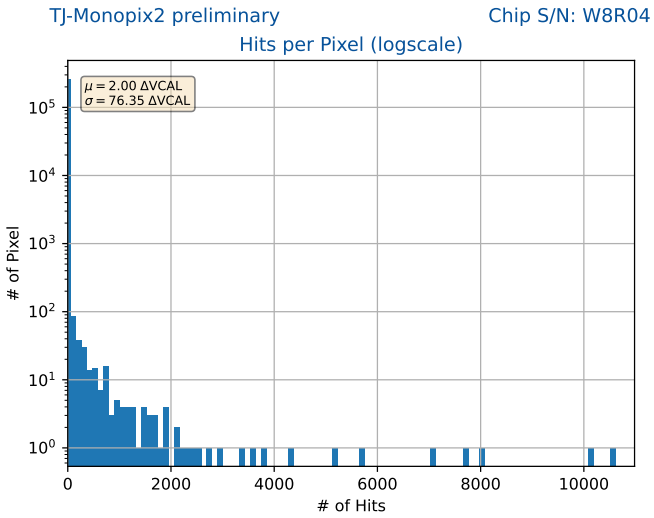

Figure 5.13: Distribution of the number of hits per pixel of the full DCC matrix enabled without injecting charge.

- The procedure is then repeated lowering the threshold by increasing I_{CASN} and increasing the temperature.
- When possible, the cut for the masking is chosen in such a way that the percentage of masked pixels is kept $< 1\%$.

A similar procedure is implemented using radioactive sources, such as ^{55}Fe and ^{241}Am, in order to induce hits on the noisy pixels with an increased rate of hit signals, which cause a cross-talk effect described in previous studies [34]. This cross-talk effect depends on the rising and falling edges of one of the digital signals activated during the readout sequence of a previous hit, which induce a signal at the input of the amplifier. If a pixel has a threshold low enough it can fire when a hit is registered on another pixel in the matrix.

The tuning procedure also requires to mask broken pixels (always trying to keep the masking percentage $< 1\%$) to avoid drops in efficiency due to missing track hits in the tracking algorithm. To easily find them, we searched the pixels that did not record any hit during threshold scans with high maximum injected charge (> 60 DAC). In a similar way, also the pixels with low threshold ($> 5 - 6\,\sigma$ from the average) that had not been masked by previous cuts were identified to be monitored and additional masking was evaluated case by case.

In Table 5.2 the masking percentages of the enabled columns for each chip and front-end are listed. During the scans some common broken rows and columns were found and masked, mainly in the W8R6 and W8R4 sensors (irradiated with fluences of 5×10^{14} and 1×10^{14} 1-MeV-n_{eq}/cm^2), in particular the row 99 and the column 248.

Due to difficulties in operating the W2R5, in particular the possibility to use only a fraction of the DCC front-end (88 columns), this front-end has a higher masking percentage.

Chip	DCC masked pixels [%]	HVC masked pixels [%]
W8R4	0.56	0.19
W2R17	1.08	-
W8R6	0.74	0.19
W2R5	1.50	0

Table 5.2: Masking percentages of the enabled columns of the two front-ends for the four irradiated sensors. Note that for W2R17 only the DCC front-end was tested.

5.7 Results on bulk irradiated TJ-Monopix2 and temperature dependence

As stated in the introduction of this chapter, this characterization effort aimed at determining the temperature dependence of the behaviour of irradiated TJ-Monopix2 sensors. Many measurements have been conducted on the

working DCC and HVC front-ends of the four chips: a measurement of the I-V curve; the measurement of the threshold of the matrix at different settings and temperatures; studies of the cross-talk effect of the clock signal at different configurations, injection phases and temperatures (shown in Section 5.8).

5.7.1 I-V curves

The I-V curve is a measurement of the dependence of the reverse bias current on the bias provided to the sensor. This measurement is conducted to find the maximum bias voltage that can be supplied to the sensor for the operation.

In particular, for the DCC front-end the increased current corresponds to the punch-through effect between the deep p-well and the p-substrate. The gap in the low n-doped layer leaves only depleted p-layer between the two, which is unable to insulate and a current is formed. However, after irradiation the voltage difference between the two layers can be increased, due to changes in the effective doping of the epitaxial layer.

The HVC front-end, instead, can be biased with higher voltages even before irradiation, but a careful assessment of the working condition needs to be done at high voltages (> 40 V) to avoid damaging the front-end.

The dependence of the punch-through voltage (in the DCC front-end) on the radiation damage is shown by Figure 5.14, where the I-V curves for the DCC front-end of the four irradiated sensors are shown. In Table 5.3, the bias provided to the sensors and their front-ends are reported.

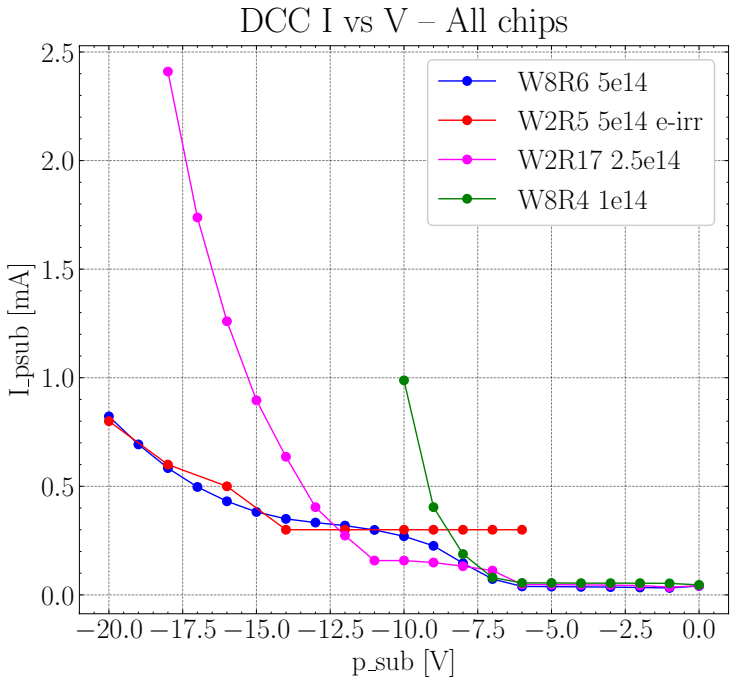

Figure 5.14: I-V curves for the DCC flavor of all the sensors after irradiation.

Chip	Fluence [1-MeV-n_{eq}/cm^2]	Max DCC Bias [V]	Max HVC Bias [V]
W8R4	1	10	35
W2R17	2.5	15	-
W8R6	5	20	40
W2R5	5 e-irradiated	20	40

Table 5.3: Chips' maximum bias for the two front-ends.

5.7.2 Leakage current dependence on temperature

The leakage current of the sensor before irradiation is very small ($\sim$ 30 pA/pixel), and consequently its variation with temperature is negligible. As a result, both threshold and noise remain stable over a wide range of temperature

conditions. In irradiated sensors, however, the substantial increase in bulk-generated leakage current, proportional to the equivalent neutron fluence (Equation 3.6), causes instead significant variations in the sensor characteristics, described in Section 5.4.

The evolution of the leakage current with temperature has been measured in the irradiated samples and it is shown in Figure 5.15.

The measurements show that the evolution of the current with temperature follows the expected one (Equation 3.4) and also the ratio between the leakage current of proton irradiated sensors at the same temperature is $\sim$ equal to the ratio of the fluences, as expected from the NIEL scaling (Equation 3.6).

The electron irradiated sensor, instead, shows a factor of 2 smaller current than the proton irradiated with the same 5×10^{14} 1-MeV-n_{eq}/cm^2 equivalent NIEL fluence, which shows that for the electrons the damage scales differently. This has also been confirmed by the beam measurements presented in Section 6.3.1.

These measurements could not be done on the W2R17 (fluence of 2.5×10^{14} 1-MeV-n_{eq}/cm^2) sensor, because the leakage current is measured from the same port used to bias the HVC front-end, which is broken in this chip.

The reasons for this discrepancy are not yet fully understood, but the observation provides an interesting insight into the behaviour of irradiated TJ-Monopix2 samples. It also highlights the need for caution when comparing bulk damage effects in sensors irradiated with electron and proton NIEL equivalent fluences.

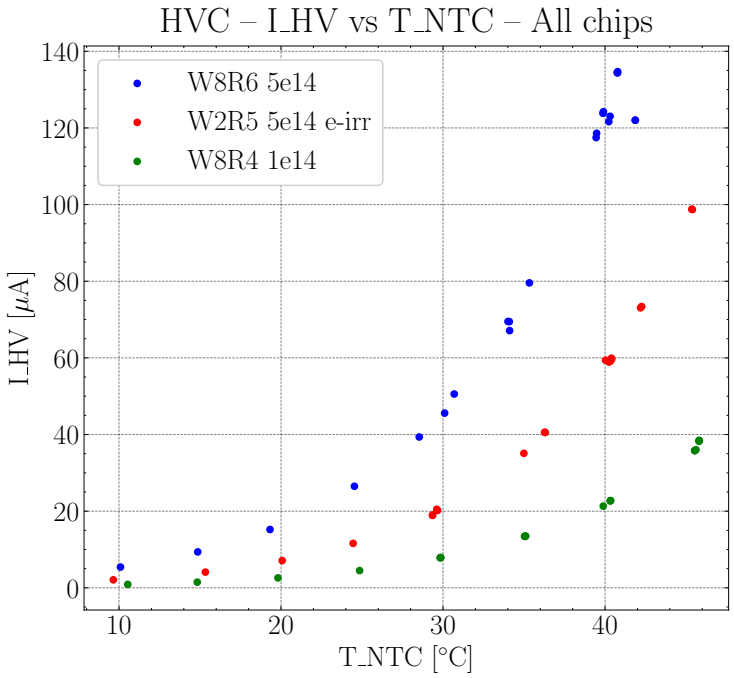

Figure 5.15: Total leakage current dependence on temperature for the HVC flavor of the chips on which the measurement could be conducted. To get the leakage current per pixel it is needed to divide by $64 \times 512 = 32768$, which are all the pixels in the HV and HVC front-ends, from which the total leakage current is collected.

5.7.3 Threshold and noise dependence on temperature

As discussed in Section 5.4, after irradiation, due to the higher leakage current and strong dependence on temperature, also the threshold and noise of the sensors increase with temperature.

This effect is seen in all the irradiated chips, both for the threshold and the noise. While the increase of the threshold can be compensated changing the settings, this is not possible to do with the noise.

In our measurements it has not always been possible to reach the maximum tested temperature (50 °C) due to the high noise and unstable conditions of some front-ends and chips.

The dependence of the threshold and the noise of the four chips on the temperature is shown in Figure 5.16, where a clear exponential-like dependence is seen. Note that the measurements shown are using the *standard* settings, therefore the achieved threshold and noise are not necessarily representative of the minimum values that could be reached for operation at the various temperatures.

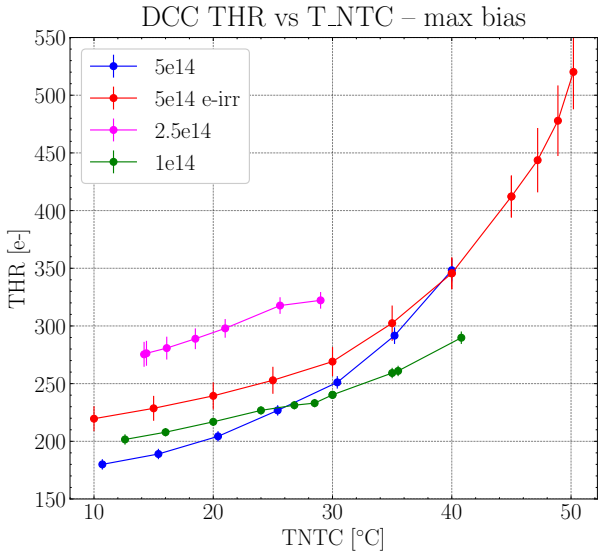

(a) THR DCC

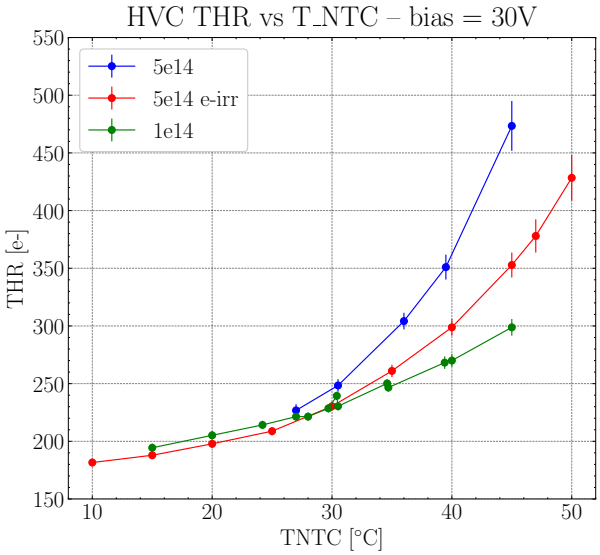

(b) THR HVC

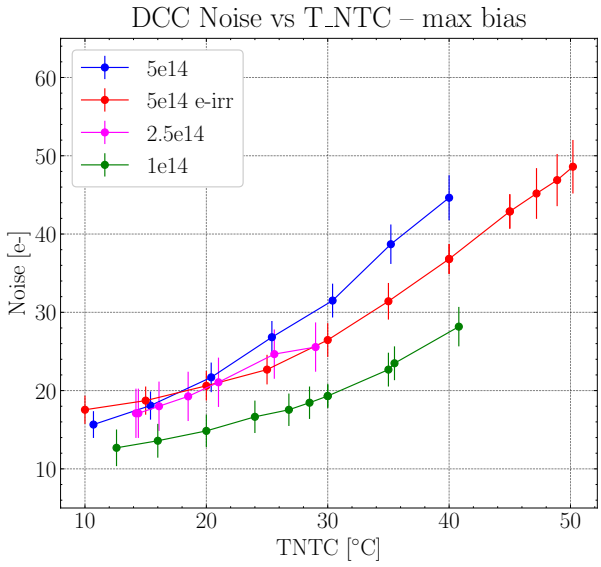

(c) Noise DCC

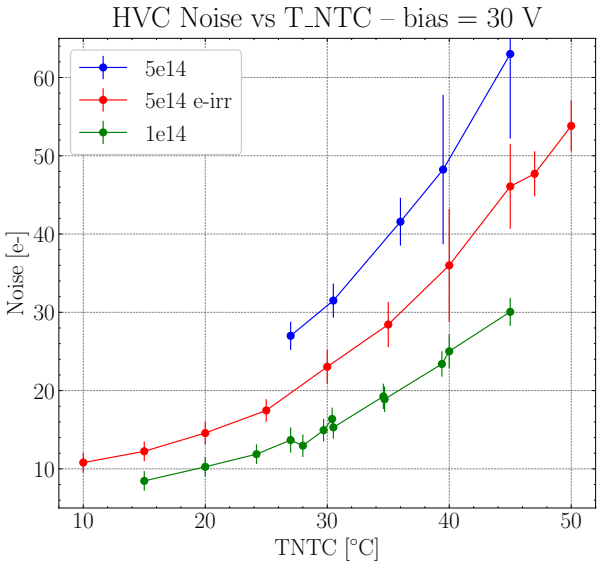

(d) Noise HVC

Figure 5.16: Threshold and noise dependence on temperature for the DCC and HVC flavors of the four tested chips. The error bars are the threshold and noise dispersion.

As shown, the threshold and noise increase with temperature is remarkable, with the threshold more than doubling over the tested temperature range and the noise reaching a value 3 times (DCC) or 5 times (HVC) greater than its minimum one.

As a reference, for a non-irradiated sensor the threshold does not change with temperature and can reach a value of $\sim 200\,e^-$, while the noise is limited to $\sim 7\,e^-$.

Threshold dependence on I_{CASN}. An important part of the measurements at the Test Beam was the dependence of the sensor efficiency on the operating front-end threshold, which can be set and varied with different registers, such as I_{CASN} (see Section 4.2.2), which changes the threshold of all the enabled matrix.

This register has been the main tool to set the global threshold of the tested front-end in most of the tests conducted in order to prepare the different configurations of the sensors for the operation at beams. In this way, a wide range of thresholds could be reached, as shown in Figure 5.17 with the data from the W2R5 chip (the electron irradiated one), with values spanning over more than 300 e^-.

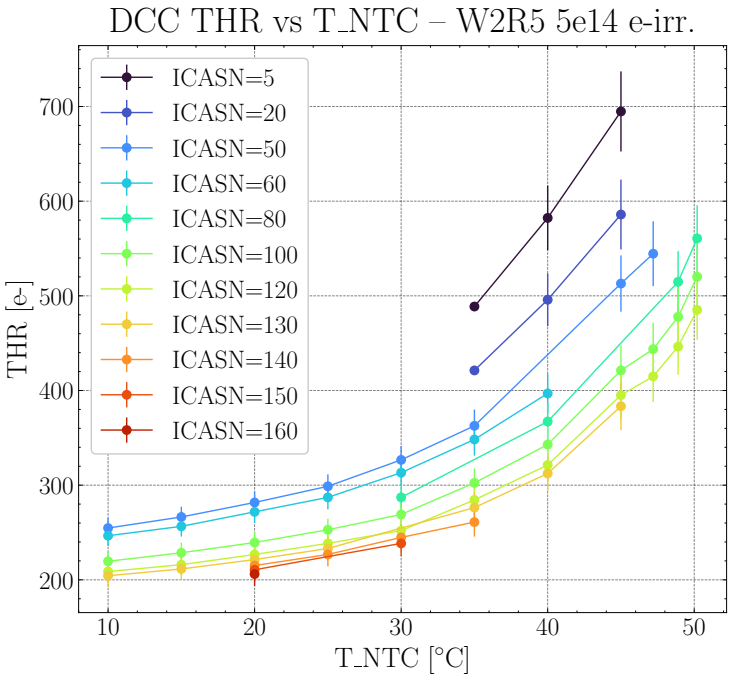

Figure 5.17: Threshold dependence on temperature and I_{CASN} for the DCC flavor of the W2R5 chip. The error bars are the threshold dispersions.

5.7.4 Fake Hit Rate

Another important part of this testing campaign, in particular in tests with beams, was the measurement of the Fake Hit Rate (FHR), the rate per enabled pixel of the hits not associated to a particle (or to the injection of a signal). This value is given by:

$$\mathrm{FHR} = \frac{N_{\mathrm{hits}}/N_{\mathrm{pix}}}{t_{\mathrm{acq}}} \tag{5.12}$$

where the N_{hits} is the total number of hits during the acquisition, N_{pix} is the number of enabled pixels and t_{acq} is the acquisition time.

Its importance lies in the necessity of operating the detector with a limited value of pixels firing while not associated to tracks. For reference, the target specifications for the hit rate in the innermost layer of VTX are of 120 MHz cm^{-2} (driven by the expected background extrapolation at the target luminosity), which correspond to a hit rate per pixel of 1.3×10^3 Hz/pixel. Fake hit rates smaller of 3 orders of magnitude than this target value are then totally acceptable.

In particular, the fake hit rate measurements aimed at comparing the two tested front-ends, to see if they could keep a low FHR and if there were differences amongst them. This last point was particularly critical, since the test beam results had already showed that the DCC front-end was more radiation resistant than the other, but the HVC seemed to have a lower average fake hit rate during data taking, despite similar noise levels were measured during the laboratory characterization and the operating threshold was similar.

Measurement. It is of crucial importance to measure the FHR at the operating conditions and at different temperatures, to fully characterize the behaviour of the sensor.

While the effort to implement an efficient way of extracting the FHR information from the beam data is ongoing, a different approach has been pursued to find an estimate of this value from measurements in the laboratory. In particular, the FHR was measured by operating the matrix for a given acquisition time, without injecting charge or using radioactive sources, in the same way as in the procedure to mask the noisy pixels, and then extracting the FHR from the number of hits registered using Equation 5.12.

In these measurements, clearly, it was essential to operate the sensors under conditions as similar as possible to the ones at the operation at the Test Beam. For this reason, the same setup used there (presented in Section 6.1.3) was used for these measurements.

The presented measurements have been done in the laboratory on the W8R6 sensor, which is expected to have the highest FHR due to the highest radiation damage.

In Figure 5.18 the results of these measurements are shown for the DCC and HVC front-ends, operated with standard settings at different temperatures. The HVC front-end shows a lower value of the FHR than the DCC, especially at low temperatures, while the results are similar at $T_{\mathrm{NTC}} = 40$ °C.

The DCC front-end, however, remains below the 10^{-2} Hz/pixel level, which is totally acceptable considering the expected hit rates on the inner layers of VTX.

Other measurements, not shown here, show a significantly higher FHR value (~ 1 Hz/pixel) when the sensor is operated in conditions with a smaller difference between the baseline and the threshold voltage, which highlights the necessity to keep that difference high enough to avoid many noise hits, especially in conditions in which the ENC and the BCID cross-talk (see Section 5.8) are large, for example at high temperatures.

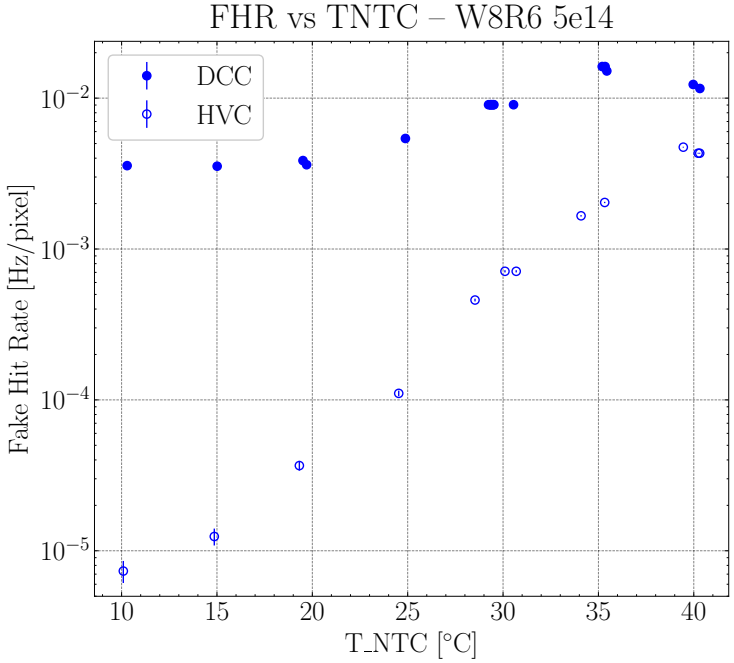

Figure 5.18: Fake Hit Rate of the DCC and HVC front-ends of the W8R6 (irradiated with 5×10^{14} 1-MeV-n_{eq}/cm^2 fluence) sensor for different temperatures.

5.8 Digital cross-talk: results on irradiated samples

A relevant part of this characterization work has been the study of the cross-talk effect of the sensor's clock.

TJ-Monopix2 is equipped with a 7-bit gray encoded 40 MHz counter, called Beam Crossing ID (BCID) counter, that should be distributed over the entire matrix to sample, at the pixel level, the leading and trailing edges (LE/TE) of the hit, then used for Time Over Threshold measurements. The BCID counter distribution could be selectably enabled to individual double columns.

BCID cross-talk From precedent studies [35], it has been shown that the distribution of this BCID counter induces a cross-talk that alters the threshold of the sensor depending on the arrival time of the hit with respect to the phase of the BCID. During the measurements performed with internal injection using a signal injection timing that can be varied with respect to the BCID counter phase, the measured threshold changes significantly as a function of the injection time delay (i.e. the arrival time of the hit), as shown in Figure 5.19, with a variation up to $100\,e^-$ when the BCID is enabled in the entire matrix.

In particular, it has been shown that this effect is due to the toggling of the two least significative bits of the BCID. The origin of this effect has been attributed to the distribution of the BCID counter, as demonstrated by the absence of threshold variation when the BCID is disabled.

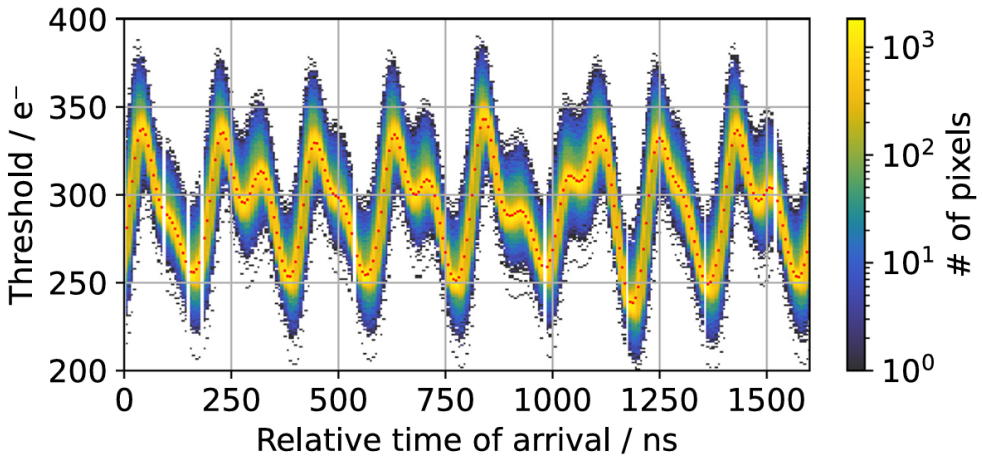

Figure 5.19: Threshold dependence on the arrival times of the hit with respect to the reset of the BCID counter (from [35]).

The characterization of this cross-talk effect required detailed measurements, either with the clock enabled and disabled and also varying the delay of the injection of the charge with respect to the reset of the clock counter.

From these measurements also a linear dependence of the threshold variation on the size of the matrix where the BCID distribution is enabled has been found (shown in Figure 5.20), which suggests that the magnitude of this effect could be up to 60% larger in OBELIX, due to a larger matrix size if countermeasures are not applied.

During the characterization in the laboratory, the effect of the BCID cross-talk could be removed since the arrival time of the hits is fixed with the injection timing, while in the operation with particles, with random arrival phase, the corresponding large random threshold fluctuation has a large impact on the operation of the sensor. This corresponds in fact to an increased effective noise, with an additional term added to the thermal noise, particularly critical when operating the sensor at low threshold after irradiation.

The effects of the BCID cross-talk on the operation with particles is discussed in detail in Section 5.8.2.

This characterization of the BCID cross-talk in irradiated samples, which is extremely critical for the future operation, has highlighted the necessity of introducing appropriate countermeasures in the OBELIX design, which are now being implemented.

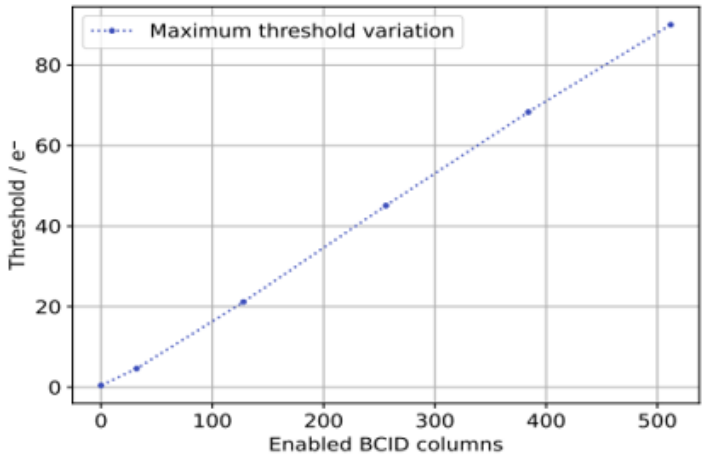

Figure 5.20: BCID cross-talk effect dependence on the number of enabled columns.

5.8.1 Threshold variation with injection time

The majority of the tests conducted in laboratory uses the internal injection circuit of the chip to simulate a charge deposit. In the standard procedure, the clock counter is reset and then the signal is injected in the first pixels

of the enabled double columns. The delay of this injection with respect to the reset of the clock counter can be controlled with a parameter, called *PulseStartCnfg*, whose value corresponds to this delay in units of 3.125 ns, up to a maximum of 64. In the following, the delay will be referred to using the value of this parameter. Changing this parameter, therefore this delay, the threshold of the sensor varies quite significantly (up to $\sim$ 40% of the minimum value), which makes the study of this dependence of great interest to understand eventual challenges to the operation of the sensor.

When deciding a standard procedure for all the sensors, the sensor irradiated with 5×10^{14} 1-MeV-n_{eq}/cm^2 fluence (W8R6) has been used as a standard. From measurements on this chip, it can be seen that the minimum of this threshold variation for the DCC front-end is at PulseStartCnfg = 19, while its maximum is at PulseStartCnfg = 45. The minimum has been chosen as the default value for the injection tests, while the maximum has been used as the reference value to determine the amplitude of this effect.

Since there is a propagation delay of the injection signal across the pixel of a column of the order of 30 ns, the effective injection time with respect to the BCID reset changes along the column, and the threshold could also be different along the column due to this additional delay. The threshold dispersion along the column depends on the slope of the threshold variation at different delays. For this reason it was decided to set the default injection phase to the value at the minimum of the curve, to reduce this threshold dispersion.

In these measurements, the values PulseStartCnfg = 30 and 35 have also been used, in order to study the behaviour of the sensor at the values of the injection delay where the slope of the threshold variation is maximum and its dispersion is largest.

The tests on the HVC front-end have shown that it has a different threshold dependence on the injection delay from the DCC, with the minimum of the threshold found at PulseStartCnfg = 25 and the maximum at PulseStartCnfg = 60.

In Figure 5.21, the threshold variation for both the front-ends of the tested sensors are shown, which show the quite dramatical change in threshold at different injection delays.

In Table 5.4 the maximum variations of the threshold for the different irradiated chips are listed for the two front-ends. These values are used to measure the effective threshold seen by the particles, as explained in Section 5.8.2.

Chip	Fluence [1-MeV-n_{eq}/cm^2]	ΔTHR DCC [e^-]	ΔTHR HVC [e^-]
W8R4	1	57	33
W2R17	2.5	58	-
W8R6	5	100	72
W2R5	5 e-irradiated	100	60

Table 5.4: Maximum threshold variation at different Pulse for the two front-ends of the four irradiated chips. The ΔTHR are all taken at 30°C.

Crosstalk effect dependence on temperature From our measurements, a clear indication of the dependence of this effect on the operating temperature has been seen, since the magnitude of the variation increases with temperature and dominates over other effects, such as threshold dispersion and noise.

In Figure 5.22, the dependence of the threshold on both the injection delay and the sensor temperature is shown for the DCC front-end of the W8R6 chip, the one irradiated with maximum fluence. As expected, the dependence of the threshold on the injection delay does not change with the temperature, keeping the same maxima and minima, while the amplitude of the threshold variation increases with it.

The tests on the temperature dependence have also been conducted on the HVC front-end, at the same PulseStartCnfg values (19, 35 and 45) used for the DCC front-end, in order to standardize the procedures, which clearly can not fully measure the threshold variation at different temperatures and injection delays.

5.8.2 Effect of the BCID cross-talk on operation with particles

Tests and measurements presented so far have been conducted with internal injection, with a fixed injection delay and always resetting the BCID counter before the injection. While this smoothens the testing process, it does not reproduce the real threshold seen by the signal from a particle. This is due to the fact that particles arrive on pixels with a random delay with respect to the BCID counter reset, which implies that the actual threshold of the pixel can vary significantly, according to the behaviour seen before.

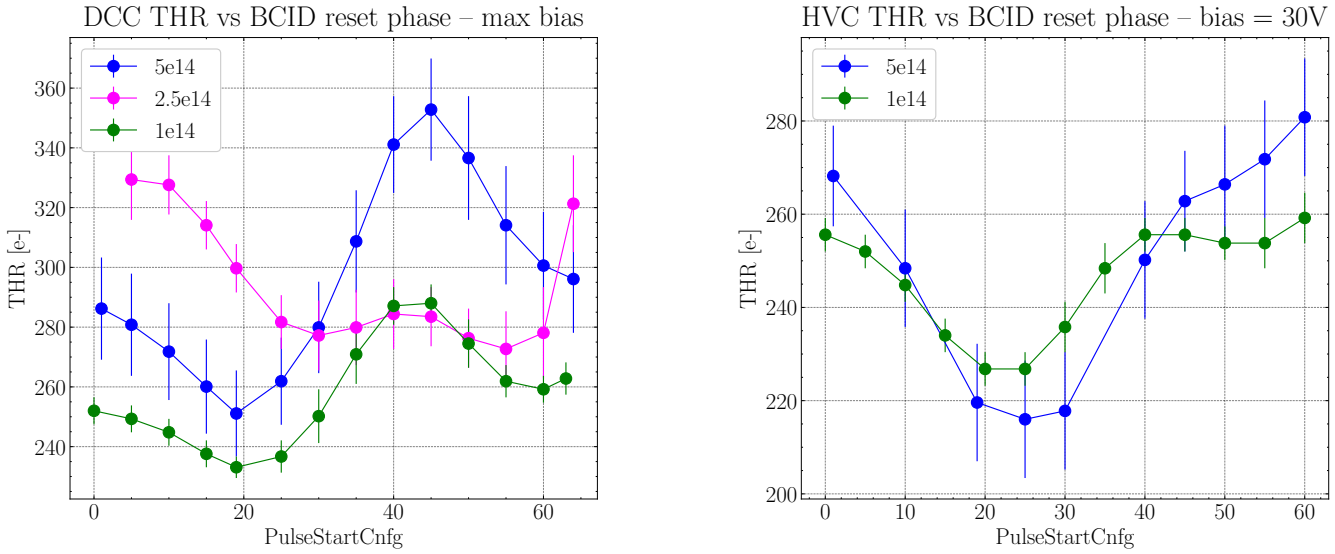

(a) DCC (b) HVC

Figure 5.21: Threshold dependence on the BCID reset phase for the DCC and HVC front-end of the tested chips. The error bars are the threshold dispersions.

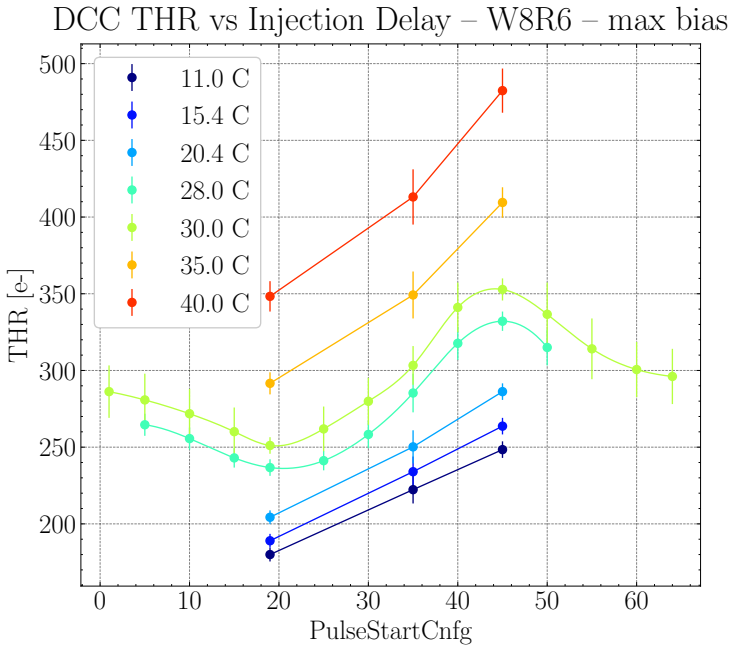

Figure 5.22: Threshold dependence on injection phase with respect to BCID reset for different values of temperature for the DCC flavor of the W8R6 chip (irradiated at maximum fluence). The curves for the 28 °C and 30 °C measurements are given by a spline interpolation, while for the other temperatures a linear interpolation between consecutive points has been chosen, due to the reduced number of measurements that did not allow to use the spline. The error bars are the threshold dispersions.

In particular, depending on the arrival time of the hit, the sensor threshold can cover the entire threshold distribution, with an effective threshold given by Equation 5.13.

$$\mathrm{THR}_{\mathrm{eff}} = \mathrm{THR}_{\mathrm{min}} + \frac{\Delta\mathrm{THR}}{2} \tag{5.13}$$

The random fluctuation of the threshold seen by the particle can be regarded as an additional noise, resulting

in an effective noise expressed by Equation 5.14. The ΔTHR from BCID cross-talk is $\sim 100\,e^-$, which is more than an order of magnitude higher than the thermal noise before irradiation ($\sim 5-10\,e^-$), and the effect scales with the number of pixels, which means that it will be $\sim 160\,e^-$ in OBELIX, due to a larger matrix (×1.6 the TJ-Monopix2 one).

$$\mathrm{NOISE_{eff}} = \sqrt{\mathrm{NOISE_{th}^2} + \left(\frac{\Delta\mathrm{THR}}{2}\right)^2} \tag{5.14}$$

The quantities in Equation 5.13 and 5.14 are shown in Figure 5.23.

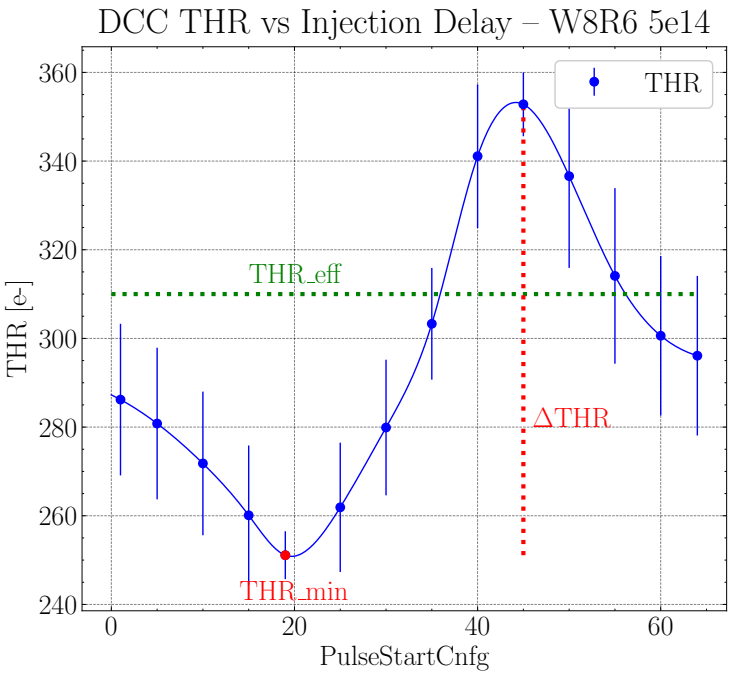

Figure 5.23: Summary of BCID cross-talk effect: the variation of the threshold with the injection delay, the effective threshold seen by the particles $\mathrm{THR_{eff}}$, the amplitude of the variation ΔTHR. The error bars are the threshold dispersion.

Figure 5.24 summarizes the various contributions relevant to define the minimal threshold to operate the sensor. As discussed in Section 5.2 and according to Equation 5.5, to have a stable operation the threshold of the sensors should be set to about 5-6 times the global fluctuations due to the noise $\sigma_{\mathrm{eff\_noise}}$ Due to the BCID cross-talk, also the threshold dispersion and the threshold variation due to the cross-talk enter into the equation:

$$\mathrm{THR} > \mathrm{THR_{min}} = 5\sigma_{\mathrm{eff\_noise}} = 5\sqrt{\mathrm{NOISE_{th}^2} + \left(\frac{\Delta\mathrm{THR}}{2}\right)^2 + \sigma_{\mathrm{thr}}^2} \tag{5.15}$$

All these terms are shown in Figure 5.24 as a function of the temperature, from which is clear that the BCID cross-talk is by far the dominating term even at high temperature, where the noise due to the increased leakage current is significant. For example, at $T_{\mathrm{NTC}} = 30$ °C (taken as a reference), the thermal noise is $30\,e^-$, with the contribution from the BCID cross-talk that is a factor 2 higher.

Considering the contribution in Figure 5.24, the minimal stable operating threshold (from Equation 5.5) is also shown as comparison.

These measures show that the current operating threshold of TJ-Monopix2 is slightly above the minimum needed for a stable operation, with very little margin for improvement, since the threshold is between 5 and 6 $\sigma_{\mathrm{eff\_noise}}$. For this reason it is not possible to easily lower the threshold, as was also noted during the Test Beam, due to the increased Fake Hit Rate.

Since in OBELIX this cross-talk effect (which is the dominant term in Equation 5.15) should not be present, the $\sigma_{\mathrm{eff\_noise}}$ will be lower and it will be possible to operate the sensor at even lower thresholds.

The effective threshold can also be estimated using internal injection tests without resetting the clock counter before the injection, simulating the arrival of particles with random delays with respect to its reset.

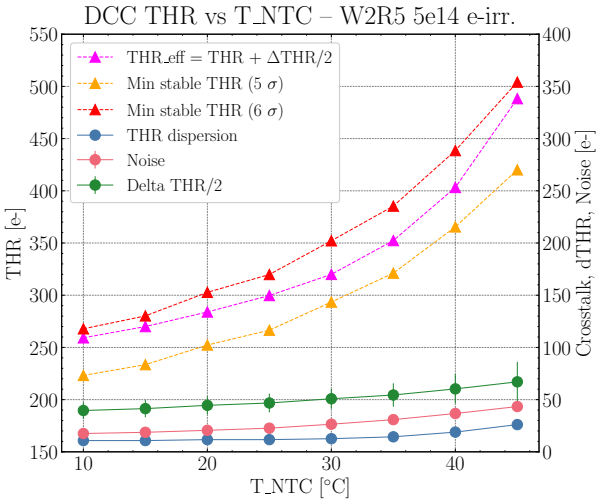

(a) W2R5 e-irradiated

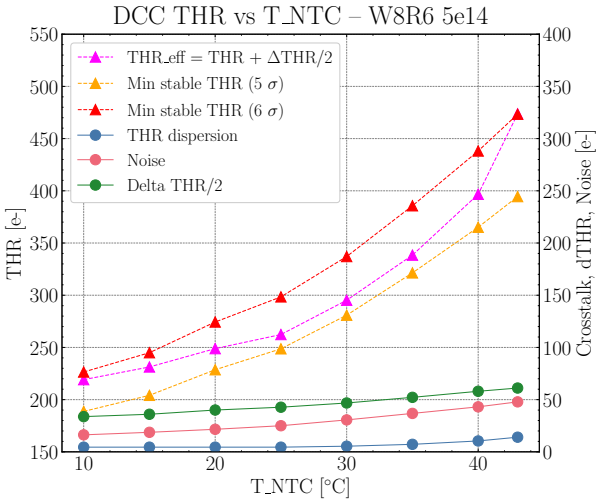

(b) W8R6 p-irradiated

Figure 5.24: Effective threshold, threshold dispersion, noise and (half) magnitude of the BCID effect at increasing temperature. The error bars are the threshold and noise dispersions. The minimum stable thresholds at 5 and 6 σ from the effective noise are also plotted.

Analysis method. While injection tests with fixed delay show a monotone occupancy curve, which can be analyzed with Equation 5.7, this is not the case for tests with random delay. For this reason, a different method from the S-curve has been used in order to measure the threshold in the case without BCID reset.

This method computes the threshold for each pixel as the weighted average of the injected charge, where the weights are given by the occupancy, such that occupancy = 0.5 has weight 1, while occupancy = 0 or 1 has weight 0, and anything in between is linearly interpolated. The noise is computed as a variance with the aforementioned weights.

In Figure 5.25 an example of this measurement is shown for the DCC front-end of the W8R6 sensor, the one irradiated with 5×10^{14} 1-MeV-n_{eq}/cm^2 fluence.

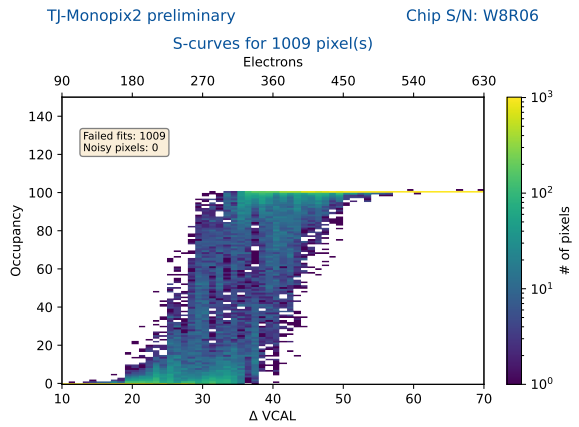

(a) Cumulative S-curve without BCID reset for the full matrix of the DCC flavor of the W8R6 chip.

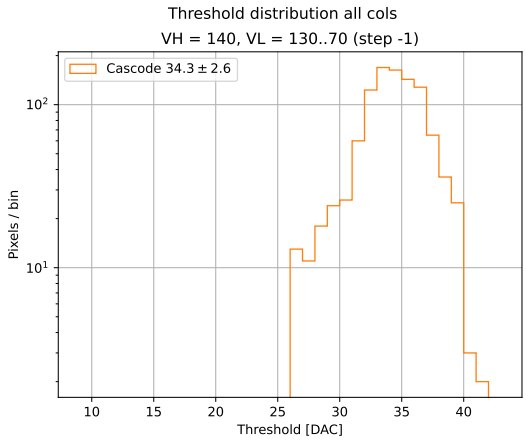

(b) Threshold distribution without BCID reset for the full matrix of the DCC flavor of the W8R6 chip.

Figure 5.25: S-curves and measurement of the threshold for the DCC front-end of the W8R6 (irradiated with maximum fluence), without using a fixed injection delay.

5.8.3 Threshold variation with BCID counter state

The detailed characterization of this cross-talk effect, therefore, requires a complete set of measurements done with different states of the BCID counter with respect to the injection: fixed delay, no reset (to emulate a random phase as for particles) and BCID not enabled (to remove the cross-talk). The measurements at fixed delay considered were the ones at PulseStartCnfg = 19 and 45.

As shown in Figures 5.27 and 5.29 for the two cascode front-ends of the W8R6 sensor (proton irradiated with 5×10^{14} 1-MeV-n_{eq}/cm^2 fluence), the hypothesis that the threshold measured without a fixed delay is equal to the effective threshold THR_{eff} is validated by the compatibility of the two data curves.

Measurements in Figures 5.27 and 5.29 show that due to the BCID cross-talk the effective threshold seen by the particles (with a random arrival time) is about 13-25% higher than the THR measured with injection with the default injection delay set to Pulse = 19.

The results for the HVC front-end are clearly different, since the threshold values taken with a fixed injection delay are not the extreme points of the threshold variation curve.

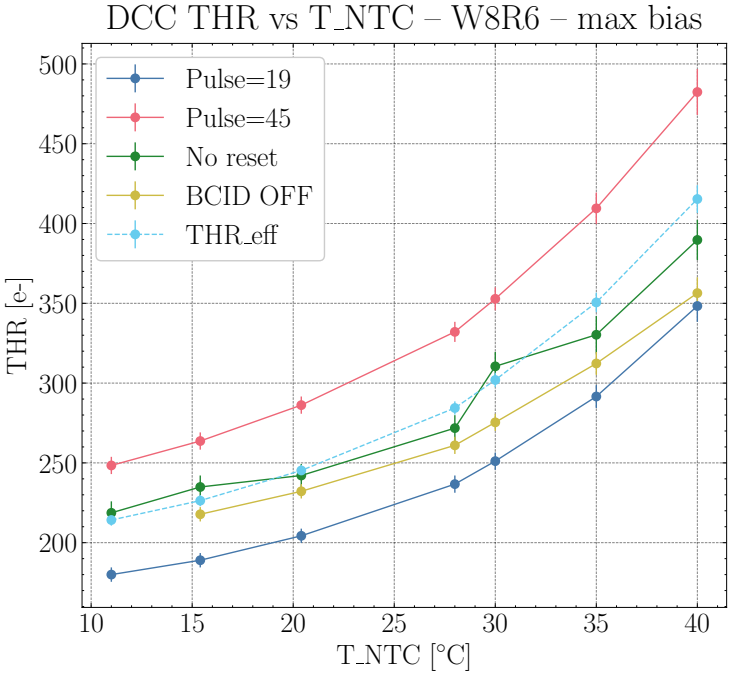

Figure 5.26: W8R6

Figure 5.27: Threshold dependence on temperature for the DCC flavor for different states of the BCID counter of the chip irradiated with maximum fluence. In particular, the cases with PulseStartCnfg = 19 and 45 are considered, together with the measurements without a fixed injection delay, the THR_{eff} computed with Equation 5.13 and the measurements with the clock distribution disabled. The error bars are the threshold dispersions.

5.8.4 Consequences on TDAC tuning

When operating with internal charge injection at a fixed delay relative to the reset of the BCID counter, this delay corresponds to the one valid for the first pixel of the column, but varies across it. The injection signal propagates sequentially through the double column, reaching subsequent pixels with an increasing delay relative to the BCID reset. As a result, the effective timing of the injection varies along the column.

The maximum value of the propagation delay is $\sim$ 30 ns, which is $\sim$ 1/3 of the half period of the threshold variation with the injection delay. For this reason, this additional delay across the column could change significantly the threshold of the pixels, creating a gradient along the double column.

When measuring the threshold of the sensor at a nominal delay, the quoted result is the mean of the threshold distribution of all the pixels of the column, which contribute with thresholds at different effective injection delays. This implies that the measured threshold for a given PulseStartCnfg value is not the actual threshold of the pixels with that nominal delay, but the average of a smeared distribution.

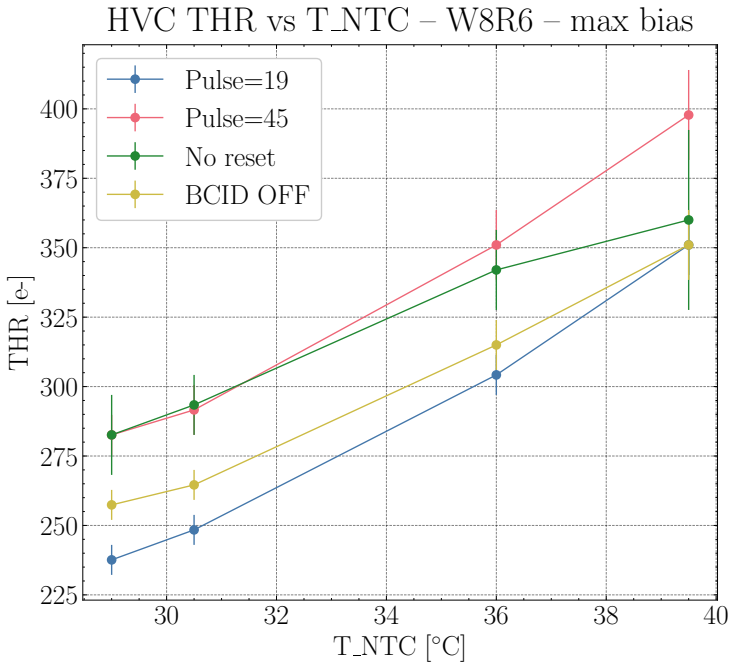

Figure 5.28: W8R6

Figure 5.29: Threshold dependence on temperature for the HVC flavor for different states of the BCID counter of the chip irradiated with maximum fluence. In particular, the cases with PulseStartCnfg = 19 and 45 are considered, together with the measurements without a fixed injection delay and the measurements with the clock distribution disabled. The error bars are the threshold dispersions.

A consequence of this injection-induced gradient is that, as shown in Figure 5.30, the threshold dispersion is higher when the gradient (represented by the red dots, which correspond to the difference between the maximum and minimum threshold across the columns) is higher. The dispersion, therefore, is maximum for the values of PulseStartCnfg which correspond to the maximum of the slope of the threshold variation (e.g. 30 or 35 for the DCC front-end).

TDAC tuning. The injection is also used during the TDAC tuning, described in Section 5.2. Therefore the delay from the propagation of the injection delay across the column might affect the measured threshold during this procedure.

The aforementioned gradient, therefore, is also induced in this procedure, meaning that the tuning algorithm tries to compensate for it in order to align each pixel's threshold with the target value. As a result, the TDAC distribution shows an anticorrelated gradient, effect of this compensation.

It is important to stress that the threshold gradient across the column, due to the injection delay, is only present during the tests with injection and not in operation with particles, which have random arrival times. Thus this threshold gradient compensation with the TDAC tuning can create an artificial gradient across the column for the threshold seen by the particles.

Measurements on a non-irradiated chip. A concern that comes from this induced gradient on the TDAC distribution is that it could hinder the operation of the sensor, due to a too large threshold difference along the double columns. This could, for example, create a gradient in the efficiency of the sensor.

Clearly, if this was the case, the threshold tuning process should be changed accordingly, in order to avoid this consequence.

Since the measurements aimed at the validation of the procedure, a non-irradiated sensor (W8R13) has been tested, in order to avoid possible effects of the irradiation that could have altered the results. Since the BCID distribution is carried out in groups of 16 double columns, the tests were conducted on one of those, with the following measurements in sequence:

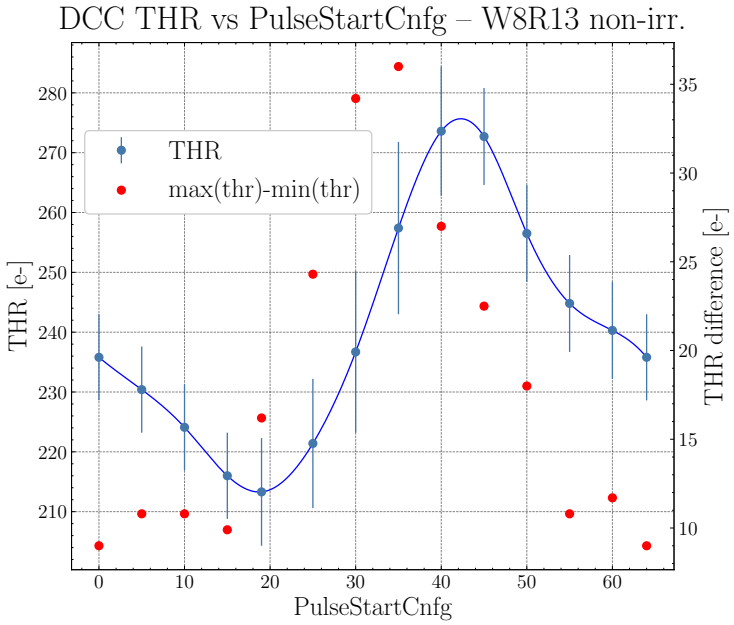

Figure 5.30: Average threshold and maximum threshold difference across a column variation as a function of the injection phase with respect to BCID reset for the DCC flavor of the W8R13 non-irradiated chip. The error bars are the threshold dispersion.

- A first measurement of the threshold, setting TDAC=4 on all the pixels, to evaluate the threshold gradient induced by the charge injection propagation delay along the 512 pixels of the column. Figure 5.31a shows the average threshold of the pixels as a function of their position along the column (row index), that clearly shows a gradient as expected, due to the injection delay of the injection signal. The average threshold of all pixels is also used as the target threshold for the following step.

- A TDAC tuning with target threshold the average threshold of all pixels from the previous measurement. Figure 5.31b shows the results of the TDAC values obtained to equalize the threshold that clearly shows an anticorrelated gradient along the columns. Higher TDAC values have to be applied to compensate the threshold gradient visible in Figure 5.31a.

- Another measurement of the threshold with the new TDAC distribution applied to verify that the tuning has effectively compensated the gradient. Figure 5.31c shows the average threshold of the pixels as a function of their position along the column, after the TDAC tuning, where, excluding the first 100 rows, the tuning has mostly compensated the threshold gradient.

- A measurement of the threshold without a fixed injection delay and applying the TDAC tuning to measure the threshold distribution seen by real particles. Figure 5.31d shows again a threshold gradient in the region with row number > 100, since now the TDAC is applied but the effect that it was supposed to compensate is no longer there, with a random time of the injection with respect to the BCID counter reset.

In all the measurements there is a clear structure in the first ~ 100 rows, with a slight monotone increase of the threshold, which has been diagnosed as an effect of the W8R13 chip unrelated to the measurements conducted.

The effect of the TDAC tuning procedure, related to the BCID cross-talk and the injection propagation delay along the column has then been confirmed with these measurements.

As can be seen in Figure 5.31: the TDAC distribution after the TDAC tuning is in anticorrelation with the threshold gradient present in the first measurement, due to the algorithm attempt to compensate it; in the second threshold measurement this compensation is working and the threshold is almost flat for row numbers > 100, since in most cases the tuning manages to cancel the gradient in the threshold distribution, leveling it to the target value; in the last threshold measurement it is again appearing a threshold gradient correlated with the TDAC one, due to the absence of the threshold gradient from the injection propagation effect, since the BCID reset is not applied and the arrival time of the injection is random.

The threshold gradient visible in the last figure (Figure 5.31d) is a measurement of the effect of a potential residual bias from TDAC tuning, done with the injection propagation delay just described, when operating with particles.

The measurements shown in Figure 5.31 have also been performed for the W8R6 (proton irradiated with 5×10^{14} 1-MeV-n_{eq}/cm^2 fluence), showing the same results (residual bias due to the TDAC tuning $\sim 20\,e^-$), thus confirming that this effect remains the same even after irradiation.

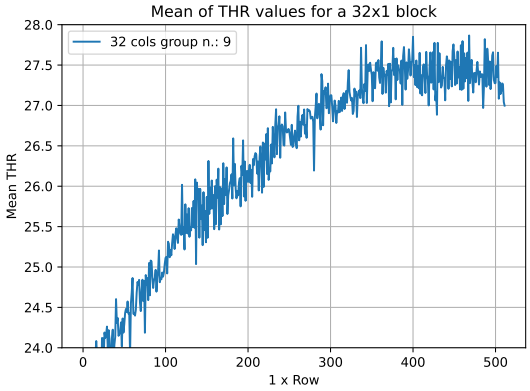

(a) Threshold (fixed injection delay, Pulse = 19) with no TDAC tuning (TDAC = 4).

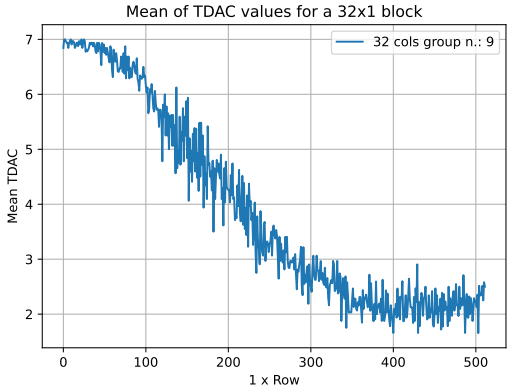

(b) TDAC values obtained during the threshold tuning procedure.

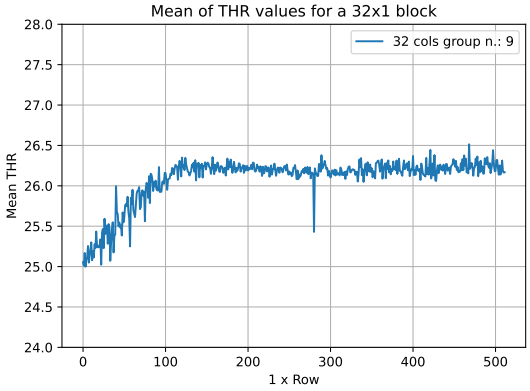

(c) Threshold (fixed injection delay, Pulse = 19) with TDAC tuning applied.

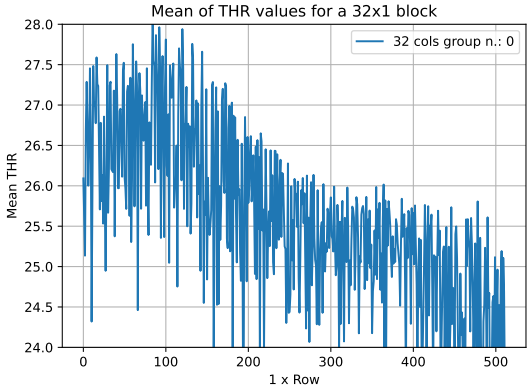

(d) Threshold (without fixed injection delay, so without BCID reset) with TDAC tuning applied.

Figure 5.31: Threshold gradient in the matrix in different phases of the tuning process with PulseStartCnfg = 30 for the DCC front-end of the non-irradiated W8R13 chip. The average over the columns is shown for every row. Note that the thresholds are expressed in DAC and not in e^-, with a conversion factor of $K_{\mathrm{DCC}} \simeq 9\ e^-/\mathrm{DAC}$.

While the difference between the maximum and minimum average threshold of the sensor's rows in Figure 5.31d can reach up to 3.5-4 DAC ($\sim 30 - 35\,e^-$) for PulseStartCnfg = 30 or 35, the difference measured for the default value of the injection delay (PulseStartCnfg = 19) is of 1-2 DAC ($\sim 10 - 20\,e^-$), which is not concerning for the operation of the sensor. The procedure, then, can be kept as it is if the PulseStartCnfg value is kept to the standard value.

5.8.5 Summary of the BCID cross-talk effects on operation with particles

The characterization of the BCID cross-talk has then given the following results:

- The effective threshold seen by the particles (with a random arrival time) is about 13-25% higher than the threshold measured with injection, with the default injection delay set to Pulse = 19.

- The random arrival time of the particle with respect to the BCID counter gives a fluctuation of the threshold that adds up to the thermal noise and threshold dispersion in determining the minimum threshold that can be set to have stable operation. This additional term from threshold fluctuation from BCID cross-talk is dominant on the other two, about $50\,e^-$ at $T_{\mathrm{NTC}} = 30$ °C, thus allowing to operate stably the sensor with a minimum threshold $> 280\,e^-$ at this temperature.
- When the TDAC tuning measured with injection is applied, the injection signal propagation delay along the column introduces an overcompensation of a threshold gradient not present when arrival time of the hit from particle is random. This effect can give a gradient in the threshold seen by particles of $\sim 20\,e^-$, with lower threshold in a part of the columns that depends on the delay set.
- The cross-talk is scaling with the matrix area where the BCID is enabled, thus in OBELIX could be 1.6 times larger if the cure for this effect is not implemented, increasing the minimum threshold achievable with stable operation to $\sim 400\,e^-$ at $T_{\mathrm{NTC}} = 30$ °C, thus degrading the detection efficiency for irradiated sensors below acceptable levels.

5.8.6 BCID cross-talk mitigation in OBELIX

This detailed study of the effects of BCID cross-talk on sensor operation with particles, together with the perspectives for OBELIX, even more dramatic, motivated further investigations into the origin of the BCID cross-talk coupling. The underlying mechanism was subsequently identified, and corrective measures were implemented before the submission of the chip, scheduled for the end of 2025.

The observed BCID cross-talk can be explained with the following mechanism. The BCID counter is distributed across the entire pixel matrix via differential lines, and perturbations in the front-end causing the threshold variation arise when the BCID driver switches bits in the pixel counters. In particular, phase shifts between the differential output lines of the driver can generate transient voltage peaks, which, together with coupling from the digital periphery to the pixel front-end through the substrate, lead to a modulation of the effective threshold.

In the OBELIX design, the mitigation strategy consisted in replacing the BCID drivers used in TJ-Monopix2 with a new version that, according to simulations, is expected to reduce the voltage peaks by approximately a factor of 30 with respect to TJ-Monopix2, while still ensuring a robust distribution of the BCID counter.

Chapter 6

TJ Monopix 2 characterization - Test Beam

During my work, I took part in a two-weeks Test Beam in March and April 2025 at the DESY Test Beam Facility, to study the behaviour of the TJ-Monopix2 sensor after irradiation. This work was conducted on the four irradiated sensors listed in Table 5.1, which have been thoroughly tested to characterize their behaviour at different temperatures. The results are presented in this chapter.

The main goal of this Test Beam was to evaluate the performance of the two cascode front-ends at different levels of radiation damage, when operated with particle beams at different temperature. The presented results have been critical for the development of both the VTX detector and the OBELIX sensor, since they identified the most radiation resistant front-end and established the operating temperature limits of the tested irradiated front-ends.

The measurements conducted on a first version of irradiated TJ-Monopix1 sensors showed a significant drop in the detector's efficiency after bulk damage, which prompted the improvement of the technology (Section 4.1.2) and the development of the TJ-Monopix2 sensor [29].

In previous test beam campaigns on TJ-Monopix2 [36], promising results were observed when measuring the performance of a sample irradiated up to 5×10^{14} 1-MeV-n_{eq}/cm^2 [37]. However, a reduction of the efficiency to $\sim 98\%$ observed at temperatures in the range of 35 °C, without a proper control of the operating conditions. The test beam campaign detailed in this chapter aimed at the full characterization of the four irradiated samples described in Table 5.1, studying the efficiency as a function of the threshold and temperature.

This was the last of several Test Beams conducted by the Belle II VTX Collaboration using TJ-Monopix2, both with irradiated and non-irradiated sensors, to fully characterize its behaviour in different conditions. Due to the high relevance for the Collaboration, a large international group of researchers took part in this work, led by the Belle II Pisa group.

6.1 Setup

While internal injection tests are particularly convenient to measure many features of a sensor, such as its threshold or noise, other relevant characteristics, such as its detection efficiency or spatial resolution, need to be tested with particle beams. Many facilities around the world offer the possibility of doing this kind of measurements, from DESY to CERN to KEK.

This Test Beam was carried out at the DESY TB21 test beam line, using 4.2 GeV electrons and the EUDET type telescope.

6.1.1 Beam

DESY Hamburg operates a test beam facility with three independent beam lines (TB21, TB22 and TB24) at the DESY II synchrotron. Electron/positron beams are available, with a user-selectable momentum in the range 1 to 6 GeV/c.

The beams are generated by a double conversion from the electrons in the DESY II beam, as shown in Figure 6.1. The first step is to insert a 7 µm thick carbon fiber in the synchrotron beam orbit, in order to produce bremsstrahlung photons in the momentum range from 1 to 6 GeV/c. These photons exit the beam from dedicated beam pipes tangential to the main beam orbit, then hit the secondary targets, made of a copper wire or aluminium

and copper plates of different thickness from 1 mm to 10 mm, and are converted via pair production into electrons and positrons.

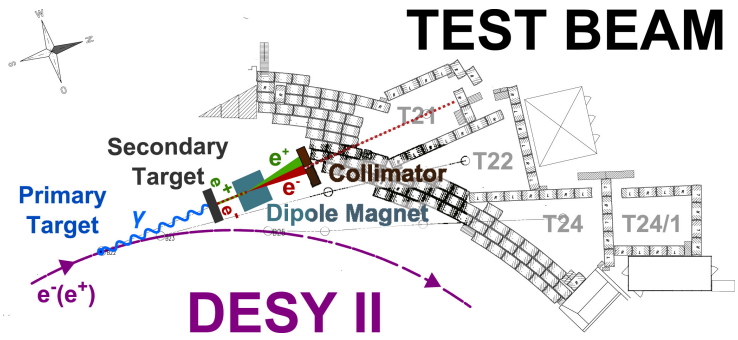

Figure 6.1: Beam generation at the DESY Test Beam facility.

A dedicated dipole magnet allows the selection of the particle charge and momentum depending on the polarity and strength of the field. The particles are then collimated and, after a (remotely) removable beam shutter, enter the test areas, where they can be additionally collimated with an exchangeable fixed-size secondary collimator, before finally hitting the telescope [38][36].

6.1.2 Telescope

Each beam area is equipped with a beam telescope, necessary to provide a reference for the tested sensor (also referred to as Device Under Test or DUT) and track the trajectories of the particles that pass through it. Each telescope is formed by multiple layers of pixel sensors with well-known space and time resolution, integration time and efficiency. In particular, they are usually divided in two arms of three planes each, in which the DUT is incorporated, with one arm upstream and one downstream. In our measurements an additional timing layer was added, which used the TelePix sensor [39].

A schematic representation and a picture of the telescope used are shown in Figure 6.2.

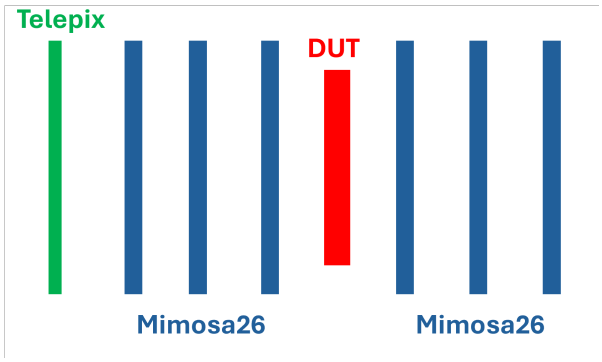

(a) Schematics

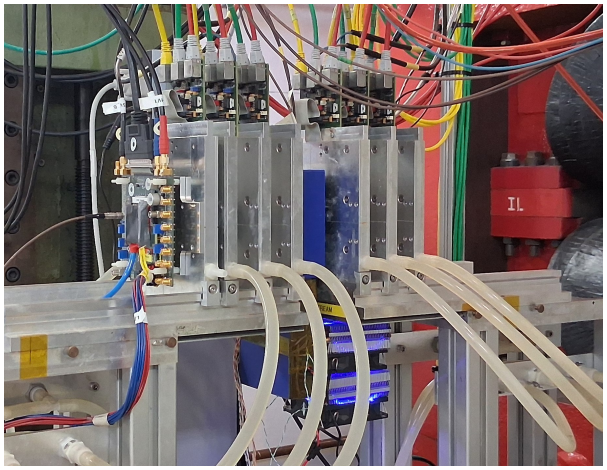

(b) Picture

Figure 6.2: Schematics and picture of the telescope and DUT setup.

At the DESY Test Beam Facility there are three telescopes available: the Adenium, the DURANTA and the DATURA.

The Adenium is an ALPIDE-based telescope prototype, which uses the ALPIDE sensor, originally developed for ALICE at the LHC. It has a better timing performance and a larger active area than the MIMOSA26-based DURANTA and DATURA telescopes.

The DATURA telescope. The DATURA telescope (like the DURANTA) [40] is an EUDET-type telescope that uses the MIMOSA26 monolithic active pixel silicon sensor. These sensors have a 1152 columns × 576 rows matrix

of square pixels, with a pitch size of 18.4 µm x 18.4 µm, which results in an active area of $\simeq$ 21.2 mm $\times$ 10.6 mm. Furthermore, their thickness of 50 µm minimizes multiple scattering within the telescope.

The sensors operate in a binary manner, since the only transmitted information is whether the signal has exceeded the threshold. The digital signals produced by the pixels are then read out in a rolling shutter mode, in which the columns are simultaneously read row by row. The entire read out process takes 115.2 µs, which is therefore the integration time per frame.

The MIMOSAs, encased in aluminium supports, are mounted on a support on which the two telescope arms can freely move on rails. Furthermore, they are cooled with a water chiller with a target temperature of 18 °C.

Acquisition mode: EUDET. The standard acquisition mode of the DATURA telescope is the EUDET mode, in which a Trigger Logic Unit (TLU) provides timestamp information on the passage of a particle through four trigger devices in coincidence. Each of these trigger devices, two in front and two behind the telescope, is a 3 mm thick and 2 cm $\times$ 1 cm scintillator matching the MIMOSA26 sensor area and attached to a photomultiplier tube [38]. The TLU and the Data Acquisition system (DAQ) of the MIMOSA26 sensors communicate in a handshake mode: when the TLU sends a trigger, the DAQ starts the readout and raises a busy signal that prevents any more triggers from arriving.

All the used sensors are integrated in the EUDAQ data acquisition framework, in which the data from them are merged and converted to event-based data.

Acquisition mode: AIDA. One of the secondary goals of this Test Beam was also to test the AIDA acquisition mode, which allows to get a better timing performance, and add the study of the Fake Hit Rate to the analysis.

This acquisition mode operates with synchronization using time stamps originating from the TLU. The communication between the sensors does not happen in handshake mode, instead the triggers are sent out continuously if there is not a veto issued by the DUT, which can veto new triggers by raising a busy signal.

The TLU trigger lasts for one clock cycle and then it is de-asserted, after which the system is ready for a new trigger.

During the operation, the TLU and the DUT do not share information about the current trigger number, which means that to keep the data aligned all the sensors need to register all the triggers. Another possible operating mode allows the TLU to ignore vetos from certain sensors, which means that TLU will issue all the possible triggers but those detectors will only record a part of them. This means that re-alignment of the data must be done after the operation, for example by comparing the time stamps of the triggers. [41]

During this Test Beam the DUT and the telescope were operated only using the timestamps of the AIDA TLU, with an offline event reconstruction that had to synchronize the clocks. The TLU clock is reset by a dedicated signal at the start of each run. During the first week of beam time the AIDA acquisition mode suffered synchronization losses (mainly in the first seconds of operation), which made the efficiency drop to zero. To limit the loss of beam time we resorted to operate with EUDET mode for the remaining of the first week.

The cause of this synchronization loss was found to be the cross-talk of an unused line of the readout board on the reset signal of the AIDA TLU, which caused unexpected resets of the clock counter. The AIDA mode has then been used during the second week of beam time.

Telepix. The DATURA telescope can process a maximum trigger rate of 3 kHz, while the available particle rates can go up to several 10 kHz. This can clearly cause ambiguities with multiple hits in single data frames. To improve the timing capabilities of the telescope, an additional pixel sensor, called TelePix, has been integrated into it, with a target timing resolution < 5 ns. Made in a 180 nm HV-CMOS technology, it has a matrix of 29 $\times$ 124 pixels, with a pitch of 165 $\times$ 25 µm^2. Signals are amplified inside the active pixel and digitized in the periphery at one edge of the sensor. The active depletion layer can be increased with a bias of up to 80 V.

Both the time-of-arrival (ToA, 10 bit) and time-over-threshold, (ToT, 10 bit) are registered in the periphery. The ToA is sampled on both clock edges, thus doubling the timestamp precision. Dedicated measurements have found that the achieved timing resolution is of 3.16 ns [39].

6.1.3 Temperature control

The cooling setup used in the laboratory in Pisa could not be used in the Test Beam, mainly because most of the parts were in front or behind the sensor, increasing multiple scattering, and also could not be placed vertically.

For these reasons it was necessary to build a new cooling setup. One of the main requirements was the possibility of doing measurements at a fixed temperature, independently of environmental conditions and changes in the sensor

temperature due to a varied power consumption. Additionally, a wider temperature range than the one obtained with the Pisa's setup would have been beneficial to the testing campaign.

With these requirements in mind, two new cooling setups were specifically designed and built at HEPHY: one was mounted in the telescope (Figure 6.3b) and one was used in the laboratory to test the other sensors in parallel to the beam operation. As can be seen in Figure 6.3a, the temperature of the sensor was controlled by putting it in contact with an end of a copper plate, which was connected to the other end to a Peltier cell that set the temperature. Two fans on top of the Peltier cell were mounted to contribute to the cooling process.

To monitor and control the humidity of the air and avoid condensation, a hygrometer and a N_2 flux were used, while also closing the sensor in a box with the copper plate.

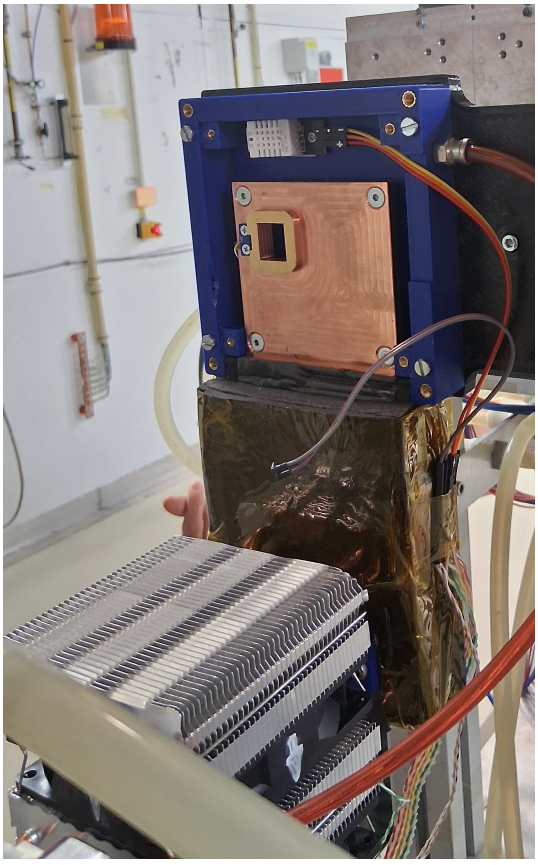

(a) The setup with the copper plate visible

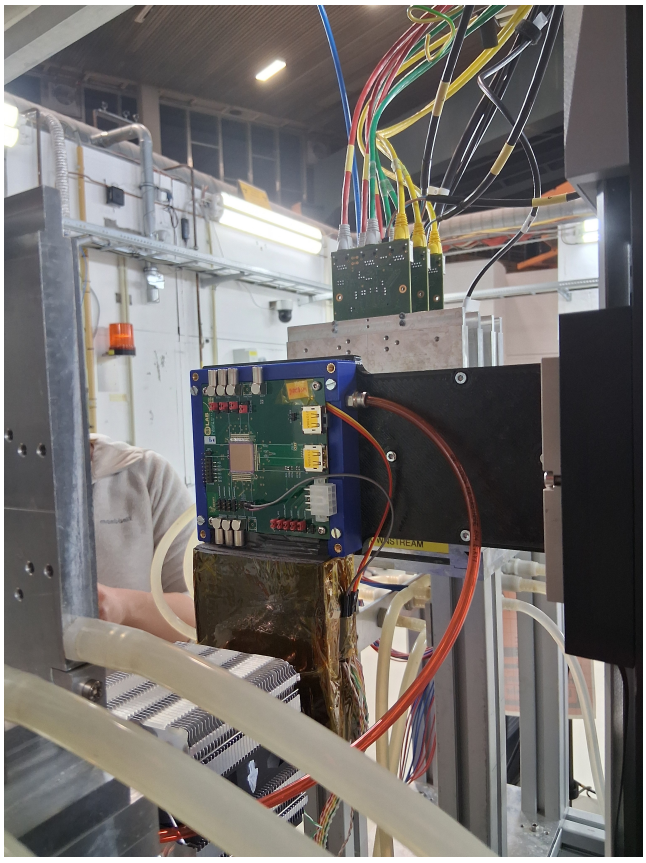

(b) The setup with the W8R6 chip mounted in the telescope

Figure 6.3: Pictures of the setup mounted in the telescope.

To find the relation between the temperature T_{Cu} of the copper plate and the temperature of the NTC placed on the PCB of the sensor, these temperatures were collected for all the runs done with all the sensors. Predictably, the NTC temperature showed a linear dependence on the copper one and a linear fit was conducted to find the values of the parameters. As also shown in Figure 6.4, from the fit:

$$T_{\mathrm{NTC}} = (0.744 \pm 0.001) \cdot T_{\mathrm{Cu}} + (6.76 \pm 0.05)\,^{\circ}\mathrm{C} \tag{6.1}$$

with a $\chi^2/ndof = 0.25$.

A web interface controlled the setup, which allowed to set the temperature on the copper together with a lookup table to associate it to the desired sensor temperature. Once the temperature was set, the system authomatically powered the Peltier and the fan in order to gradually bring the copper to the desired temperature (usually ~ 10 minutes were required to change the temperature). This setup allowed to test the sensors at temperatures between 10 and 50 °C, but its operating range was actually significantly larger.

Additionally, a separated web interface controlled the powering and the biasing of the sensor, while also monitoring its currents.

All the data from these two monitoring systems have been recorded and collected in dedicated log files.

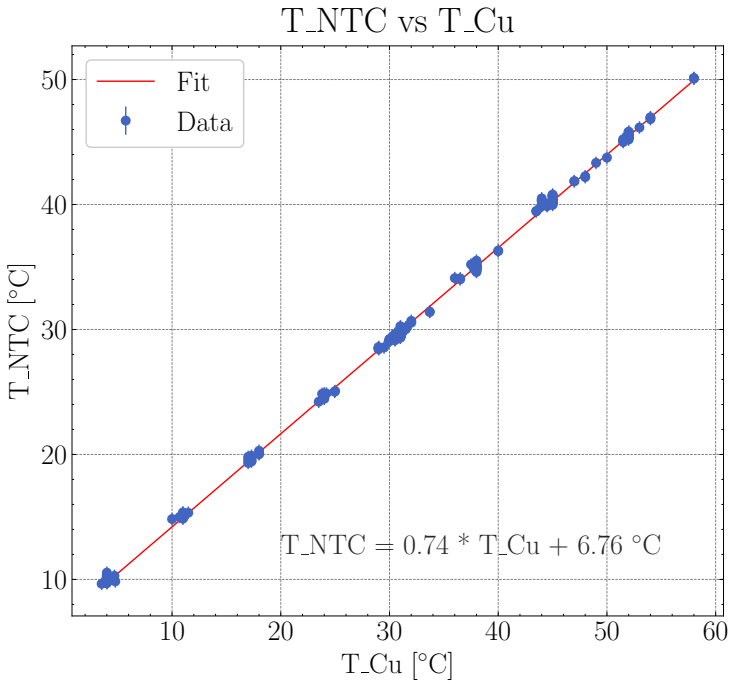

Figure 6.4: Calibration of the NTC temperature with respect to the temperature of the copper.

However, the copper plate revealed to be a significant issue for the operation with beams, since the border of the hole specifically done to let the particles pass through the setup overlapped with the top 80 rows of the matrix. This caused the tracking algorithm to fail at reconstructing many tracks that passed through those rows, since it did not take into account the multiple scattering in the plate. This can be seen from Figure 6.5: in Figure 6.5a the hitmap of the MIMOSA on a plane in the downstream arm shows an increased number of hits along the contour of this opening, while in Figure 6.5b the distribution of the hits on the DUT of the reconstructed tracks shows a dramatic drop in the number of tracks along the same contour. For this reason, a region with low efficiency could be found in the top rows of the matrix, therefore the last 80 rows of every sensor were masked to avoid effects on the result of the global efficiency.

6.2 Analysis

During this Test Beam 270 good data runs (i.e. not for debugging or without DAQ errors during the acquisition) were conducted.

The analysis of the data was initially conducted on a limited sample (some tens of seconds of beam data) right after the acquisition, in order to get a preliminary result that could suggest to repeat some tests or to push the sensor towards more extreme operating conditions.

After the end of the Test Beam, then, the entire data set has been analyzed using the full statistics.

6.2.1 Analysis framework

The analysis uses the Corryvreckan reconstruction and analysis framework [42], which has been designed and developed specifically to be used at Test Beams to easily reconstruct the data.

This framework uses a modular design to improve the flexibility of the analysis algorithms. These modules can work with data from all the detectors in the setup or only from some of them, with many different purposes. Some of them, for example, are used to correctly load the events from a detector, while others merge these data to implement the reconstruction of the tracks or the alignment of the setup.

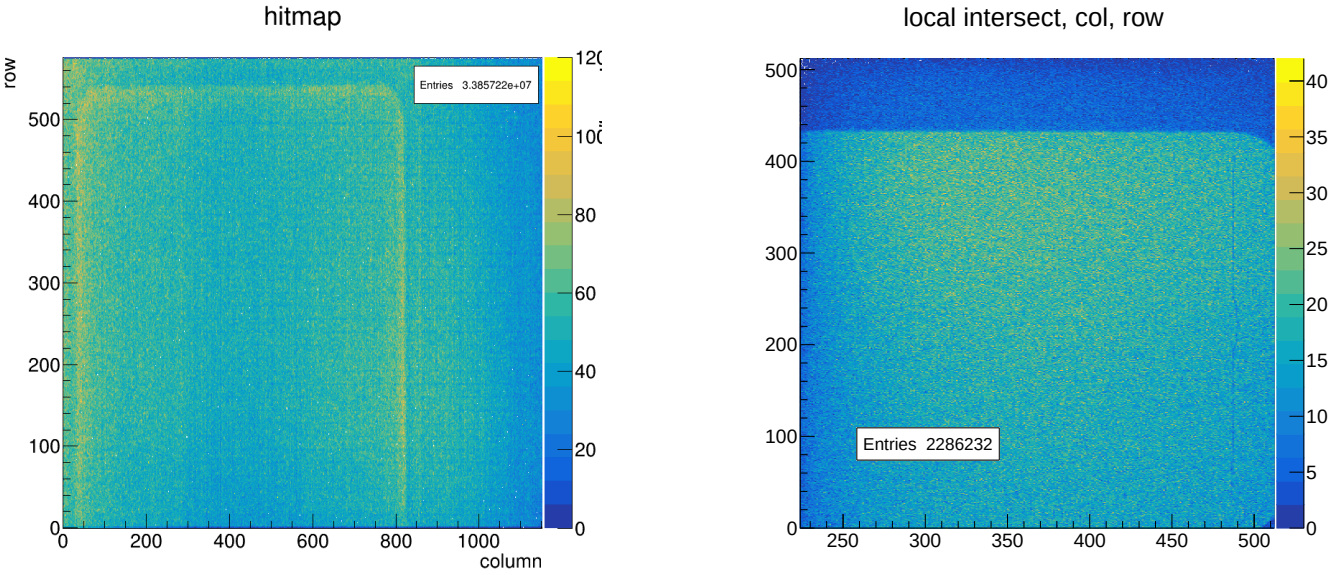

(a) MIMOSA26

(b) W8R6

Figure 6.5: Hitmap of a MIMOSA26 behind the copper plate (a) and track interception on the W8R6 sensor (b), the one irradiated with maximum fluence. In both the contour of the opening in the copper plate is clearly visible.

6.2.2 Tracking

Once the data are correctly divided into events, the track reconstruction process can begin which is the most important step in the analysis of the data. This process requires multiple steps.

The first one is the masking of the pixels next to disabled pixels in the DUT. This is done in order to avoid reconstructing tracks passing through the border of the active area, where many factors (i.e. charge sharing with disabled pixels or mechanical vibrations) could negatively impact the track fitting.

Subsequently, another important step is clustering, because particles traversing through a sensor can release energy in more than just one pixel. If the collected charge is sufficiently high, multiple adjacent pixels can fire simultaneously. For this reason, hits in adjacent pixels are clustered together and are associated to a single traversing particle.

Lastly, the reconstruction of the tracks of the electrons is done using the [*Tracking4D*] module of Corryvreckan. This method can either use a simple line fit ignoring scattering or a General-Broken-Lines fit [43]. The one implemented in this analysis is the latter, which takes multiple scattering into account by dividing the trajectory in multiple segments, each between two adjacent planes.

After a first fit with a straight line is done to get aproximated values for the tracks parameters, the measured points y_i and their standard deviation σ_i for each plane are fitted with the least squares method in order to minimize the function:

$$S(\mathbf{u}) = \sum_{i=1}^{n} \frac{(y_i - u_i)^2}{\sigma_i^2} + \sum_{i=2}^{n-1} \frac{\beta_i^2}{\sigma_{\beta,i}^2} \tag{6.2}$$

where $\mathbf{u}$ is the vector of all the track interceptions u_i with the planes, while β_i are the kink angles due to the multiple scattering, which have expectation values zero and variances $\sigma_{\beta,i}^2$ given by the multiple scattering theory [44]. These variables are also described in Figure 6.6.

The fitted tracks are then temporarily stored to be used in subsequent steps of the alignment or analysis process.

6.2.3 Alignment procedure

Another crucial part of the analysis process is the alignment procedure, in which the relative positions of the sensors are found using the reconstructed tracks. It is a very delicate operation, since a small misalignment can significantly affect the reconstruction power of the tracking method and the measurement of the efficiency.

The first step of this process is the measurement by hand of the relative position of the planes of the telescope, which is then used as a starting value for the prealignment and alignment processes carried out by Corryvreckan.

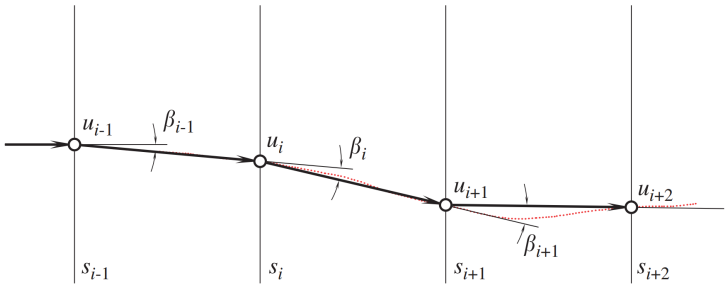

Figure 6.6: Particle trajectory with fitted interceptions and u_i and kink angles β_i.

The prealignment, which uses the [*Prealignment*] module, iteratively finds the relative positions between the planes by translationally shifting the planes, using the correlation histograms to adjust these values.

After tracking, which requires the prealignment in order to be successful, the fine alignment can be done. The alignment is conducted in two steps: firstly the telescope is aligned with multiple (5-10) iterations of the [*AlignmentMillepede*] or the [*AlignmentTrackChi2*] modules, then the DUT is aligned with the [*AlignmentDUTResidual*] module. The results are then written for each sensor in a *geometry* file, from which further alignment iterations or the analysis take the information about the relative positions of the planes. After the alignment process is finished, during the analysis, the tracking is done again using the last geometry file from the alignment procedure.

Each of the cited algorithms uses the reconstructed tracks in the tracking phase to precisely find the relative positions and rotations of the planes. To do it, the planes are moved and the tracks refitted a user-selected number of times.

The [*AlignmentMillepede*] uses an adaptation to analyze test beam data of the Millepede method [45], which allows to quickly converge thanks to an optimized algorithm to deal with systems with multiple global and local parameters. This method, however, needs a good prealignment to properly converge.

The [*AlignmentTrackChi2*], instead, uses the least squares method to validate the various steps of the iteration.

The [*AlignmentDUTResidual*], finally, moves the DUT to minimize the residuals of the track intercepts with its plane with respect to the hits that it recorded.

6.2.4 Sanity checks

During alignment and analysis, it is crucial to have clear indicators of whether the procedure has successfully converged. This aspect was particularly relevant during the online analysis performed in parallel with data acquisition, as it allowed us to distinguish between unexpected results (e.g. very low efficiency) caused by a run that needed to be repeated and those arising from poor alignment.

One of the first checks consists in examining the correlation histograms between the various sensors and the MIMOSA telescope plane chosen as reference. Due to their importance as a preliminary validation tool of the alignment, the histograms of the correlations of all the sensors were monitored during the run using the [*OnlineMonitor*] module of Corryvreckan. The signature of a proper alignment is the presence of a straight diagonal line crossing the origin, as shown in Figure 6.7.

Another relevant aspect of the alignment is given by the track multiplicity (i.e. the number of tracks per event), which can also be monitored while the analysis is going on from the output on the terminal, and in normal condition was in the range $\simeq 3-7$. A number of tracks minor of these values can mean that the alignment needs to be redone.

An important check to do is the stability of the efficiency over time: as said in Section 6.1.2, for example, the AIDA mode suffered a loss of efficiency after some time, which clearly placed this check at the top of the to-do list when running the analysis during the Test Beam. This drop usually happened after few tens of seconds but, as can be seen in Figure 6.8, it can happen also after ~ 20 minutes.

Finally, the goodness of the alignment can be verified by checking the mean values of the hit residuals, the distance between the intercept of the track extrapolated on the sensor and the corresponding hit, in the x and y directions, which should be compatible with zero. Since the tracking algorithm of the DUT only associates hits to a track if they are inside a 100 µm $\times$ 100 µm region around the track interception with the detector, a bad alignment (i.e. such that part of the residuals distribution is clipped by this cut) can significantly reduce the measured efficiency.

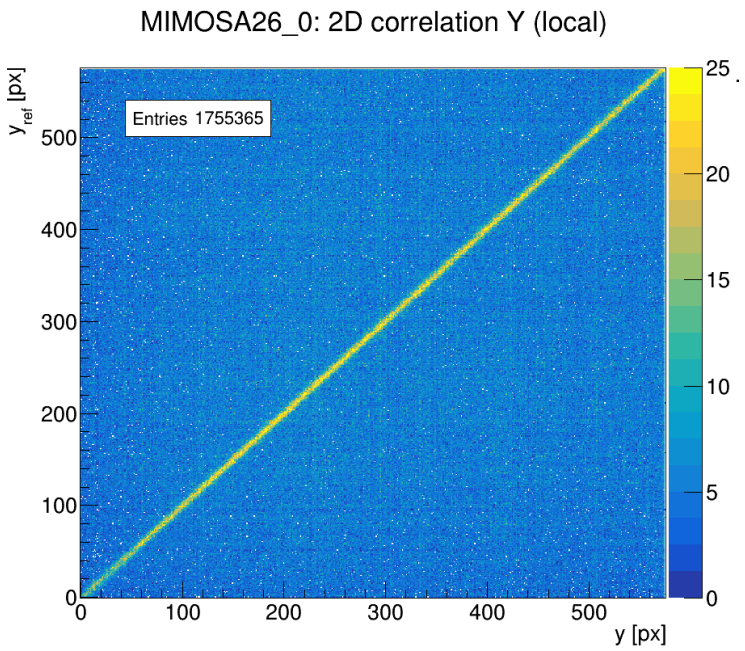

Figure 6.7: Correlation histogram on the y coordinate of the first MIMOSA with the third (set as a reference).

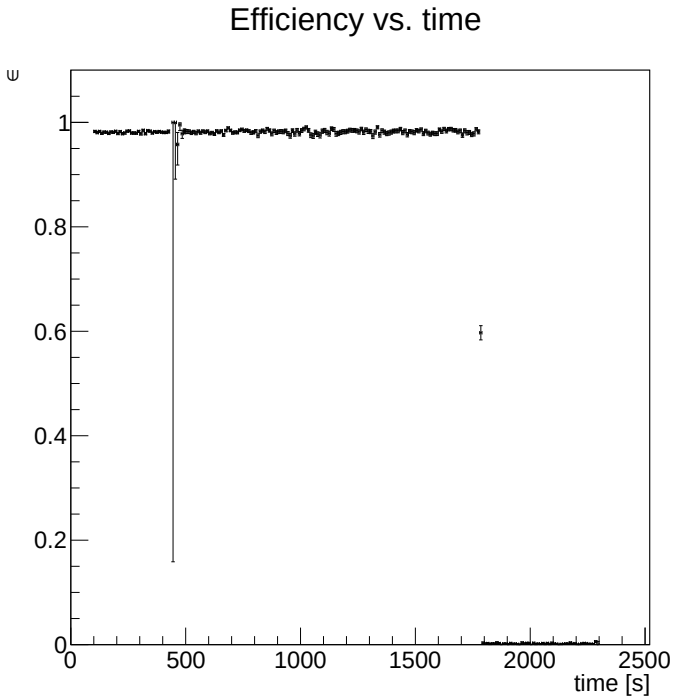

Figure 6.8: Efficiency evolution in time for a run of the W2R5 sensor. The drop in efficiency towards the end of the run is clearly visible.

6.3 Results

Results from previous test campaigns [36, 37] had already confirmed that the specifications in terms of resolution and efficiency could be achieved with non-irradiated TJ-Monopix2 sensors. The main objective of the present campaign was to study the dependence of the efficiency of irradiated sensors on operating temperature and threshold, with particular emphasis on comparing the two cascode front-ends, DCC and HVC.

The long process of the analysis of the complete data set is undergoing many iterations. In this chapter the results from the first completed iteration are presented.

In the analysis two modules are used: [*AnalysisEfficiency*], to carry the efficiency-related measurements, and the [*AnalysisDUT*], which gives general information about the sensor, such as the hitmap of the clusters associated to a track (an example in Figure 6.9) or its residuals.

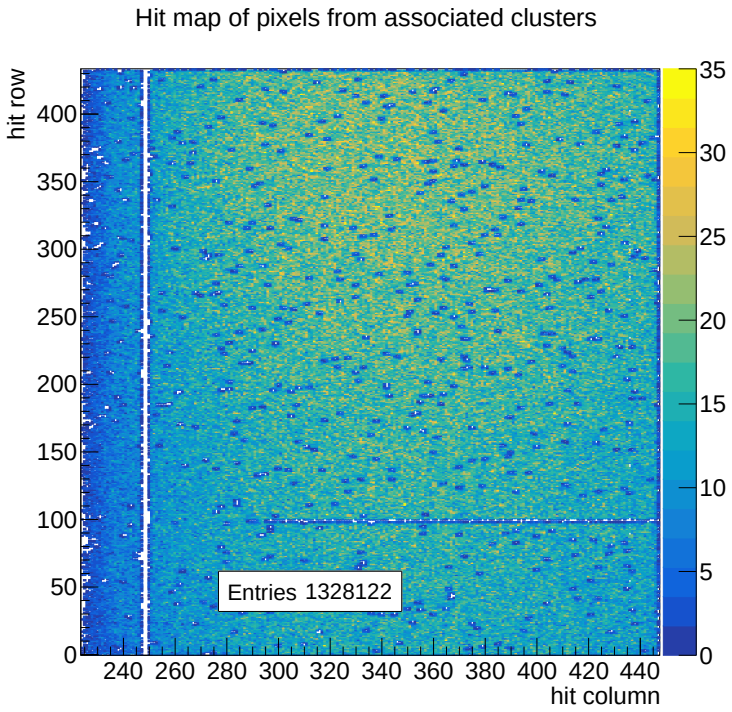

Figure 6.9: Hitmap on the DCC front-end of the W8R6 sensor (irradiated with maximum fluence).

6.3.1 Efficiency

The efficiency of the sensor is measured using the tracking algorithm described in Section 6.2.2 to reconstruct the tracks of the beam's particles. Each track is extrapolated to the DUT and a cluster is associated to the track if it is found within a given distance from the track (usually ±100 µm). The efficiency is computed as the ratio of the number of tracks with an associated DUT cluster $N_{\text{ass cls DUT}}$ over the total number of them that passes through it $N_{\text{tracks DUT}}$:

$$\varepsilon = \frac{N_{\text{ass cls DUT}}}{N_{\text{tracks DUT}}} \tag{6.3}$$

The statistical error is computed using the formula:

$$\sigma_{stat} = \sqrt{\frac{\varepsilon(1-\varepsilon)}{N_{\text{tracks DUT}}}} \tag{6.4}$$

Typical efficiency values of non irradiated sensors are $> 99.95\%$.

Dependence of the efficiency on bias. To study the internal behaviour of the pixel, the local position of a track interception within it is recorded for all the tracks and the local efficiency is computed.

After bulk irradiation, the change in the doping concentration and trapping effects might require higher reverse bias voltage to reach the full depletion of the epitaxial p layer and to increase the lateral electric field in the pixel corners (see Section 3.6), improving collection efficiency.

During the Test Beam, all the chips have been tested varying the bias voltage from the minimum values used for non-irradiated sensors (DCC: 6 V, HVC: 10 V) to the maximum allowed for each chip, as listed in Table 5.3, to study the dependence of the efficiency on the bias.

The results from the W8R6 chip (proton irradiated with the highest fluence) are shown in Figure 6.10a for the DCC front-end and in Figure 6.10b for the HVC front-end.

The measurements have been conducted on a limited range of tensions, without exploring tensions lower than 6 V for the DCC and 10 V for the HVC. From these results it can be seen that the bias voltage needed to saturate the efficiency is different for the two front-ends: for the DCC it is 12-14 V, while for the HVC it is ≥ 40 V, since the saturation is not achieved at this bias. Nevertheless with HV = 40 V the efficiency reached was already acceptable ($> 99.5\%$) and, since increasing further the HV applied to the sensor could break the device, it was decided to keep this as HV limit.

Furthermore, the reduction of the detection efficiency in the corners can be seen in both the front-ends, together with the improvements at higher bias tension. These are shown in Figures 6.11 and 6.12 for the DCC and HVC front-ends. For both the front-ends the bias voltage considered are the minimum reached and an intermediate value at which the efficiency has not saturated yet. For the HVC front-end the smaller statistics (due to a smaller front-end) causes a coarser granularity in the color scale than the DCC.

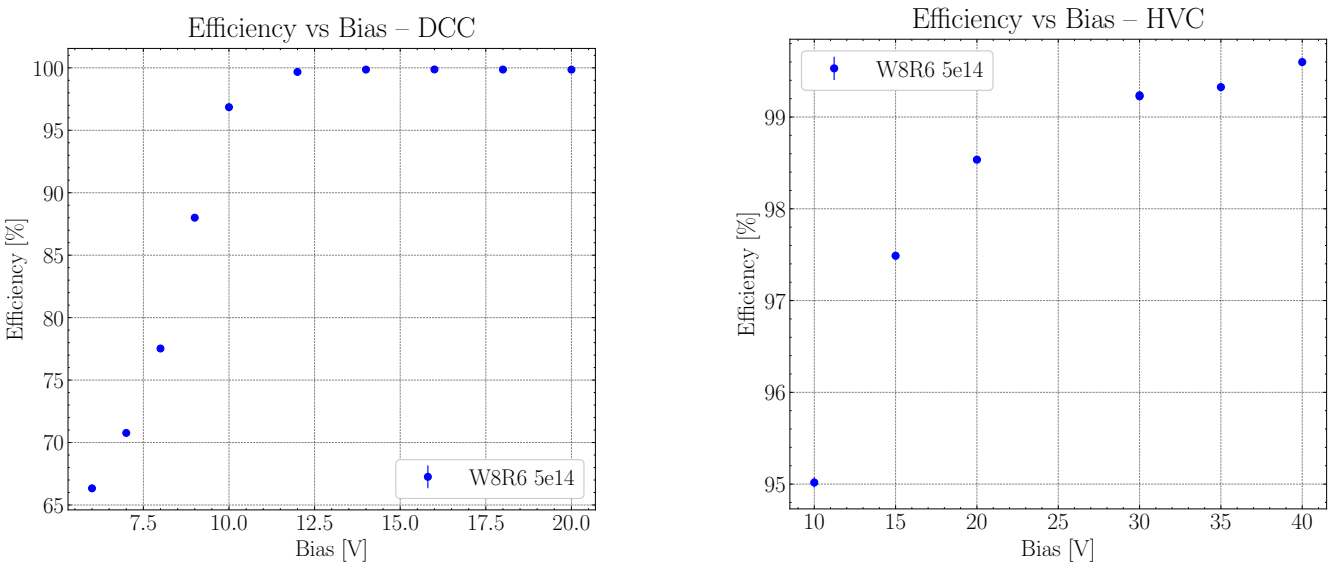

(a) DCC (b) HVC

Figure 6.10: Dependence of the efficiency on the bias of the DCC (a) and (b) front-end of the W8R6 sensor, the one irradiated with 5×10^{14} 1-MeV-n_{eq}/cm^2 fluence.

Dependence of efficiency on threshold. The dependence of the detection efficiency on the threshold of the sensor is one of the main features under study in this analysis.

As already discussed in Section 5.8.2, the effective threshold seen by particles is not the result of the measurements with a fixed injection phase after the reset of the BCID counter, but it is about 13-25 % higher due to the BCID cross-talk effect as shown in Equation 5.13. However, the thresholds quoted in these results are the ones measured with a fixed injection delay that corresponds to the minimum of the threshold variation.

In Figure 6.13, the efficiency as a function of the threshold is shown for the DCC and HVC front-ends of the various tested sensors. The data shown are from measurements conducted on the sensors biased with the maximum tension possible (listed in Table 5.3).

Note that there are many different sets of parameters that are implemented, which leads to a greater variance in the behaviour of the sensor. These values have been collected searching for the highest value of the threshold for which the sensor had managed to operate above the target efficiency.

As a side note, the W2R17 sensor could only be operated at thresholds higher than $\simeq 330\, e^-$, because at a lower value the noise produced enough hits to block the readout.

From the results shown in Figure 6.13 three main conclusions can be drawn:

- The efficiency of the DCC version is significantly higher than that of the HVC, particularly at higher fluences, where the DCC maintains superior efficiency across the entire range of tested thresholds.

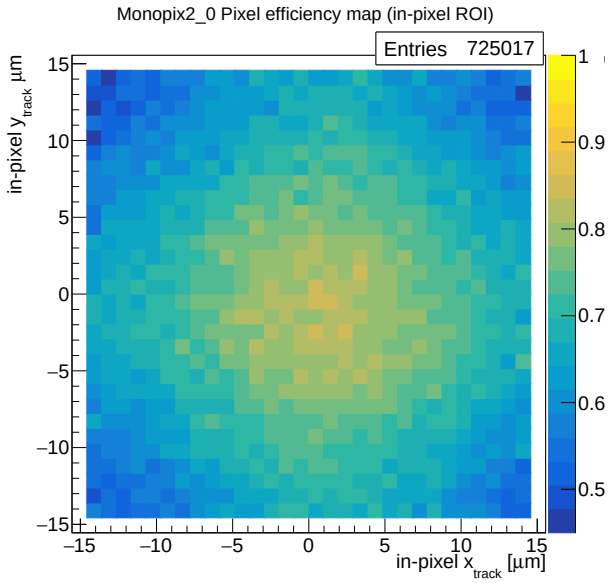

(a) Bias = 6 V, total efficiency = 66.3 %

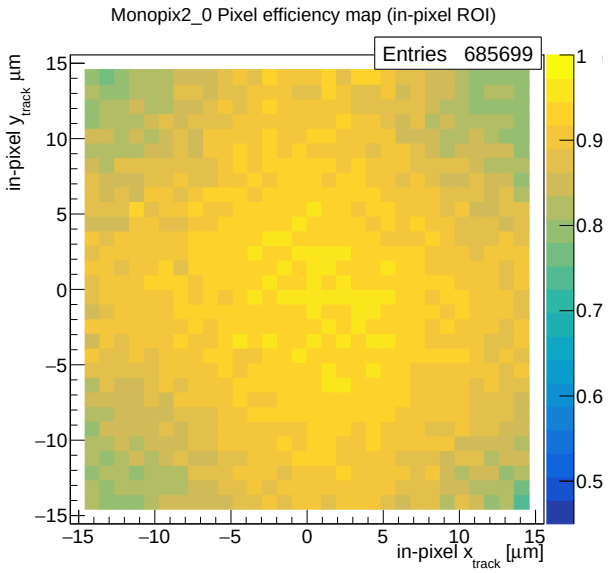

(b) Bias = 9 V, total efficiency = 88.0 %

Figure 6.11: In-pixel efficiency map of the DCC front-end of the W8R6 chip for bias = 6 V (a) and for bias = 9 V (b). The improvement in the efficiency in the corners is clearly visible.

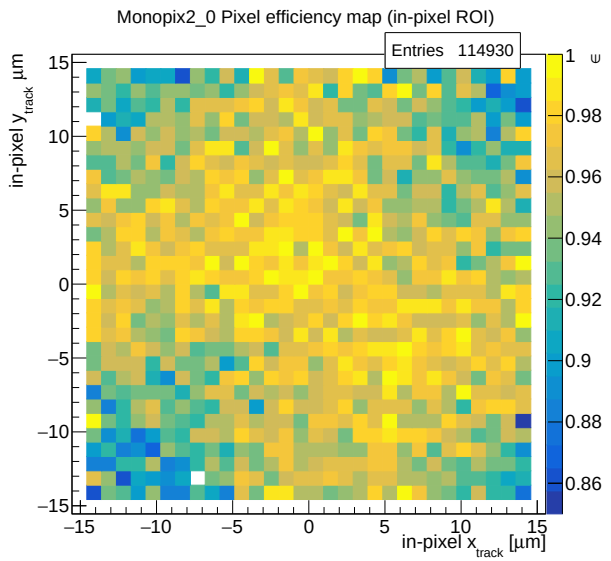

(a) Bias = 10 V, total efficiency = 95.0 %

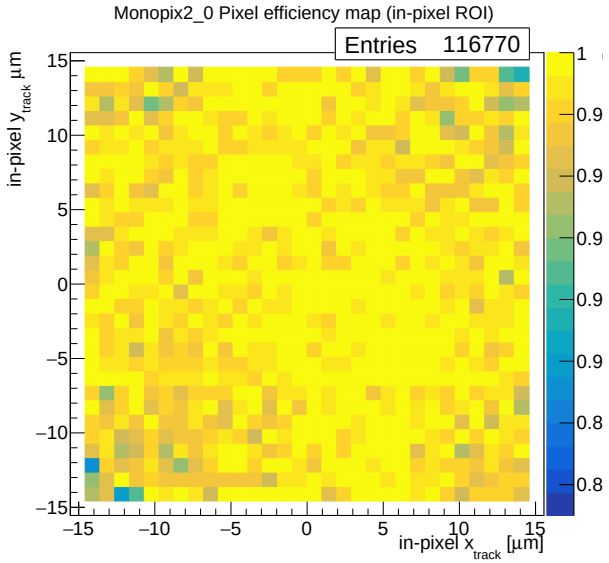

(b) Bias = 20 V, total efficiency = 98.5 %

Figure 6.12: In-pixel efficiency map of the HVC front-end of the W8R6 chip for bias = 10 V (a) and for bias = 20 V (b). The improvement in the efficiency in the corners is clearly visible.

- The efficiency is correlated with the level of bulk damage: sensors irradiated with lower equivalent fluence preserve higher efficiency than those exposed to higher fluence at the same threshold.
- Furthermore the W2R5 sensor (electron irradiated) exhibited higher efficiency than the W8R6 (proton irradiated at the same equivalent fluence 5×10^{14} 1-MeV-n_{eq}/cm^2), suggesting that the electron irradiation induces less bulk damage than proton irradiation at the same 1 MeV equivalent fluence, contrary to the expectations from the NIEL model.

  As also shown in Section 5.7.2, the leakage current measurement is consistent with this observation, indicating that the electron irradiated sensor may experience reduced bulk damage under the same neutron equivalent

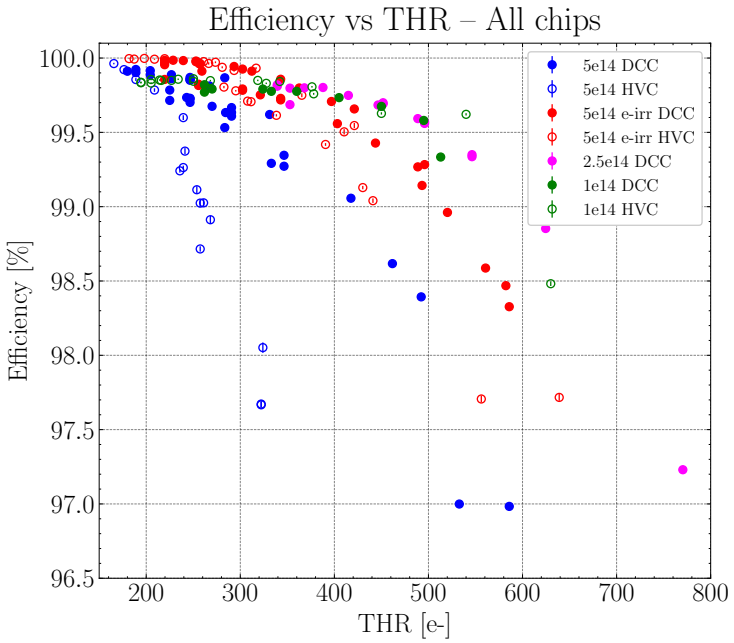

Figure 6.13: Efficiency dependence on threshold for the cascode front-ends.

fluence.

Table 6.1 summarizes the approximate threshold values at which each sensor and front-end reaches the target efficiency of 99%.

Chip	Fluence [1-MeV-n_{eq}/cm^2]	THR DCC [e^-]	THR HVC [e^-]
W8R4	1	> 600	> 600
W2R17	2.5	600	-
W2R5	5 e.irr	510	450
W8R6	5	430	260

Table 6.1: Values of the threshold at which the different front-ends reach the target efficiency of 99 %.

Dependence of efficiency on temperature Another important feature of the irradiated sensors is the dependence of their efficiency on the operating temperature. As already explained, the rise in leakage current with temperature increases both the threshold and the noise of the sensor, thereby raising the minimum stable operating threshold and reducing the efficiency.

The study aimed to determine the maximum operating temperature at which the sensor maintains a target efficiency of 99%. A key challenge of this Test Beam was to identify the optimized operating point that preserves efficiency above this threshold at elevated temperatures, while minimizing the fraction of masked pixels, with a reference limit of 1%.

In Figure 6.14 the efficiency dependence on the temperature is shown for all the tested sensors and front-ends. For each temperature, different operating points were explored, resulting in varying efficiencies at the same temperature. The data presented come from measurements with standard settings.

Operating temperature limit and comparison between DCC and HVC front-ends. The measurements presented in this chapter allow the determination of the operating temperature limits for the VTX sensor, which are crucial for the final design of the module cooling strategy, and enable the assessment of the best-performing front-end between the DCC and HVC versions.

To be conservative, the conclusions are drawn based on data from the W8R6 proton-irradiated sensor at the target fluence of 5×10^{14} 1-MeV-n_{eq}/cm^2 (shown in Figures 6.15 and 6.16), as it exhibited a higher level of damage

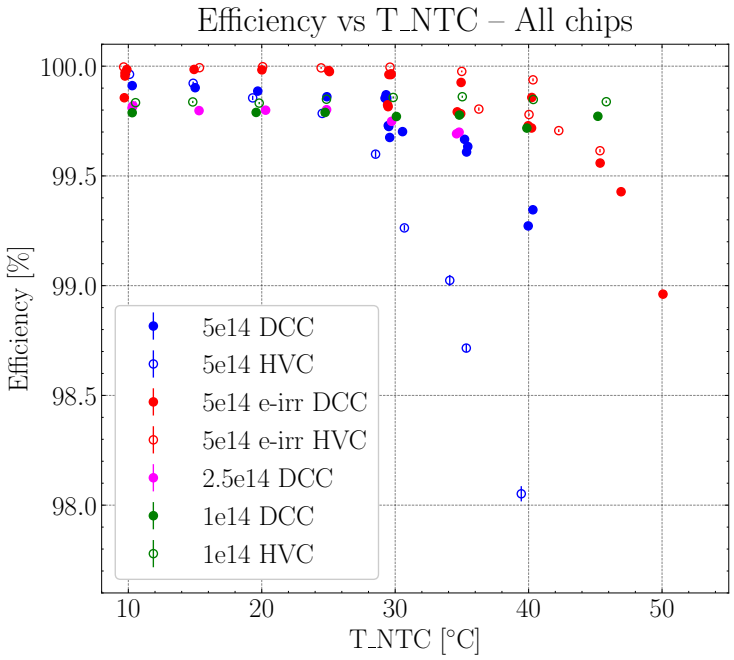

Figure 6.14: Efficiency dependence on temperature of the NTC for the cascode front-ends.

compared to the electron irradiated sensor, and significant uncertainties remain regarding the background levels expected after the SuperKEKB interaction region redesign.

The comparison in Figure 6.15 shows that the DCC front-end has a better radiation resistance than the HVC one, since it manages to keep its efficiency $> 99\%$ up to a threshold of $\simeq 430\,e^-$, while the HVC front-end only up to $\simeq 260\,e^-$.

The same response is given by the dependence of the sensor's behaviour on the temperature in Figure 6.16, which shows that the DCC front-end can operate with an efficiency of $\geq 99\%$ up to $\simeq 40$ °C, while the HVC only up to $\simeq 35$ °C. After 40 °C, however, the operation of the W8R6 sensor becomes particularly challenging due to increased leakage current and noise. Note that the quoted T_{NTC} temperature is ~ 7 °C lower than the actual temperature of the sensor, which is the one used in the simulations of the VTX cooling apparatus.

From these measurements, therefore, a target operating temperature of 30 °C has been decided for the VTX detector, which allows for some safety margin for the integration of OBELIX. Furthermore, the clear indication that the DCC front-end manages to keep a high efficiency up to higher thresholds and temperatures than the HVC one contributes to the OBELIX development, in particular to the decision of the type of front-end that will be implemented in the sensor.

Efficiency drop in the corners. An example of a phenomenon studied using the in-pixel efficiency (i.e. the local position of a track intercepiton within a pixel) is given by the efficiency drop in the corners of the pixel.

This effect was already shown by the tests on TJ-Monopix1 and its root cause was later found to be the insufficient charge collection capabilities in the sides of the pixels due to a low lateral field. For this reason the modification of the process described in 4.1.2 was implemented already in the TJ-Monopix1 and then in the TJ-Monopix2 sensors.

The histogram of the efficiency inside the pixel is used to check for this drop in efficiency in order to understand the behaviour of this modification in the TJ-Monopix2 sensor after irradiation. While at low threshold the efficiency stays high in all the parts of the pixels, it drops once the threshold is increased and the signals induced by smaller collected charge do not exceed the threshold of the discriminator. The significant drop at the corners found in all the sensors shows that this charge collection problem is still present, even though the drop is smaller than its predecessor at $\sim$ the same conditions.

The magnitude of this drop is also different (at the same operating threshold and temperature) for the DCC and the HVC front-end, as can be seen in Figure 6.17, where the efficiency maps for a threshold of $\simeq 500\,e^-$ are shown for both the front-ends. The mean efficiency of the sensor is 86.9% for the HVC and 97.0% for the DCC and the lower value of the former is due to the efficiency loss in the corners of the pixels, where the efficiency is $\sim 75\%$, while it stays over 95% in the DCC front-end.

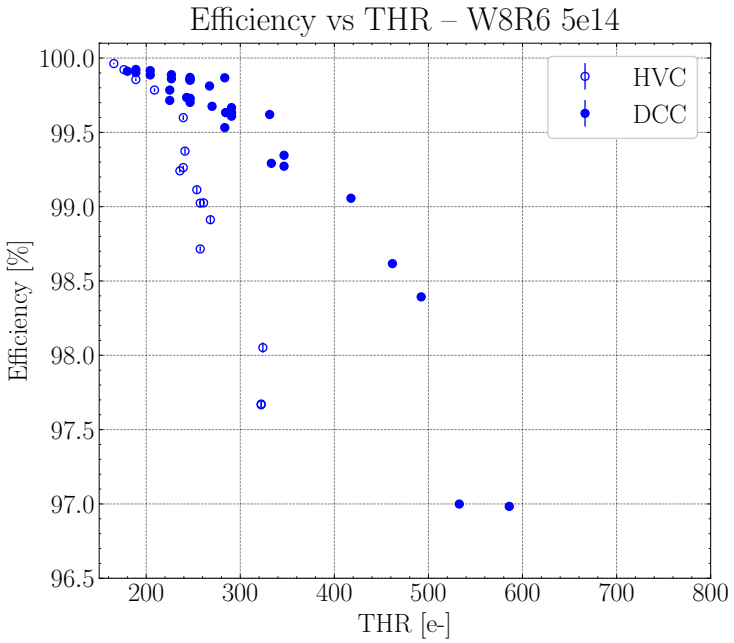

Figure 6.15: Comparison between the DCC and HVC front-ends of the efficiency dependence on threshold.

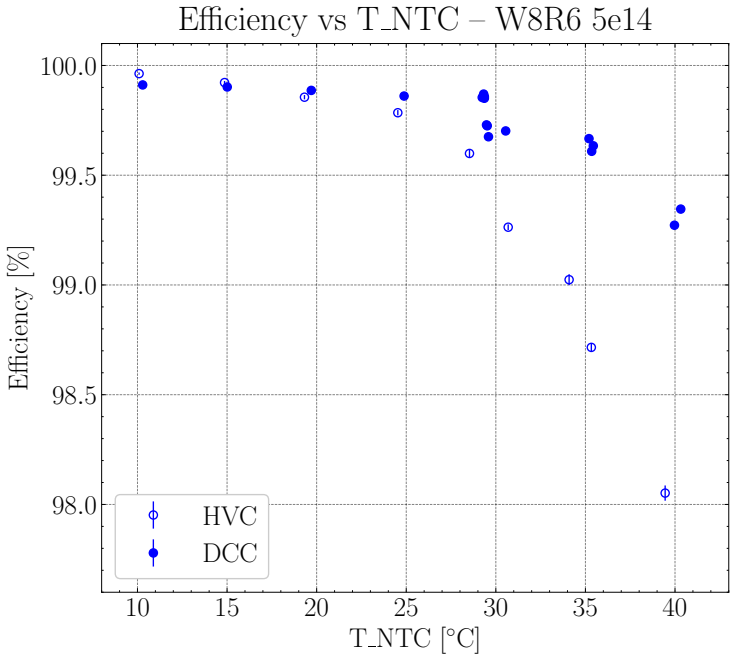

Figure 6.16: Comparison between the DCC and HVC front-ends of the efficiency dependence on temperature.

6.3.2 Position resolution

The final measurements presented concern the sensor position resolution, which can be determined from the standard deviation of the residuals distribution between reconstructed tracks and the associated hits on the DUT, after subracting in quadrature the contribution from the uncertainty in the track extrapolation onto the DUT. In Figure 6.18a it is shown for the DCC front-end of the W8R6 sensor, the one irradiated with maximum fluence.

If a DUT only produces single hits, without clusters, the maximum resolution is given by the standard deviation of the uniform distribution: $\sigma_{\mathrm{DUT,\,unif}} = p/\sqrt{12}$, where p is the pitch of the pixels. This is because if only one pixel fires, the position of the track interception can only be estimated with a uniform distribution. However, if clusters of more than one pixel are produced, Position Finding Algorithms (PFAs) can be employed to find more precisely

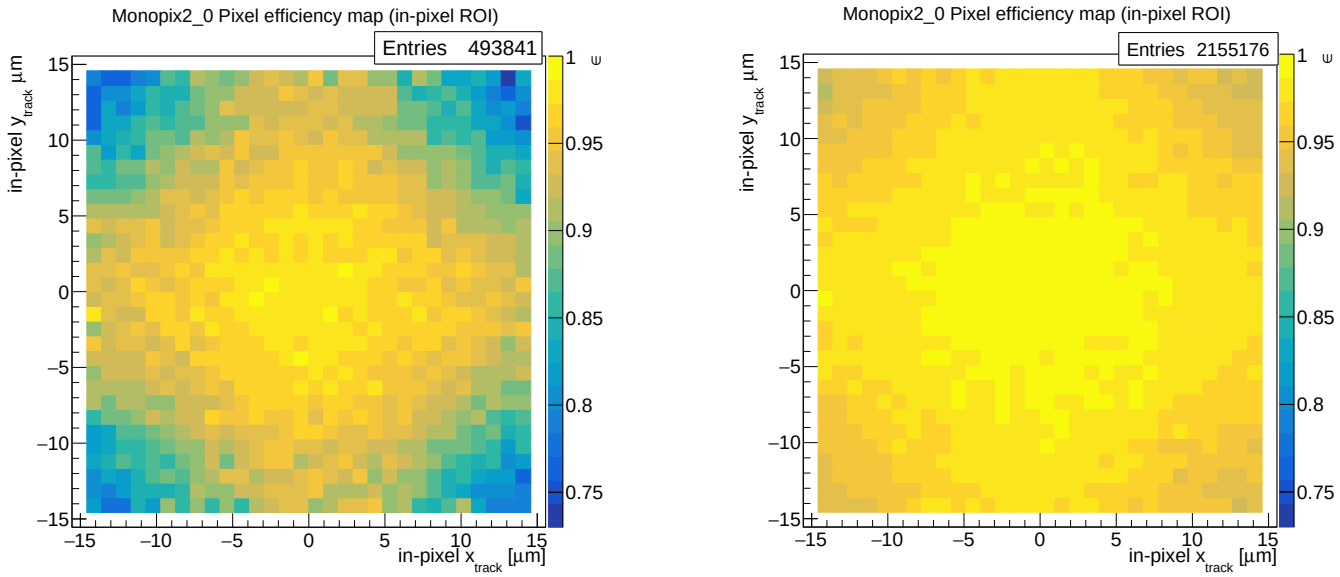

(a) HVC, total efficiency = 86.9 %

(b) DCC, total efficiency = 97.0 %

Figure 6.17: In-pixel efficiency map for thresholds of $\simeq 500\,e^-$ for the HVC front-end (a) and for the DCC front-end (b) of the W8R6 sensor, the one irradiated with 5×10^{14} 1-MeV-n_{eq}/cm^2 fluence. The clear difference in the efficiency in the corners of the pixel is visible, with the HVC front-end with the lower one.

the effective position of the hit on the sensor, exploiting the analog information on the collected charge.

For example, before irradiation the position resolution can reach < 8 µm, thanks to the higher charge sharing and cluster size. The average cluster size for the tested irradiated sensors, instead, is in the range $1.25 - 1.44$, which only allows to obtain a position resolution similar to the one obtainable with only digital information. An example is given in Figure 6.18.

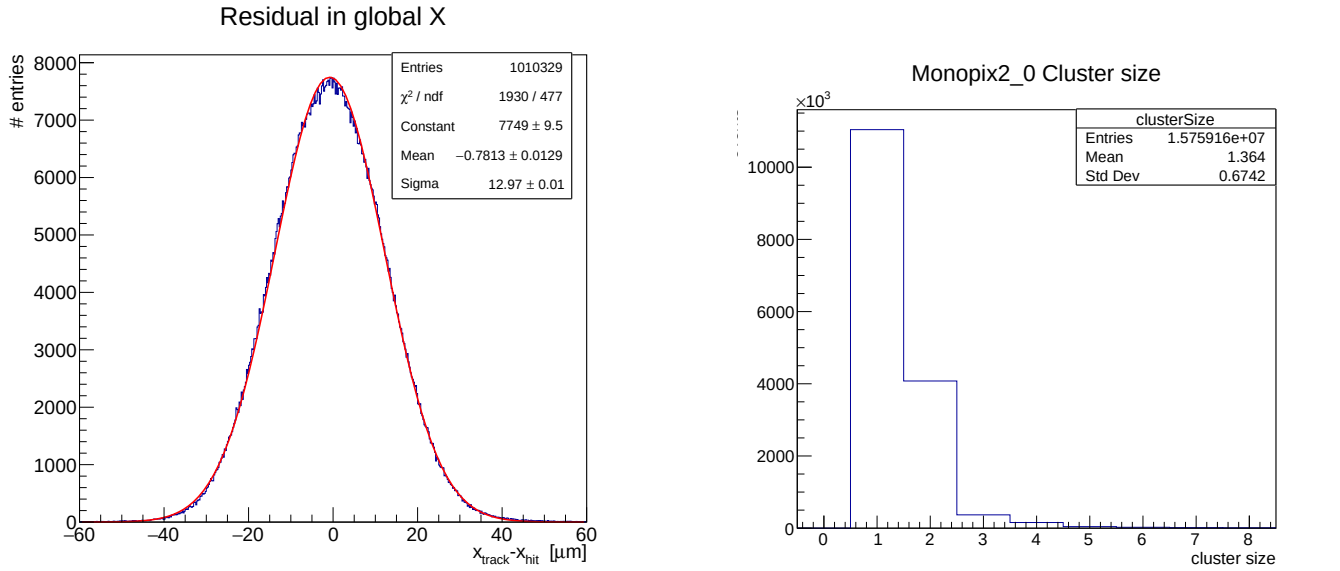

(a) Residuals on the x axis.

(b) Cluster size distribution.

Figure 6.18: Residuals on the x axis and cluster size for a run on the DCC front-end of the W8R6 sensor, the one irradiated with 5×10^{14} 1-MeV-n_{eq}/cm^2 fluence. The chip was run at 20 °C with a threshold of $204\,e^-$, obtaining a detection efficiency of 99.88%.

The resolution of the sensor is given by the equation:

$$\sigma_{\mathrm{DUT}} = \sqrt{\mathrm{Var}(s_{\mathrm{fit}} - s_{\mathrm{hit}}) - \sigma_{\mathrm{tel}}^2} \tag{6.5}$$

where s_{fit} and s_{hit} are the coordinates of the intersection of the telescope track on the DUT plane and of the hit on the DUT, while σ_{tel} is the uncertainty of the telescope track on the DUT, determined by the telescope resolution and the setup geometry.

Using the results in [46] for the same EUDET telescope and similar geometry used in this Test Beam for the contribution from the track extrapolation σ_{tel} of the telescope ($\sigma_{\mathrm{tel},\,x} \simeq \sigma_{\mathrm{tel},\,y} \simeq 4.4$ µm), the resolution of the sensors can be computed for both the x and y coordinates and compared with the standard deviation of the uniform distribution $\sigma_{\mathrm{DUT,\,unif}} = p/\sqrt{12} = 9.5$ µm. The results are slightly different from chip to chip and from front-end to front-end, but are in general between 9.5 and 11 µm, where the higher values are likely related to some additional contribution from not optimal alignment.

As a final note, the position resolution extracted from the residuals shows a dependence on the alignment quality, as can be seen in Figure 6.19, where the resolutions for the HVC front-end of the W8R6 and W2R5 sensors (proton and electron irradiated at maximum fluence, respectively) are divided for alignment groups (a block of consecutive runs that share the same alignment). This effect is an indication that in some groups the alignment quality was not optimal, increasing the estimated position resolution extracted from a wider residual distribution. Therefore, in the next iteration of the analysis, greater attention must be given to the alignment of these runs to reduce the systematic effects affecting them.

Furthermore, at higher thresholds, the resolution saturates, approaching the value determined solely by the digital information ($p/\sqrt{12}$). In contrast, at lower thresholds, the cluster size increases, enabling the application of dedicated algorithms to achieve improved position resolution.

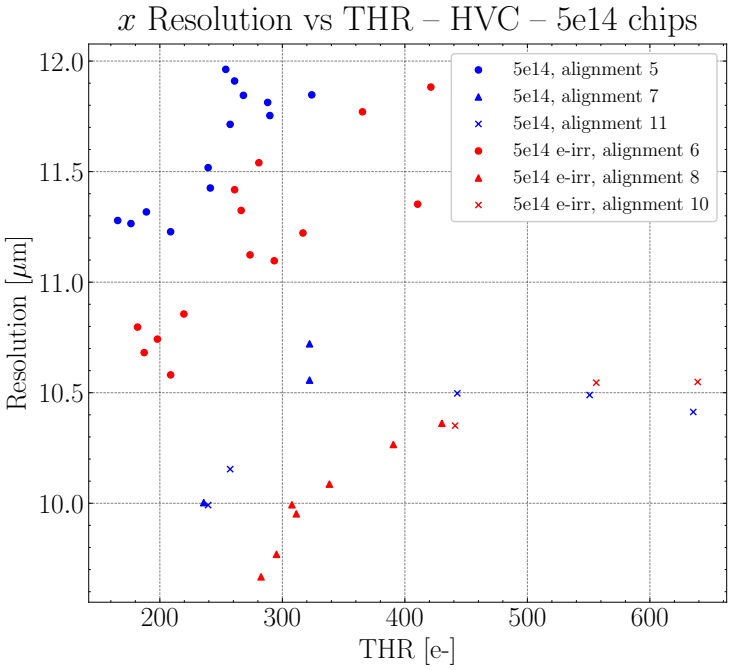

Figure 6.19: Dependence of the resolution on the threshold and the alignment group for the HVC front-end of the W8R6 and W2R5 sensors, respectively proton and electron irradiated at maximum fluence.

Chapter 7

Conclusions

This thesis presents the results of the characterization of the TJ-Monopix2 chip, a small collection electrode DMAPS in a modification of the TowerJazz Semiconductor 180 nm CMOS process, after irradiation.

The measurements described have been conducted in laboratory and with particle beams on the cascode front-ends of four devices, irradiated with fluences from 1×10^{14} 1-MeV-n_{eq}/cm^2 to 5×10^{14} 1-MeV-n_{eq}/cm^2, covering the full range of the radiation damage expected during the 10-year operation of the VTX detector.

The evolution of the sensor performance at different temperatures has been of significant relevance, due to the planned operation of VTX at room temperature. The tests have been conducted in the temperature range between 10 and 50 °C.

The variation of the sensor threshold as a function of temperature has been thoroughly studied, identifying the discharge of the collection electrode due to the leakage current as one of the main causes of this effect.

The fake hit rate of the sensor has also been measured as a function of temperature, showing that both the DCC and HVC front-ends are able to mantain it below 10^{-2} Hz/pixel, orders of magnitude lower than the expected rates in the inner and outer layers of VTX.

A cross-talk effect originating from the clock signal has been characterized, which limits the stable and efficient operation of the sensor at low threshold. This effect is expected to become more pronounced in OBELIX, prompting the implementation of mitigation strategies in its upcoming submission. In particular, the impact of this cross-talk on sensor performance during operation with particles has been investigated.

The efficiency of these sensors has been studied at a Test Beam at DESY. Two important results have been achieved: the identification of the DCC as the most radiation-hard front-end, based on the comparison of the detection efficiency degradation with increasing threshold of the DCC and HVC front-ends; and the determination of the operating temperature of the VTX detector, based on the observed detection efficiency degradation with increasing temperature and the safety margins for the integration of OBELIX. The former result, in particular, has led to the decision to adopt the DCC front-end as the definitive choice for OBELIX, already from the first submission.

This work is part of the broader effort toward the upgrade of the Belle II vertex detector, essential to achieve the ambitious physics goals of the Collaboration. This effort will continue with the submission of the OBELIX sensor, scheduled for the end of this year, followed by its testing, characterization and integration in a system project for the construction of the VTX detector. The installation of this detector is planned to begin in 2032, with physics operations expected to resume in 2034.

This work is also part of a global effort in the research and development of CMOS MAPS detectors, which are opening new frontiers of low-material tracking and are at the center of many future projects, such as FCC-ee.

Bibliography

[1] E Kou et al. "The Belle II Physics Book". In: *Progress of Theoretical and Experimental Physics* 2019.12 (2019), p. 123C01. DOI: 10.1093/ptep/ptz106.

[2] P. Raimondi, D. N. Shatilov, and M. Zobov. *Beam-Beam Issues for Colliding Schemes with Large Piwinski Angle and Crabbed Waist*. 2007.

[3] S. Navas et al. "Review of Particle Physics". In: *Phys. Rev. D* 110 (3 2024), p. 030001. DOI: 10.1103/PhysRevD.110.030001.

[4] H. Aihara et al. *The Belle II Detector Upgrades Framework Conceptual Design Report*. 2024.

[5] Ludovico Massaccesi. "Search for CP violation in the $D^0 \to \pi^+\pi^-\pi^0$ decay at the Belle II experiment". PhD thesis. University of Pisa, 2025.

[6] The Belle II Collaboration. *The Belle II Experiment at SuperKEKB – Input to the European Particle Physics Strategy*. 2025.

[7] T. Abe et al. *Belle II Technical Design Report*. 2010.

[8] Leila Jones et al. "The APV25 deep submicron readout chip for CMS detectors". In: (1999). DOI: 10.5170/CERN-1999-009.162.

[9] Lingxin Meng. *ATLAS ITk Pixel Detector Overview*. 2021.

[10] Sudhir Malik and on behalf of the CMS Tracker Group. "CMS Phase-2 Inner Tracker Upgrade". In: *Journal of Physics: Conference Series* 2374.1 (2022), p. 012053. DOI: 10.1088/1742-6596/2374/1/012053.

[11] *Technical Design Report for the ATLAS Inner Tracker Strip Detector*. Tech. rep. Geneva: CERN, 2017.

[12] Fabio Ravera. *The CMS Outer Tracker for the High Luminosity LHC*. Tech. rep. Geneva: CERN, 2024. DOI: 10.7566/JPSCP.42.011010.

[13] Maximilian Babeluk. "Development and Testing of Depleted Monolithic Active Pixel Sensors in 180 nm CMOS technology for the Belle II VTX Upgrade". reposiTUm. PhD thesis. Vienna University of Technology, 2025. DOI: https://doi.org/10.34726/hss.2025.107368.

[14] S. Bettarini et al. "The DMAPS upgrade of the Belle II vertex detector". In: *Journal of Instrumentation* 19.02 (2024), p. C02060. DOI: 10.1088/1748-0221/19/02/C02060.

[15] B Abelev et al and (The ALICE Collaboration). "Technical Design Report for the Upgrade of the ALICE Inner Tracking System". In: *Journal of Physics G: Nuclear and Particle Physics* 41.8 (2014), p. 087002. DOI: 10.1088/0954-3899/41/8/087002.

[16] H. Kolanoski and N. Wermes. *Particle Detectors: Fundamentals and Applications*. 1st ed. Oxford University Press, 2020.

[17] *Technical Design Report for the ATLAS Inner Tracker Pixel Detector*. Tech. rep. Geneva: CERN, 2017. DOI: 10.17181/CERN.FOZZ.ZP3Q.

[18] *The Phase-2 Upgrade of the CMS Tracker*. Tech. rep. Geneva: CERN, 2017. DOI: 10.17181/CERN.QZ28.FLHW.

[19] J. Baudot et al. "First test results Of MIMOSA-26, a fast CMOS sensor with integrated zero suppression and digitized output". In: *2009 IEEE Nuclear Science Symposium Conference Record (NSS/MIC)*. 2009, pp. 1169–1173. DOI: 10.1109/NSSMIC.2009.5402399.

[20] Michael Moll. "Radiation damage in silicon particle detectors: Microscopic defects and macroscopic properties". Ph.D. Thesis (Advisor: G. Lindstrom); Dissertation, Universität Hamburg, 1999. Dissertation. Universität Hamburg, 1999, p. 251. DOI: 10.3204/PUBDB-2016-02525.

[21] L. Massaccesi. "Performance study of the SVD detector of Belle II and future upgrades". Available at https://docs.belle2.org/pub_data/documents/4033/. Master's thesis. Pisa, IT: University of Pisa, 2021.

[22] Christopher J. Kenney et al. "A prototype monolithic pixel detector". In: *Nuclear Instruments and Methods in Physics Research Section A: Accelerators, Spectrometers, Detectors and Associated Equipment* 342.1 (1994), pp. 59–77. DOI: https://doi.org/10.1016/0168-9002(94)91411-7.

[23] Giacomo Contin. "The MAPS-based vertex detector for the STAR experiment: Lessons learned and performance". In: *Nuclear Instruments and Methods in Physics Research Section A: Accelerators, Spectrometers, Detectors and Associated Equipment* 831 (2016). Proceedings of the 10th International "Hiroshima" Symposium on the Development and Application of Semiconductor Tracking Detectors, pp. 7–11. DOI: https://doi.org/10.1016/j.nima.2016.04.109.

[24] Wikipedia contributors. *Tower Semiconductor — Wikipedia, The Free Encyclopedia*. [Online; accessed 27-September-2025]. 2025.

[25] M. Mager. "ALPIDE, the Monolithic Active Pixel Sensor for the ALICE ITS upgrade". In: *Nuclear Instruments and Methods in Physics Research Section A: Accelerators, Spectrometers, Detectors and Associated Equipment* 824 (2016). Frontier Detectors for Frontier Physics: Proceedings of the 13th Pisa Meeting on Advanced Detectors, pp. 434–438. DOI: https://doi.org/10.1016/j.nima.2015.09.057.

[26] T Noulis et al. "Noise Analysis of Radiation Detector Charge Sensitive Amplifier Architectures". In: (2008). DOI: 10.5170/CERN-2008-008.486.

[27] I. Caicedo et al. "The Monopix chips: depleted monolithic active pixel sensors with a column-drain read-out architecture for the ATLAS Inner Tracker upgrade". In: *Journal of Instrumentation* 14.06 (2019), C06006–C06006. DOI: 10.1088/1748-0221/14/06/c06006.

[28] R. Cardella et al. "MALTA: an asynchronous readout CMOS monolithic pixel detector for the ATLAS High-Luminosity upgrade". In: *Journal of Instrumentation* 14.06 (2019), p. C06019. DOI: 10.1088/1748-0221/14/06/C06019.

[29] Konstantinos Moustakas. "Design and Development of Depleted Monolithic Active Pixel Sensors with Small Collection Electrode for High-Radiation Applications". Available at https://repository.cern/records/6tesn-kkg39. PhD thesis. Bonn, DE: University of Bonn, 2021.

[30] Magdalena Munker et al. "Simulations of CMOS pixel sensors with a small collection electrode, improved for a faster charge collection and increased radiation tolerance". In: *JINST* 14.05 (2019). Proceedings of the PIXEL 2018 Workshop, p. C05013. DOI: 10.1088/1748-0221/14/05/C05013.

[31] W. van Hoorn. "Study and Development of a novel Silicon Pixel Detector for the Upgrade of the ALICE Inner Tracking System". Available at https://repository.cern/records/s4e9y-sne35. PhD thesis. Vienna, AT: TU University of Vienna, 2015.

[32] H. Pernegger et al. "Radiation hard monolithic CMOS sensors with small electrodes for High Luminosity LHC". In: *Nuclear Instruments and Methods in Physics Research Section A: Accelerators, Spectrometers, Detectors and Associated Equipment* 986 (2021), p. 164381. DOI: https://doi.org/10.1016/j.nima.2020.164381.

[33] C. Bespin. "Characterization of the TJ-Monopix2 Depleted Monolithic Active Pixel Sensor for High-Energy Physics Experiments". Available at https://inspirehep.net/literature/2853779. PhD thesis. Bonn, DE: University of Bonn, 2024.

[34] M. S. Calò. "Study of monolithic CMOS pixel sensors in the Belle II experiment upgrade". Available at https://docs.belle2.org/pub_data/documents/3881/. Master's thesis. Pisa, IT: University of Pisa, 2024.

[35] Lars Schall et al. *Cross talk of a large-scale depleted monolithic active pixel sensor (DMAPS) in 180 nm CMOS technology*. 2024.

[36] M. Schwickardi. "Characterisation of CMOS Sensors for the Belle II Vertex Detector Upgrade". PhD thesis. Goettingen, DE: University of Goettingen, 2024. DOI: 10.53846/goediss-10611.

[37] A. Kumar et al. "Upgrade of the Belle II Vertex Detector with monolithic active pixel sensors". In: *Proc. of the 42nd International Conference on High Energy Physics (ICHEP 2024)*. Vol. 476. Pre-published Jan. 16, 2025; published Apr. 29, 2025. PoS (SISSA), 2025, p. 0909. DOI: 10.22323/1.476.0909.

[38] R. Diener et al. "The DESY II test beam facility". In: *Nuclear Instruments and Methods in Physics Research Section A: Accelerators, Spectrometers, Detectors and Associated Equipment* 922 (2019), pp. 265–286. DOI: https://doi.org/10.1016/j.nima.2018.11.133.

[39] H. Augustin et al. "Upgrading the beam telescopes at the DESY II Test Beam Facility". In: *Nuclear Instruments and Methods in Physics Research Section A: Accelerators, Spectrometers, Detectors and Associated Equipment* 1040 (2022), p. 167183. DOI: 10.1016/j.nima.2022.167183.

[40] H. Jansen. "Resolution studies with the DATURA beam telescope". In: *Journal of Instrumentation* 11.12 (2016), p. C12031. DOI: 10.1088/1748-0221/11/12/C12031.

[41] P. Baesso, D. Cussans, and J. Goldstein. "The AIDA-2020 TLU: a flexible trigger logic unit for test beam facilities". In: *Journal of Instrumentation* 14.09 (2019), P09019–P09019. DOI: 10.1088/1748-0221/14/09/p09019.

[42] D. Dannheim et al. "Corryvreckan: a modular 4D track reconstruction and analysis software for test beam data". In: *Journal of Instrumentation* 16.03 (2021), P03008. DOI: 10.1088/1748-0221/16/03/p03008.

[43] Claus Kleinwort. "General broken lines as advanced track fitting method". In: *Nuclear Instruments and Methods in Physics Research Section A: Accelerators, Spectrometers, Detectors and Associated Equipment* 673 (2012), 107–110. DOI: 10.1016/j.nima.2012.01.024.

[44] V. Blobel. "A new fast track-fit algorithm based on broken lines". In: *Nuclear Instruments and Methods in Physics Research Section A: Accelerators, Spectrometers, Detectors and Associated Equipment* 566.1 (2006). TIME 2005, pp. 14–17. DOI: https://doi.org/10.1016/j.nima.2006.05.156.

[45] V. Blobel and C. Kleinwort. "A New method for the high precision alignment of track detectors". In: *Conference on Advanced Statistical Techniques in Particle Physics*. 2002.

[46] M. Antonello et al. "Precision determination of the track-position resolution of beam telescopes". In: *Nuclear Instruments and Methods in Physics Research Section A: Accelerators, Spectrometers, Detectors and Associated Equipment* 1072 (2025), p. 170185. DOI: 10.1016/j.nima.2024.170185.